Nondestructive Interaction of Ultrafast Laser Pulses with Transparent Dielectrics

by

Sebastian W. Winkler

(Under the direction of William M. Dennis)

Abstract

The interaction of focused ultrashort pulses with a thin transparent dielectric sample under the destruction threshold is investigated by studying the change in the pulse shape as a function of input pulse energy. The complex field is measured using an improved high dynamic range second harmonic generation frequency resolved optical gated experiment and analyzed using improved phase retrieval algorithms. The experimental results are compared to computer simulations, which show that the pulse develops strong spatio-temporal dependences due to the generation of an under-critical free carrier plasma.

Index words: Ultrafast, Nondestructive Interaction, Pulse Splitting, Fused Silica, m-FROG, Frequency Resolved Optical Gating

Nondestructive Interaction of Ultrafast Laser Pulses with Transparent Dielectrics

by

Sebastian W. Winkler

Dipl. Phys. Technische Universität Berlin 2003

A Dissertation Submitted to the Graduate Faculty
of The University of Georgia in Partial Fulfillment
of the
Requirements for the Degree

Doctor of Philosophy

Athens, Georgia

2009

Nondestructive Interaction of Ultrafast Laser Pulses with Transparent Dielectrics

by

Sebastian W. Winkler

Approved:

Major Professor: William M. Dennis

Committee: Steven Lewis
Susanne Ullrich
Sean Kirkpatrick

Electronic Version Approved:

Maureen Grasso
Dean of the Graduate School
The University of Georgia
May 2009

Acknowledgments

First I want to thank my family: My parents, my sister. Your love and support made it possible to go to school, study in the US, do research and finally write this dissertation. I want to thank you; this is is for you.

I want to take this chance to thank Erik Zeek for teaching me about FROG and the magic involved. My thanks goes to Tom, Mohua, and Sarah for discussing physics with me, correcting my english, making my talks better, working in the office and laboratory with me and being my friends over the past four years. Susanne, Arkadi, Nick, Billy, and Cyril I want to thank for both allowing me and helping me to work in their laboratories. A special thanks to Carl: Thank you for welcoming me in Athens (and in Saint E. for that matter), opening doors, having my back and allowing me to learn from you. I also want to express my gratitude for the friendship and collaboration I have had over the years with Jeremy, who discussed physics and politics with me and allowed me a deeper insight into both. Thanks to Dr. Lewis and Dr. Kirkpatrick for spending their valuable time serving on my committee. I want the thank Razvan for inviting me to Saint Ètienne, discussing hot topics of all areas with me, and teaching me about light. Dr. Dennis: In your way, you made me a better physicist and person. I want to thank you for your patience, your advice, your trust, and the opportunity to work with you. I think I am now a better physicist and person. Oh yes, I need to thank you for the nurturing and mentoring that I was so happy to enjoy over the years. May many more students profit from the same treatment!

Most of all I want to thank Kamilya. Ich liebe Dich. Danke dass Du da bist, dass Du Geduld mit mir hast. Ohne Dich bin ich nicht ganz.

Table of Contents

Page

Acknowledgments iv

List of Tables vii

Chapter

1 Introduction 1

2 Ultrafast Laser Pulse - Transparent Dielectric Interaction . . 6

2.1 Nonlinear Optics 8

2.2 Drude-Lorenz Model 11

2.3 Electron Generation 15

2.4 Pulse Propagation Simulations 20

3 Considerations: Measuring and analyzing the shape of ultrashort pulses 24

3.1 Using Frequency Resolved Optical Gating to measure ultrafast pulses 25

3.2 Experimental Setup 34

3.3 FROG analysis Software 52

3.4 FROG Simulation 63

4 Experimental Results and Comparison with Computer Simulation 69

4.1 Experimental Results 69

4.2 Comparison of the Experimental Results to Computer Simulations 83

4.3 Conclusions 97

5 Summary, Conclusion and Future Work 100

Appendix

A Computing the gradient of Z with respect to E 103

Bibliography 106

List of Tables

2.1 The terms used to simulate the propagation of the ultrashort pulse. 22

2.2 The parameters used in the computer simulation [138]. 23

3.1 G_{error} depending on offsets with and without the OC. 60

4.1 G_{error} and offset compensation (OC) for the retrieved complex fields in Fig 4.2. 71

4.2 G_{error} and offset compensation (OC) for the retrieval process of the complex fields in Fig 4.6. 79

4.3 G_{error} and offset compensation (OC) for the retrieved complex fields in Fig 4.7. 79

4.4 G_{error} and offset compensation (OC) for the retrieved complex fields in Fig. 4.17. Note that the G_{error} scales with $\sqrt{n_f n_\tau}$. 98

Chapter 1

Introduction

With the increased interest in laser-induced modification of transparent materials for industrial applications, a detailed and fundamental understanding of the interaction between the laser pulse and the material has become essential. In the last 20 years laser pulses with pulse width shorter than 0.5 ps (ultrafast) have become widely available. Ultrafast laser pulses are now used to modify dielectrics and organic materials on micro- and nanometer length scales, to write waveguides in bulk materials and to polish the surfaces of a variety of different materials [1–35]. The current interest is driven by the advantages provided by ultrafast pulses when used for precise material modifications. Since the pulse width is short compared to the lattice relaxation time, which is on the order of picoseconds, the energy deposition and the introduced modifications are well localized in the volume irradiated. Furthermore, ultrafast pulses can be used to modify materials that only absorb at high intensities, allowing (due to multiphoton absorption) modifications of transparent materials such as diamond and glass [36; 37]. See R. R. Gattass and E. Mazur for a recent overview of ultrafast laser pulse applications in dielectric material modification [38]. While there are a large number of applications of femtosecond-laser pulses, these pulses can also cause unwanted destruction of optical elements such as lenses and mirrors. The presence of dust, impurities, damage at the surface or in the material bulk of the optical elements, or hot spots in the beam profile of the laser can lead to the destruction well below the destruction threshold of the optical element due to the same processes that can be utilized to process optical materials. These same processes can limit the maximum attainable peak pulse energy of a given laser system. In order to effectively apply ultrafast laser pulses for precise material modification, while

avoiding unwanted effects, detailed knowledge of the nature of the ultrafast pulse-matter interaction and the material response (*e.g.* the formation of a free carrier gas) is required.

The energy deposition processes are commonly described in terms of plasma generation (or dielectric breakdown) in the material [39–42], which in turn causes a strong absorption in an initially transparent medium. This phenomenon has now been investigated for 80 years starting with the work of von Hippel [43] with large static fields [45] and the theoretical work of Fröhlich and co-workers [44].

A major breakthrough in this area came with the introduction of the laser, which made strong oscillating fields available. In 1971 Yablonovitch used a CO_2 laser with a 7 ns pulse width ($\lambda_L = 10.6$ μm) to induce a dielectric breakdown in alkali-halide crystals. The results confirmed earlier investigations made using static fields of similar strength in the same type of crystal [46; 47]. In the following years experimental investigations of optical breakdown were performed on a wide variety of materials at multiple wavelengths and pulse widths [48–56]. These studies identified impact ionization, where a hot electron in the conduction band excites an electron from the valence band by means of collision into the conduction band, as the dominant electron generation process. Since this process depends on the number of electrons in the conduction band it is also called avalanche process. For pulses longer than 5 ps the presence of "lucky electrons" was assumed, *i.e.* a small population (10^8 cm^{-3}) of free electrons in the conduction band were postulated as necessary to start the avalanche process. The first study in quartz using pulses on the femtosecond regime (Full Width Half Maximum (FWHM) $>$ 150 fs) was conducted by Du *et al.* in 1994; This study determined that impact ionization was the dominant electron generating process [57].

In 1965 Keldysh proposed multiple excitation mechanisms [58] for dielectrics with a bandgap energy large compared to the photon energy, *i.e.* he posited tunneling and multi-photon ionization as possible electron generation processes in the presence of strong oscillating fields. In 1996 Stuart *et al.* proposed a rate equation model to describe the electron generation in ultrashort pulse irradiated transparent dielectrics based upon their *post mortem*

study of surface destruction using focused femtosecond laser pulses [39]. This model included a simplified term for the multi-photon excitation as well as a term describing impact ionization. No "lucky-electrons" were needed to initiate the avalanche process in this model.

With the use of ultrafast pulses, *in-situ* experiments became more challenging because the time resolution of existing measurement techniques was not sufficient to resolve the processes involved. Most studies on ultrafast laser pulse material interaction were performed by investigating the *post mortem* damage on the material surface [6; 7; 39; 59–65; 67–75] or the bulk [1; 2; 76], therefore allowing the investigation the damage threshold as a function of pulse width and energy. A few studies investigated the change in optical properties of the material by observing the total absorption in the material [77; 78], or detecting the emission from the generated plasma, and the total transmission through the sample, as a function of pulse energy to determine the threshold for dielectric breakdown [57; 79; 80]. Other studies have characterized the properties of the plasma that is generated as result of the field - matter interaction [81–85]. Several groups have combined *post mortem* analysis of the damage tracks and photography of the plasma emission with pulse propagation simulations to investigate the electron density as a function of propagation distance inside the material [86–91]. The use of pump and probe techniques has made it possible to investigate the *in-situ* change of the optical and spectral properties of the material [92–102]. The change in plasma density as a function of position on the surface and time has also been investigated using pump and probe techniques [103–105]. While the change in the material has been extensively investigated experimentally, the corresponding change in the laser pulse was mainly studied using computer simulations [87; 89; 102; 106–121], which also provided predictions of the electron plasma density for different input pulse energies and shapes. These results were often compared to experimental data, *e.g.* damage threshold, damage tracks or plasma emission.

The first *in-situ* measurement of the breakdown process at the picosecond-time scale was performed using a streak camera by Anthens *et al.* in 1977 [53]. To extend the concept of the streak camera into the sub-ps range in the visible spectral range is challenging, and its

development decelerated with the emergence of other pulse measurement methods. Simple autocorrelation measurements have replaced the streak camera [122–127] for ultrafast pulse characterization. While autocorrelation can provide information on the pulse width, it cannot give a definite answer about the pulse shape. An autocorrelation measurement yields the information about the amplitude of the field only and does not include any phase information. If the pulse shape is known (or assumed), autocorrelation can be used to determine the pulse width. A cross-correlation measurement can be even more effective if a well-defined pulse is available to characterize an unknown pulse. To this end, some experiments split the beam before the experiment and use one pulse as a reference and the other as the probe pulse. This has the advantage that even though the original pulse shape might not be known, changes in the pulse shape can be detected [128].

To fully characterize the electric field of the pulse, it is necessary to obtain information about the phase. One way of obtaining this information is by spectrally analyzing the autocorrelation signal as a function of the time delay between the pulses. In this experiment both the phase and the amplitude information are captured and can be extracted by means of a phase retrieval process [129; 130]. This technique was first applied to measurement of ultrafast pulses by Trebino *et al.* and is called Frequency Resolved Optical Gating (FROG)[130].

Recent studies on ultrafast laser pulse - material interaction have used interferometric methods (such as Spectral Phase Interferometry for Direct Electric-field Reconstruction (SPIDER) [131]), transient absorption or cross-correlation signals to make *in-situ* observations [99–102; 128; 132–138]. In most previous studies using these techniques, the sample thickness was well beyond the Rayleigh length as well as the self-focusing length of the pulse [99–102; 132–137], making it impossible to distinguish between the changes due to the interactions near the surface and the cumulative changes due to the interactions which take place in the bulk of the medium.

The results presented in this dissertation are an extension of these earlier studies. The FROG technique is used to time resolve the complex field of the pulse both before and after

the interaction with a thin medium, yielding insight into the near surface processes involved. The results presented in this dissertation are obtained using second harmonic generation (SHG) - FROG and are compared to results from 3D+1 computer simulations of the pulse propagation within the sample.

The structure of this dissertation is as follows: In the following chapter a classical theory of the interaction between the ultrashort pulse and the transparent dielectric is introduced. The fundamentals of nonlinear optics are presented, and are followed by a discussion of the Drude-Lorenz Model, which is used to predict the optical properties of a free-carrier plasma. The generation of the plasma due to the interaction with the laser pulse is modeled with a more detailed rate equation than that used by Stuart *et al.* [39], which includes the full Keldysh model for photoionization [58] and the Rethfeld Model for impact ionization [41]. This discussion is then followed by a description of the "pulsesuite" package, which has been developed by the Dennis Group, to simulate both the pulse propagation and the pulse-matter interaction and thus can be used to interpret the experimental results.

In Chapter 3 the FROG method used in this dissertation is described, as is the experimental setup with which the data was taken, and the code that controls the experiments. A description of the analysis software is provided in the last section of that chapter, which includes a discussion of the phase retrieval code used to interpret the FROG traces and the algorithm that is used to generate FROG traces of the computer simulation results.

The results are discussed in the fourth chapter, starting with the beam profiles that are measured before and after the sample at different pulse energies. The complex fields found using the phase retrieval code on the experimental FROG traces are then compared with the results of the computer simulation. Finally, the FROG traces that show spatio-temporal dependences are compared to the artificial FROG traces generated from the computer simulation results. The fifth chapter is reserved for a summary of the results, conclusions, and some suggestions for future work.

Chapter 2

Ultrafast Laser Pulse - Transparent Dielectric Interaction

Most of our everyday experience with light and its interaction with matter can be described using the formalism of linear optics [139; 140]. The experiments and computer simulations described in this dissertation go well beyond what can be understood by this simple formalism. This chapter introduces the relevant additional relevant nonlinear optical effects [141; 142]. The beam propagation method that was used to simulate the experiment [151] in order to interpret the experimental results is introduced together with necessary extensions to account for the nonlinearities.

The interactions between field and matter not only modifies the properties of the electromagnetic field but lead to changes of the optical properties of the material. For ultrashort pulses these changes can happen in roughly four time regimes. The first is the instantaneous change of the material due to the field interaction with the polarization of the material. Instantaneous in this context means that the change in the material occurs fast compared to the change in amplitude in the field. This dissertation investigates changes that occur on the order of the pulse duration, *e.g.* the generation of a free-carrier plasma. Due to these processes, energy can be transfered to the material, leading to energy dissipation and additional processes such as melting or material stress fracturing, which occur on timescales from picoseconds to microseconds. The latter effects can be mostly neglected for the experiments described here, since the pulse duration is too short and the laser repetition rate is too low to measure effects on this time scale. Multi-pulse damage can occur at lower pulse energies due to the cumulative effects of many laser pulses, which ultimately leads to a breakdown

of the material. The experiments presented in this dissertation do indeed expose the material to multiple laser pulses, however besides a lowering of the damage threshold, no other effects from accumulated damage was observed. Depending on the material and the amount of energy deposited, this can then lead to permanent changes in the optical properties of the material. It is important to distinguished between reversible and irreversible material modifications [66; 91]. The former is evidenced by a localized change in the refractive index and can be removed by annealing the material (at 900°C for fused silica) [33; 66]. Irreversible damage cannot be removed by heating and can take different forms (*e.g* birefringence, ablation, complete local structural breakdown). Both kinds of damage can be induced by a single laser pulse, but the damage threshold is lowered for multiple pulse exposure [66]. This kind of material modification opens up new and exciting possibilities for material machining, such as the laser drilling of diamonds, waveguide writing in transparent material, and laser polishing of thermosensitive transparent materials [1–37]. Ultrashort pulses can therefore be used both to cause and to study optical damage. The interaction between the laser pulse and highly excited electrons within the material is complex and to date many questions remain unanswered.

In this dissertation, changes in the laser pulse will be measured in order to gain new insight on the material response that takes place on the timescale of the laser pulse. In this chapter, the relevant nonlinear effects will be discussed, as will the material response that results from the interaction. In sections 2.1 and 2.2 the effects on the electromagnetic field are discussed. The mechanisms responsible for changing the optical properties of the material are introduced in sections 2.3 and 2.4, where the simulation method and its predictions are also presented.

2.1 Nonlinear Optics

In the macroscopic Maxwell equations describing field-matter interactions in a dielectric material, the electric displacement field $\vec{D}$ is related to the electric field $\vec{E}$ by the constitutive relation in the frequency domain, *i.e*

$$\begin{aligned} \vec{D}(\omega) &= \epsilon(\omega)\vec{E}(\omega) \\ &= \epsilon_0\vec{E}(\omega) + \vec{P}(\vec{E}(\omega)) \end{aligned} \tag{2.1}$$

where $\vec{E}$ is the total electric field, ω is the frequency and $\vec{P}$ the polarization. The polarization depends on the material properties and is in principle a complicated function of the total electric field. In many cases the polarization can be expanded in power of the field:

$$\begin{aligned} \vec{P}(\omega) = &\epsilon_0\chi^{(1)}(\omega)\vec{E}(\omega)+ \\ &+ \epsilon_0 \int_{-\infty}^{\infty} \chi^{(2)}(\omega, \omega-\omega', \omega')\vec{E}(\omega-\omega')\vec{E}(\omega')d\omega'+ \\ &+ \epsilon_0 \int_{-\infty}^{\infty} \chi^{(3)}(\omega, \omega-\omega'-\omega'', \omega', \omega'')\vec{E}(\omega-\omega'-\omega'')\vec{E}(\omega')\vec{E}(\omega'')d\omega' d\omega''+ \\ &+ ... \end{aligned} \tag{2.2}$$

The first, second and third order electric susceptibility, $\chi^{(1)}$, $\chi^{(2)}$, and $\chi^{(3)}$, are tensors of rank 2, 3, and 4, respectively and describe the interaction of the electric field with the material.

Since this dissertation only considers light - matter interactions caused by ultrashort pulses, nonlinear effects that take place on timescales significantly longer than the pulse length are neglected; for a general overview see [142]. For monochromatic fields Eq. 2.2 can be simplified into a more common form

$$\begin{aligned}\vec{P}(\omega) = \epsilon_0\chi^{(1)}(\omega)\vec{E}(\omega) + \epsilon_0\chi^{(2)}(\omega,\omega_1,\omega_2)\vec{E}(\omega_1)\vec{E}(\omega_2)+ \\ + \epsilon_0\chi^{(3)}(\omega,\omega_1,\omega_2,\omega_3)\vec{E}(\omega_1)\vec{E}(\omega_2)\vec{E}(\omega_3)+ \\ + ...\end{aligned} \tag{2.3}$$

In the work presented in this dissertation a $\sim$ 140 fs full width half maximum (FWHM) focused laser pulse with $\sim$ 50 μJ pulse energy is used as a primary light source. The highest intensities ($I \approx 10^{17}$ Wm^{-2}) used in the experiment give rise to several nonlinear effects, which are introduced in the following subsections.

2.1.1 Kerr Effect and Self-Focusing

The refractive index n is a function of the permittivity $\epsilon(\omega)$:

$$n = \sqrt{\epsilon(\omega)}; \tag{2.4}$$

for low intensities it follows from Eq. 2.1 that Eq. 2.4 can be approximated with

$$n = \sqrt{1 + \chi^{(1)}}. \tag{2.5}$$

At sufficiently high field strengths the nonlinear terms in Eq. 2.3 are no longer negligible and the refractive index n of the material becomes a function of the field, [140; 141]

$$n = \sqrt{1 + \chi_{eff}(E)}. \tag{2.6}$$

Here χ_{eff} is the effective electric susceptibility in the dielectric. For isotropic materials the even order terms in Eq. 2.3 vanish from symmetry arguments, so that the linear and the third order terms dominate. This is called a Kerr effect, and it means that the refractive index has now become a function of the intensity for a single external field $\vec{E}$.

$$\vec{P} \simeq \epsilon_0\chi_{\text{eff}}E \quad \text{with} \quad \chi_{\text{eff}} = \chi^{(1)} + \chi^{(3)}|E|^2, \tag{2.7}$$

using Eq. 2.4,

$$n \approx \sqrt{1 + \chi^{(1)} + \chi^{(3)}|E|^2}. \tag{2.8}$$

This can be further approximated to give

$$n(I) \simeq n_0 + n_2 I. \tag{2.9}$$

This $n(I)$ is the effective refractive index for a material with a linear refractive index $n_0 = \sqrt{1+\chi^{(1)}}$ and nonlinear refractive index n_2, and has been irradiated with an intensity distribution $I(\vec{x}, t)$. For beams with Gaussian or Gaussian-like beam profiles, the Kerr effect causes a variation of the refractive index due to the beam profile and in turn acts like a lens on the beam. The beam path in the center of the beam is increased with respect to the edges of the beam, acting as a focusing lens on the beam. As the beam diameter decreases, the field intensity increases, further enhancing the lensing effect in material and the beam. In the absence of a limiting effect such as plasma generation, this leads to the catastrophic collapse of the beam, at which point additional higher order nonlinear effects such as multi-photon absorption start to become important. Marburger [51] has shown that the pulse self-focusing process is a peak-power rather than a peak-intensity dependent process for the case when dispersion, absorption and plasma generation are assumed to be negligible. The critical power P_{cr} can be estimated for Gaussian beam profiles using [51] :

$$P_{\text{cr}} = \frac{3.77\lambda^2}{8\pi n_0 n_2}. \tag{2.10}$$

The factor 3.77 is for Gaussian beams only.

2.1.2 SELF PHASE MODULATION

The electric field can be described in the form of a complex field envelope $E(t) = |E(t)|e^{i\phi(t)}$, with $\phi(t)$ being the temporal phase. The time derivative of the temporal phase $\phi(t)$ of the field gives the instantaneous frequency $\omega(t)$ [143]:

$$\omega(t) = -\frac{\partial\phi(t)}{\partial t}. \tag{2.11}$$

The phase is a function of the refractive index

$$\phi(t) = \omega_0(t - n(I)l/c) \tag{2.12}$$

with $n(I)$ defined in Eq. 2.9. The instantaneous frequency becomes a function of the intensity and therefore for a finite field of t:

$$\omega(t) = \omega_0 \left(1 - \frac{l}{c}\frac{dn(I(t))}{dt}\right) = \omega_0 \left(1 - \frac{l}{c}\frac{dn}{dI}\frac{dI}{dt}\right) \tag{2.13}$$

with ω_0 being the carrier frequency and l being the interaction length and c the speed of light in vacuum. From Eq. 2.13 it follows that the spectrum broadens according to the rate of change in intensity and interaction length. In the case where $\chi^{(3)} > 0$ the spectrum of the leading edge of the pulse is shifted towards lower frequencies, while the spectrum of the trailing edge shifts to higher frequencies. Together with chromatic dispersion in the material, this results in a broadening of the pulse in time as well as in frequency.

2.2 Drude-Lorenz Model

In order to understand who the generated free carrier plasma affects the laser pulse, it is necessary to describe the optical properties of the free carrier plasma for different densities and carrier frequencies. In this dissertation the Drude-Lorenz model [144; 145] is used, which defines the dielectric function $\epsilon(\omega)$ as:

$$\epsilon(\omega) \simeq \epsilon_0(1 + \chi_b^{(1)} + \chi_p) \tag{2.14}$$

Here $\chi_b^{(1)}$ is the susceptibility due to the bound charges, χ_p is the plasma susceptibility as given by the Drude-Lorenz model:

$$\epsilon(\omega) = \epsilon_b\epsilon_0 + \epsilon_0\chi_p = \epsilon_b\epsilon_0 + \frac{Nq^2}{m_q^*(\Omega_0^2 - \omega^2 - i\omega\gamma)} \tag{2.15}$$

where $\epsilon_b = 1+\chi_b^{(1)}$, N as the carrier density per unit volume, m_q^* and q are the effective mass and charge respectively. The resonant frequency of the carrier is given by Ω_0 while is the ω_0 is the frequency of the driving field. The material dependent coefficient is the damping constant $\gamma = 1/\tau_c$, with τ_c being the collision time of the electrons, which describes the interaction rate of the electron with other electrons, the lattice, and photons of the driving

field. For electrons in the conduction band one can treat the carriers as free (*i.e.* no restoring force), in which case the resonant frequency $\Omega_0 = 0$ and Eq. 2.15 can be written as:

$$\epsilon(\omega) \simeq \epsilon_b\epsilon_0 - \frac{iNq^2}{m_q^*(i\omega^2 - \omega\gamma_0)} = \epsilon_b\epsilon_0 - \epsilon_0\left(\frac{\omega_p^2}{\omega^2 + i\omega\gamma_0}\right) \tag{2.16}$$

where $\omega_p = \sqrt{\frac{Nq^2}{\epsilon_0 m_q^*}}$ is the plasma frequency. For $\omega\gamma_0 \ll 1$

$$\epsilon(\omega) \sim \epsilon_0\left(\epsilon_b - \frac{\omega_p^2}{\cdot}\omega^2\right) \tag{2.17}$$

2.2.1 Absorption due to a free carrier gas

If a plasma is present ($\omega_p > 0$), which means $\epsilon(\omega)$ is decreased and the real refractive index n is lowered:

$$n(\omega) = \sqrt{\epsilon(\omega)/\epsilon_0} \tag{2.18}$$

Additionally, an imaginary part is introduced to the refractive index n, *i.e.* the free carrier gas of density N becomes absorbing. For the case where the plasma frequency is lower than the frequency of the driving field, $\omega_p < \omega$, the refractive index n is reduced in the presence of a free carrier gas, which can counteract the increase of n due to the Kerr effect and therefore prevent the catastrophic collapse of the beam in the case of soft focusing.

When a dielectric material with free carrier gas density $N \ll 10^{19}$ cm^{-3} is exposed to a high intensity field (as from a focused ultrashort pulse), the free carrier gas density will change rapidly, leading to a change in the plasma frequency and subsequent change in the refractive index. The absorption due to the plasma becomes very effective when the plasma frequency becomes closer to the carrier frequency. Most authors define the destruction threshold for the material accordingly as the point when the carrier frequency ω_0 is equal to the plasma frequency, which is the case for

$$N_D = \frac{\omega_0^2}{\omega_p^2}N = \frac{\epsilon_0\omega_0^2 m_q^*}{q^2} \tag{2.19}$$

From Eq. 2.19 the threshold for fused silica (Si_2O) is found to be $N_D \sim 10^{21}$ cm^{-3} at center wavelength of $\lambda_0 = 800$ nm [128]. For higher plasma densities, the absorbed energy

will permanently modify the material, which can be the observed *post mortem* as visible damage. Sudrie *et al.* [89] report that permanent modifications are also possible well under the critical density .

2.2.2 Absorption due to free-carrier generation

Transparent insulating dielectric materials are characterized by the band gap energy U, which is larger than the photon energy hc/λ in the visible region. Consequently, those materials have very few electrons in the conduction band at room temperature [146]. Thus electrons in the valance band can absorb individual visible photons only in the presence of defects (*e.g.* color centers), which provide locally allowed energy levels within the band gap. However, as will be shown later, an electron can be excited across the band gap in the presence of a strong driving field due to photoionization, tunneling, or avalanche processes (Fig. 2.1 (a),(b), or (c) respectively). Here multiple photons are involved in the excitation process. Once in the conduction band the electron can participate in single photon absorption.

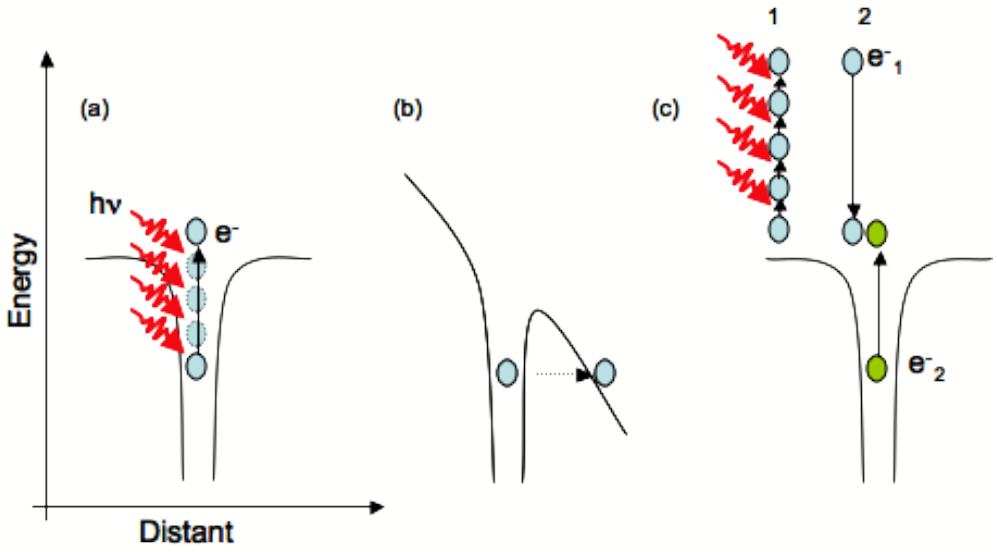

Figure 2.1: (a) illustrates the electron excitation by simultaneous absorption of multiple photons. (b) illustrates the bending of the potential by an outside field, due to which the electron tunnels out of the potential well. (c.1) shows the sequential absorption of photons by an electron (e_1^-) in the conduction band, which then excites a valence-band electron (e_2^-) to the conduction band by impact ionization (c.2).

Not only do these processes populate the conduction band, they also absorb energy from the driving field, the resulting change in pulse intensity can be found from [39]:

$$\frac{\partial I}{\partial z} = -\sigma N_{\mathrm{c}} I - W_{\mathrm{PI}} U, \tag{2.20}$$

where z is the direction of propagation of the driving field, $W_{\mathrm{PI}} = (N - N_c)/N$ is the multi-photon rate (from the theory of Keldysh [58]) with N_c being the free-carrier density in the conduction band and N being the total charge density calculated from the molecular density. It is assumed that each atom contributes maximum one electron, since the binding energy is increased for the remaining electrons in an ionized atom. U is the band gap energy, and σ is the cross-section of single photon absorption due to a photon-electron-phonon process (inverse Bremsstrahlung); *i.e.*

$$\sigma = \frac{q^2 \tau_c}{n_0 c \epsilon_0 m^* (1 + \omega_0^2 \tau_c^2)}.$$

The linear index of refraction is $n_0 = k_0 c/\omega_0$ with k_0 being wave vector of the incoming field and τ_c the electron collision time, c the speed of light in vacuum, m_q^* and q the effective mass and charge respectively, and ω_0 the carrier frequency of the driving field.

2.2.3 Filamentation

A filament is usually defined as a long, thin region with a visible plasma density in an environment with lower or no plasma density. Since earlier computer simulation and experimental work [87; 89; 109; 138; 147] indicate that ultrashort pulses can lead to the formation of filaments in fused silica, a short introduction into the formation mechanisms is provided.

A filament is formed when self-focusing causes the intensity to increase to a level where a free carrier gas is generated; this counteracts the nonlinear increase of the refractive index (see Eq. 2.16), preventing a catastrophic collapse of the beam. The self-focusing and plasma processes balance each other creating a long region with a visible plasma density. A comprehensive review of filamentation is given in reference [147].

For the experiments described in this dissertation a combination of short sample length with soft focusing ensured that filamentation was minimized.

2.3 Electron Generation

Since optically transparent dielectrics have band gap energies $U > 5$ eV, single photons in the visible region cannot excite an electron from the valance band into the conduction band *i.e.* absorption due to one-photon photoionization is negligible. However, electrons can still gain the energy needed for the excitation processes from the field. The electron population in the conduction band can be found using a simple rate equation first introduced by Stuart *et al.* [39] and later modified by Rethfeld [41]:

$$\frac{\partial N_c(x,t)}{\partial t} = \left[\left(\frac{\partial N_c(x,t)}{\partial t}\right)_{(PI)} + \left(\frac{\partial N_c(x,t)}{\partial t}\right)_{(AI)}\right] \frac{(N - N_c(x,t))}{N} - N_c(x,t)/\tau_e \qquad (2.21)$$

Where $N_c(x,t)$ is the electron density in the conduction band as a function of position in the beam and time, and N the molecular density (with one available electron per atom). In this dissertation $\left(\frac{\partial N_c}{\partial t}\right)_{PI}$ and $\left(\frac{\partial N_c}{\partial t}\right)_{AI}$ account for multi-photon / tunnel ionization after Keldysh [58], and avalanche ionization after Rethfeld [41]. The last term in Eq. 2.21 accounts for recombination of the generated carriers with τ_e being the reciprocal of the recombination rate. In the following, the physics underlying each term in Eq. 2.21 is discussed, as are the effects of the electron gas on the optical properties of the host material.

2.3.1 Keldysh Model

Even though a material is transparent for a certain region of the spectrum, that does not mean that there is no absorption possible. The process of tunneling ionization is always possible. Here an electron tunnels through the energy barrier into the conduction band. Its rate W_{PI} is determined by the magnitude of the electric field $|\vec{E}|$ and the ionization potential U, if the field contains frequency components lower than [58]:

$$\omega < \omega_T = \frac{e|\vec{E}|}{\sqrt{m_e^* U}} \qquad (2.22)$$

Here e is the electron charge, m_e^* is the effective electron mass and U is the ionization potential (or band gap). For fields with frequencies lower than the tunneling frequency $\omega_T = 1/\tau_t$, with τ_t being the average time the electron needs to tunnel through the potential barrier, the tunneling process can be seen as instantaneous, since the electron can tunnel through the potential barrier in less than one optical cycle. For driving fields with higher frequencies, the tunneling effect depends on the frequency of the driving field as well as its amplitude.

Tunneling is not the only possible photoionization process in transparent media. The electron can also be excited by absorbing multiple photons simultaneously. The multi-photon ionization rate scales with $\sigma_k I^k$, I being the field intensity, k the number of photons required, and σ_k the cross section of the k-photon absorption. As Keldysh has shown [58], the multi-photoionization and tunneling ionization are extreme cases of a general ionization process (see Fig. 2.2). The general ionization rate is given by:

$$W_{\mathrm{PI}}(|E|) = \frac{2\omega_0}{9\pi}\left(\frac{m_e\omega_0}{\sqrt{\gamma_1}\hbar}\right)^{3/2} Q(\gamma, x)\exp(-\varpi\langle x+1\rangle) \tag{2.23}$$

The notation $\langle\rangle$ denotes the integer part. With $\gamma = \omega_0\sqrt{m_e U/e_0|\vec{E}|}$ being the Keldysh parameter from which $\gamma_1 = \gamma^2/(1+\gamma^2)$ and $\gamma_2 = 1-\gamma_1$ are found. Here the variables are defined as $\varpi = \pi(K(\gamma_1) - E(\gamma_2))/E(\gamma_2)$ and $x = (2U/\pi\omega)(\sqrt{1-\gamma^2}/\gamma)E(\gamma_2)$, with K and E being complete elliptical integrals of the first and second kind as defined in [148]. Q is defined as:

$$Q(\gamma, x) \equiv \sqrt{\frac{\pi}{2K(\gamma_2)}}\sum_{n=0}^{\infty} exp(-n\varpi)\Phi(\sqrt{\vartheta(n+2\nu)}) \tag{2.24}$$

here, $\vartheta = \nu/4K(\gamma_2)E(\gamma_2)$ and $\nu = \langle x+1\rangle - x$. The Dawson function is
$\Phi(z) = \int_0^z \exp(y^2 - z^2)dy$.

Note that for $\gamma \gg 1$ the ionization process can be described simply as a multi-photon process, while for $\gamma \ll 1$ the ionization happens through a tunneling process. Since for the cases investigated in this dissertation $\gamma \sim 1$, no such distinction can be made and the full Eq. 2.23 is used.

The ionization rate $\left(\frac{\partial N_c}{\partial t}\right)_{PI}$ in Eq. 2.21 due to the tunneling/multi-photon picture given in Keldysh's paper is calculated using

$$\left(\frac{\partial N_c}{\partial t}\right)_{\mathrm{PI}} = W_{\mathrm{PI}}(|\vec{E}|, \omega_0)U \tag{2.25}$$

so that the ionization rate depends on the gap energy U, the amplitude $|\vec{E}|$, and frequency ω_0 of the driving field.

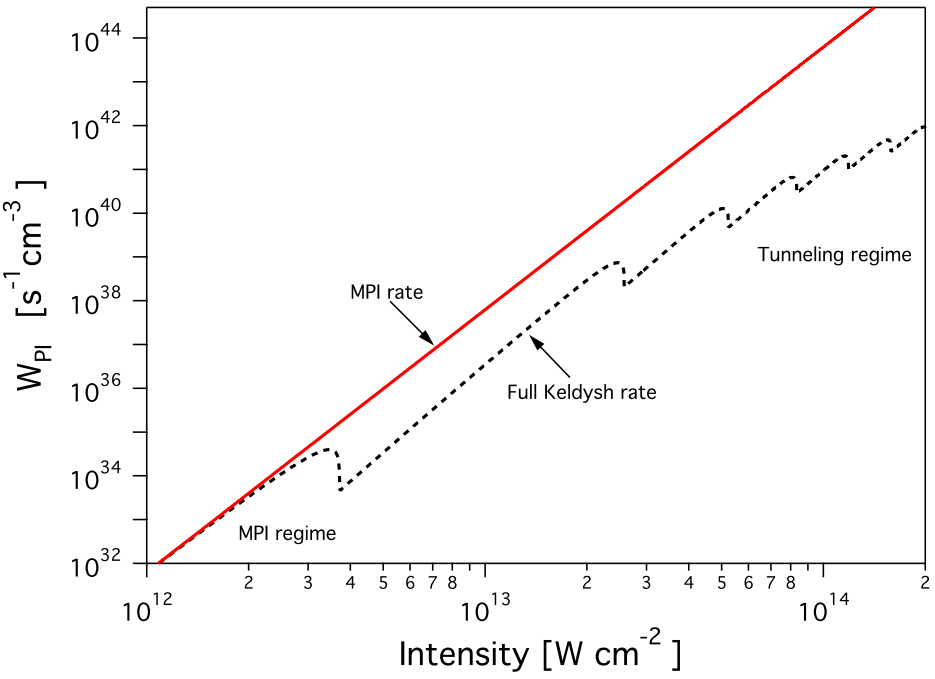

Figure 2.2: The photoionization rate W_{PI} as a function of the intensity I for the multi-photon ionization rate alone (solid red line) and that for the full Keldysh picture (dashed black line).[116]

2.3.2 Avalanche Process

Once an electron has been excited to the conduction band it can absorb single photons due to the continuous nature of the conduction band by the process of inverse bremsstrahlung absorption. It is assumed that once the electron has absorbed sufficient energy to excite an additional electron from the valence band into the conduction band this process takes immediate effect. Once the free electron is in a high energy state within the conduction band

the hot electron transfers part of its kinetic energy by impact ionization to an electron in the valence band, which is in turn excited to the bottom of the conduction band. The formerly hot electron has lost energy and is now back at the bottom of the conduction band and the net electron density in the conduction band is increased. The electrons in the conduction band absorb one photon at a time [41]. This means that one electron has to go through a sequence of absorptions before it has sufficient energy to excite an electron from the valence band into the conduction band as shown in Fig. 2.3 [41]. The rate at which an electron in the conduction band absorbs photons, $W = \sigma(\varepsilon)I$, depends linearly on I and on the inverse bremsstrahlung coefficient $\sigma(\varepsilon)$, which also depends on the electron energy above the bottom of the conduction band ε. This means that the number of electrons in the conduction band with energy $\varepsilon_{k_{\max}} > U$ which is the case for $k_{\max}$ absorbed photons, depends linearly on the intensity. The avalanche ionization term in the rate equation 2.21, $\left(\frac{\partial N_c}{\partial t}\right)_{\mathrm{AI}}$ is thus

$$\left(\frac{\partial N_c}{\partial t}\right)_{\mathrm{AI}} = \tilde{\alpha} N_k \tag{2.26}$$

with $\tilde{\alpha}$ being the ionization probability. Note that only electrons with energy sufficient to ionize a valence band electron contribute to this process. In a simple model, the conduction band is represented by $k_{\max}+1$ energy levels. The k^{th} level is populated with N_k electrons per unit volume. The population development of all the $k_{\max}+1$ energy states is then described by the rate equations [41]:

$$\dot{N}_0 = W_{\mathrm{PI}}(|E|) + 2\tilde{\alpha}_k N_k - W(\varepsilon_0) N_0 \tag{2.27}$$

$$\dot{N}_{\mathrm{k}} = W(\varepsilon_{\mathrm{k}-1}) N_{\mathrm{k}-1} - W(\varepsilon_{\mathrm{k}}) N_{\mathrm{k}} \quad \text{with} \quad k = 1..k_{\max-1} \tag{2.28}$$

$$\dot{N}_{\mathrm{k}_{\max}} = W(\varepsilon_{\mathrm{k}_{\max}-1}) N_{\mathrm{k}_{\max}-1} - W(\varepsilon_{\mathrm{k}_{\max}}) N_{\mathrm{k}_{\max}} - \tilde{\alpha}_k N_k \tag{2.29}$$

$W(\varepsilon_{\mathrm{k}-1}) N_{\mathrm{k}-1}$ is the rate at which electrons are excited into the k level, while $W(\varepsilon_{\mathrm{k}}) N_{\mathrm{k}}$ gives the rate the electrons move from level k into the higher level $k+1$.

The change of the electron density at the bottom of the conduction band is described by Eq. 2.27. Eq. 2.28 describes the population of electrons in the k level, where the electron has the energy corresponding to k photons. Eq. 2.29, which describes the behavior of the

population with more than the critical energy $\varepsilon_{k_{\max}}$, where the electrons have sufficient energy to excite one electron from the valence band into the conduction band.

The avalanche process often excites the majority of electrons during the tail of the pulse when the electron density is high and the multi-photon ionization decreases nonlinearly with the intensity [41]. Avalanching is therefore the dominant electron excitation process in pulses that are longer than a few picoseconds, while its effect on the electron density can be neglected for pulses shorter than 50 fs. [40; 41]

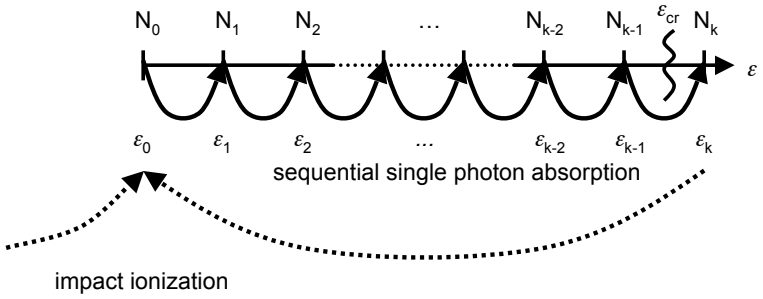

Figure 2.3: Once an electron is in the conduction band, it can absorb single photons and thus gain energy. When the electron has sufficient energy to excite an electron from the valence band into the conduction band ($\varepsilon_{\mathrm{cr}}$) it does so through impact ionization.[40; 41]

2.3.3 Recombination Rate

Since the electron lifetime in the conduction band is limited, electrons in the conduction band fall back to the valence band as a result of spontaneous emission. This recombination process is accounted for in the rate equation Eq. 2.21 by the last term, which only depends on the lifetime of the electrons in the conduction band, τ_e, and the conduction band electron population density, N_c.

Note that this process is the only process that accounts for the depopulation of the conduction band in the rate equation. Lattice defects (for example color centers and impurities) can lead to more rapid non-radiative recombination processes. The electron lifetime for a given material can be challenging to measure for some materials. This has lead to a wide

range of published values spanning more than two orders of magnitude from 0.2 fs [73; 104] to 23.3 fs [89] for fused silica. Depending on the material the lifetimes can range from one femtosecond up to several microseconds [73; 78; 88; 89; 91; 101; 104; 109; 138; 147; 149; 150].

2.4 Pulse Propagation Simulations

In order to interpret the experimental results presented in this dissertation, the experiments were closely modeled using the "pulsesuite" code, which has been developed by the Dennis Group [116]. This 3+1D (three spatial dimensions and time) code simulates the propagation of a specified femtosecond pulse through a medium of given length using a modified nonlinear Schrödinger equation (NLSE), which is solved simultaneously with the differential equations describing the evolution of the material.

The code allows the user to specify the optical properties, the resolution and step size inside the material, as well as the included nonlinear effects. Simulations with different material properties were performed and compared to the experimental results.

2.4.1 nonlinear Schrödinger Equation

To simulate the propagation of the complex field envelope $\vec{E}(\vec{x},t) = |\vec{A}(\vec{x},t)|e^{i(\vec{k}\vec{x}-\omega t)}$, with $A(\vec{x},t) = |A(\vec{x})|e^{i\phi t}$, a modified nonlinear Schrödinger equation (NLSE) is solved for a polarized field $E(t)$ [151]:

$$\frac{\partial E}{\partial z'} = \frac{i}{2k_0}\hat{T}^{-1}\nabla_\perp^2 E + i\hat{D}_b E + i\frac{k_0 n_2}{n_0}(1-f_r)\hat{T}IE \tag{2.30}$$

$$+i\frac{k_0 n_2}{n_0}f_r\hat{T}\left[\int_{-\infty}^{\tau} d\tau' R(\tau-\tau')I(\tau')\right]E - \frac{W_{\mathrm{PI}}U}{2I}\xi - \frac{\sigma}{2}(1+i\omega_0\tau_c)\hat{G}^{-1}[\rho\xi]. \tag{2.31}$$

All parameters are described in Table 2.1. The first two terms describe the diffraction and dispersion of the field due to the bound charges respectively. The third term accounts for the instantaneous Kerr effect and steepening, while the fourth term is the contribution of the stimulated Raman scattering to the nonlinear polarization. The fifth term accounts for the photoionization and the last term describes the dispersion due to free electrons.

The NLSE was integrated using a split step method which included a linear step and a nonlinear step. The diffraction and dispersion terms are calculated in the linear step, which is solved using a Crank-Nicoloson algorithm [152], while the remaining terms were calculated in the nonlinear step, which is solved using a fourth-order Runge-Kutta method [152]. A more detailed description of the computer simulation algorithm is provided in Reference [151]. The computer simulation results presented in this dissertation were performed using a 256 $\times$ 256 spatial grid with 512 time points. The spatial resolution was chosen to be $\delta x = 10w_r/256$ and the temporal resolution was chosen to be $\delta t = 10\tau_0/512$, where w_r and τ_0 are the $1/e^2$ width of the beam and pulse respectively. The pulse parameters were chosen to be as similar as possible to the experimental data. The pulse shape and the temporal phase were derived from a measured pulse shape using SHG-FROG. A beam profile was measured in the experiment before the first lens. This beam profile had sharp edges (due to the clipping by the detector) which were smoothed out at the edges using a super Gaussian function, in order to reduce unwanted diffraction effects in the computer simulation. The smoothed beam profile was than Fourier transformed to simulate the focusing of the beam at the sample surface, at which point the input field was constructed. The pulse powers chosen for the computer simulations were whenever possible, the same as those used in the experiments.

2.4.2 Simulations of fused silica

All experiments and computer simulations described in this dissertation were performed using fused silica as the sample material, since it is a comparatively well characterized material that is commonly used for optical elements and is consequently of great interest (*e.g* [1–4; 6–8; 10–12; 15; 16; 19; 23; 24; 29; 30; 39; 57; 73; 78; 87–89; 91; 100; 101; 104; 116; 128; 138; 149; 150; 154]). The sample thickness of 200 μm in the computer simulations was chosen to match to the sample thickness in the experiments. The other parameters for the computer simulation were taken from [138].

Table 2.1: The terms used to simulate the propagation of the ultrashort pulse.

	Description	Definition
E	Complex field envelope	$E(t) = \|E(t)\|e^{i\phi t}$
z'	Propagation direction	
$\tilde{\kappa}$	Complex wave vector	$\tilde{\kappa}(\omega) = \tilde{k}(\omega) + i\tilde{\alpha}(\omega)/2$
k_m	Derivative of $\tilde{k}$	$k_m = \frac{\partial^m \tilde{k}(\omega)}{\partial \omega^m}\|_{\omega_0}$
α_m	Derivative of $\tilde{\alpha}$	$\alpha_m = \frac{\partial^m \tilde{\alpha}(\omega)}{\partial \omega^m}\|_{\omega_0}$
$\hat{T}$	Steepening operator	$\hat{T} = 1 + i\frac{1}{\omega}\partial_\tau$
$\hat{T}^{-1}$	Inverse steepening operator	
ω_0	Carrier frequency	
e_0	Free carrier charge	
$\hat{D}_b$	Bound charge linear dispersion operator	$\hat{D}_b = i\frac{\alpha_0}{2} - \frac{\alpha_1}{2}\partial_1 + \sum_{\mathrm{m}=2}^{\infty} \frac{k_m + i\alpha_m/2}{m!}(i\partial_\tau)^m$
$\hat{G}^{-1}$	Inverse free charge dispersion operator	$\hat{G}^{-1} = \sum_{m=0}^{\infty} \left(\frac{i}{\omega_0} g\partial_\tau\right)^m = \left(1 + \frac{i}{\omega_0} g\partial_\tau\right)^{-1}$
I	Intensity	$I = (1/2)n_0 c\epsilon_0 \|\xi\|^2$
f_r	Fraction of the Raman contribution to the nonlinear polarization	
$R(\tau)$	Raman response function	$R(\tau) = \frac{\tau_1^2 + \tau_2^2}{\tau_1 \tau_2^2} e_{\tau/\tau_2} \sin \tau/\tau_1$
τ_1, τ_2	Adjustable parameters in the Raman response function	
n_0	Linear refractive index	
n_2	Second order nonlinear refractive index	
τ_c	Electron collision time	
τ	Retarded time	$\tau = t - z/v_g$
v_g	Group velocity	$v_g = 1/\partial_\omega k(\omega_0)$
W_{PI}	Photoionization rate per unit volume	
U	Band gap energy	
ρ	Time dependent charge density	

Table 2.2: The parameters used in the computer simulation [138].

Parameter	Description	Value and Units
n_0	Linear refractive index	1.45
k_2	GVD coefficient	361 fs^2W^{-1}
n_2	Nonlinear refractive index	2.48×10^{-16} cm^2W^{-1}
ε_{cr}	Band gap energy	9 eV
τ_c	Electron collision time	1.27 fs
m_q^*	Effective carrier mass	0.5 m_e
$\rho_{\max}$	Molecular density and maximum electron density	6.6×10^{22} cm^{-3}
τ_r	Electron recombination time	150 fs

2.4.3 Non-Symmetric beam profile

The 3+1D computer simulation enables pulses of different energies, shapes, and from non-symmetric beam shapes to be simulated. In particular, the computer simulation can use an asymmetric beam profile measured in the laboratory in order to model the experimental measurement as closely as possible.

Therefore, computer simulations in this dissertation use beam profiles and pulse shapes derived from measurements in the laboratory. For the computer simulations described in this dissertation, the approximation was made that there is no initial spatio-temporal dependence in the beam prior to propagating in the sample. This assumption is reasonable, since the FROG traces without sample and at low energies do not show any signs of spatio-temporal dependences and were yield a unique solution, which would not be the case otherwise.

Chapter 3

Considerations: Measuring and analyzing the shape of ultrashort pulses

In order to investigate the interaction of an ultrafast laser pulse with a transparent sample, it is desirable to measure the pulse shape itself, since intensity dependent nonlinear interactions between light and material lead to changes in the pulse shape. Knowledge of the change of the pulse shape due to the interaction yields information about the nature and strength of the interaction taking place.

Measurements of an event usually entail a correlation with a temporal response (gate) function of the detection system. The shorter the gate function is in time and the more often it is applied within the event duration, the better the time resolution of the measurement. If the gating function becomes comparable in temporal duration to the event of interest, or is not applied often enough, the time resolution suffers. When the exposure time of an optical detector (*e.g.* a film or CCD chip) is long compared with the event under measurement, that event cannot be temporally resolved. Solutions to this problem range from using a light flash, which is short compared with the event (a technique that was first used by Ernst Mach for measuring the pressure cone in front of a projectile traveling faster than sound [155]) to combining the information of multiple frames to regain the time resolution as is used in video sequences [156].

A solution for measuring time-resolved ultrashort pulses is not so easily achieved, since ultrafast optical pulses are usually the shortest events available in the laboratory. This chapter explains a technique called Frequency Resolved Optical Gating (FROG), which is used to overcome this difficulty; how it differs from previously established techniques; and the improvements made to this technique.

3.1 Using Frequency Resolved Optical Gating to measure ultrafast pulses

3.1.1 Advantages and disadvantages of Autocorrelation

A popular method for measuring extremely short events available is to gate the event with itself; this is called autocorrelation (AC) [122–127; 157]. The optical autocorrelation method uses a nonlinear process (often second harmonic generation (SHG)[125; 126]) to produce a correlation of the pulse with itself. The laser beam is split in two for this purpose. The reference beam, is delayed by a time τ with respect to the sample beam, as shown in Fig. 3.1. For the work described in this dissertation, the nonlinear process used is SHG, which depends on the intensity of the total field inside a nonlinear crystal. The total field is found by superposition:

$$\mathcal{E}_{\text{total}}(t,\tau) = \mathcal{E}_1(t) + \mathcal{E}_2(t-\tau) \tag{3.1}$$

$$\mathcal{E}(t,\tau) = \frac{1}{2}E(t,\tau)\exp\left[i(\omega t - \vec{k}_j\cdot\vec{r})\right] + \text{c.c.} \tag{3.2}$$

When calculating the polarization $\mathcal{P}$ using Eq. 2.2, the second term is given by:

$$\begin{aligned}\mathcal{P}^{(2)}(\omega_1,\omega_2,\vec{r},t_1,t_2) = \epsilon_0\chi^{(2)}(&\frac{1}{2}E_2(\vec{r},t_2)E_2^*(\vec{r},t_2) + \text{c.c.}+\\ &+\frac{1}{4}E_1^2(\vec{r},t_1)\exp\left[2i(\omega_1 t_1 - \vec{k}_1\cdot\vec{r})\right] + \text{c.c.}+\\ &+\frac{1}{4}E_2^2(\vec{r},t_2)\exp\left[2i(\omega_2 t_2 - \vec{k}_2\cdot\vec{r})\right] + \text{c.c.}+\\ +\frac{1}{2}E_1(\vec{r},t_1)E_2(\vec{r},t_2)&\exp\left[i((\omega_1 t_1+\omega_2 t_2) - (\vec{k}_1+\vec{k}_2)\cdot\vec{r})\right] + \text{c.c.}\\ +\frac{1}{2}E_1(\vec{r},t_1)E_2^*(\vec{r},t_2)&\exp\left[i((\omega_1 t_1-\omega_2 t_2) - (\vec{k}_1-\vec{k}_2)\cdot\vec{r})\right] + \text{c.c.}\end{aligned} \tag{3.3}$$

While the first three terms are concerned with fields due to only one of $\mathcal{E}_1$ or $\mathcal{E}_2$, the last two terms calculate the fields which are generated from a combination of the fields. In particular the fourth generates a field with frequency $\omega = \omega_1 + \omega_2$. These terms are referred to as the sum-frequency generation (SFG) terms. The last term describes the generation of a field with frequency $\omega = \omega_1 - \omega_2$, and are called the difference-frequency generation (DFG) terms. For the case $\omega_1 = \omega_2$ the DFG term produces a DC field ($\omega = 0$).

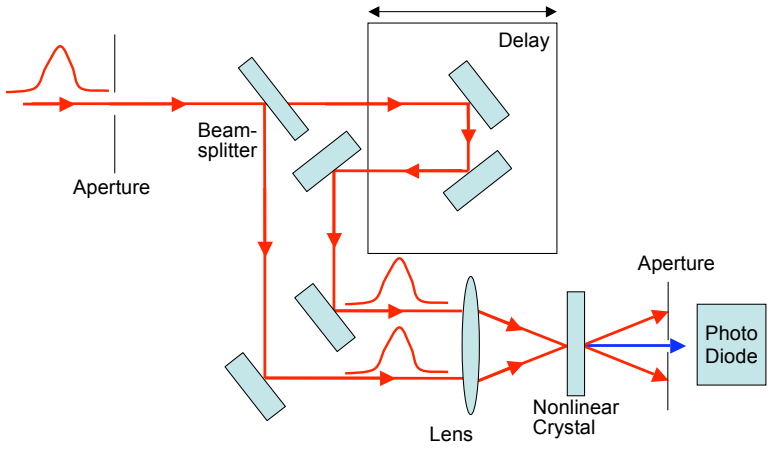

Figure 3.1: The beam from the experiment is first apertured and is split by a beamsplitter. One of the beams can be delayed with respect to the other. The beams are focused on the nonlinear crystal. The second harmonic field generated is measured using a photodiode or photomultiplier.

The autocorrelation experiment is based on the SFG terms, and if the two fields have the same frequency but different $\vec{k}$ vectors, it leads to:

$$\mathcal{P}^{(2)}(2\omega) = \frac{1}{2}E_1(\vec{r})E_2(\vec{r}, t-\tau)\exp\left[i(2\omega t - (\vec{k}_1 + \vec{k}_2)\cdot\vec{r})\right]\exp\left(-i\omega\tau\right) + \text{c.c.} \tag{3.4}$$

When two pulses of the same frequency cross (overlap in space and time) in a suitable nonlinear crystal, this process provides a background-free correlation signal at the doubled frequency of the incoming pulse. In the case of a slowly varying envelope the resulting field $E(2\omega)$ can be found using

$$E(2\omega) = -i\frac{\mu_0\omega^2}{2k}\mathcal{P}^{(2)}L. \tag{3.5}$$

Here L is the thickness of the nonlinear crystal, μ_0 is the magnetic permeability in free space, and k is the wave vector of the field. Therefore SFG provides the nonlinearity required for the autocorrelation experiment. When performing an autocorrelation experiment $t_2 = t_1 - \tau$ with the delay τ. The autocorrelation signal $A^{(2)}(\tau)$ of two identical pulses does not depend

on t but only on the delay between the pulses:

$$A^{(2)}(\tau) = \int_{-\infty}^{\infty} |E(t)|^2 |E(t-\tau)|^2 dt \tag{3.6}$$

Since the complex phase information is lost in the process, the resulting signal does not contain enough information to determine the complex field of the initial pulse. The autocorrelation signal is therefore not unique; *i.e.* different pulse shapes can lead to the same autocorrelation signal. Measuring the pulse length with an autocorrelation experiment requires initial knowledge of the pulse shape. It provides sufficient information if the initial pulse shape is known or if one is only interested in relative changes in pulse length. In order to investigate the differences between pulses due to nonlinear interaction, the phase information is required as well as the amplitude information.

3.1.2 Frequency Resolved Optical Gating as a solution to the uniqueness problem

In order to recover the envelope of the complex field $E(t)$, the amplitude and phase are needed. Autocorrelation measurements do not provide enough information to determine pulse shapes, since the complex phase information is not recoverable; *i.e.* the problem is undersampled since the information available is not sufficient to yield a unique solution. This problem can be solved by the use of frequency resolved optical gating (FROG) [130]. In order to gather the missing phase information, the FROG technique uses the spectrum of the SHG signal as a function of τ. This signal is given by

$$I(\omega, \tau) = \left| \int_{-\infty}^{\infty} E(t) E(t-\tau) e^{-i\omega t} dt \right|^2 \tag{3.7}$$

A measurement of $I(\omega, \tau)$ with appropriate spectral width $\Delta\omega$ and delay $\Delta\tau$ resolution provides sufficient information to recover both the amplitude and phase of the original field. Here the minimal resolution is given by the Nyquist limit, which says the sampling frequency f_{sample} needs to be at least twice that of the highest frequency component measured. From

which the resolution in delay can be found by

$$\Delta\tau = 1/f_{\text{sample}} \tag{3.8}$$

If the FROG trace measured fulfills this criterion, the field retrieved from this data is unique. The remaining question is one of how to retrieve the field from the FROG trace.

3.1.3 The Basic FROG principle

The basic problem in the autocorrelation measurement is the lack of information about the phase of the complex field. This problem can be solved by measuring the spectrum of the second harmonic signal. It is possible to reconstruct the incoming field from the knowledge of the spectrum of the second harmonic signal as a function of delay. The experiment is based on an autocorrelation experiment, as can be seen in Fig. 3.2. The pulse is split by the beam splitter, and one pulse is delayed with respect to the other pulse. Both pulses are then brought to an overlapping focus in the nonlinear crystal. The second harmonic signal is then focused by a second lens into the spectrometer in which its spectrum is recorded by a 1024 pixel CMOS array. The data are transfered to a computer where the data are recorded for later analysis in the form of a FROG trace (Fig. 3.3).

3.1.4 The retrieval process

In order to extract the original pulse shape from the FROG trace (see Fig. 3.3), a modified Gerchberg-Saxton algorithm [129] is employed, as shown in Fig. 3.4. This method was first used on measurements in electron microscopy [158], but was soon after applied to other problems where only intensity measurements are made, but it is necessary to extract both amplitude and phase information [159–172]. The method requires an amplitude measurement in the Fourier space of the object as well as additional information about the object itself. The additional information can be as simple as object size. This information is used to filter the signal in object space and advance the process towards the solution. The algorithm Fourier transforms an initial test function g_{initial} back and forth between the object domain

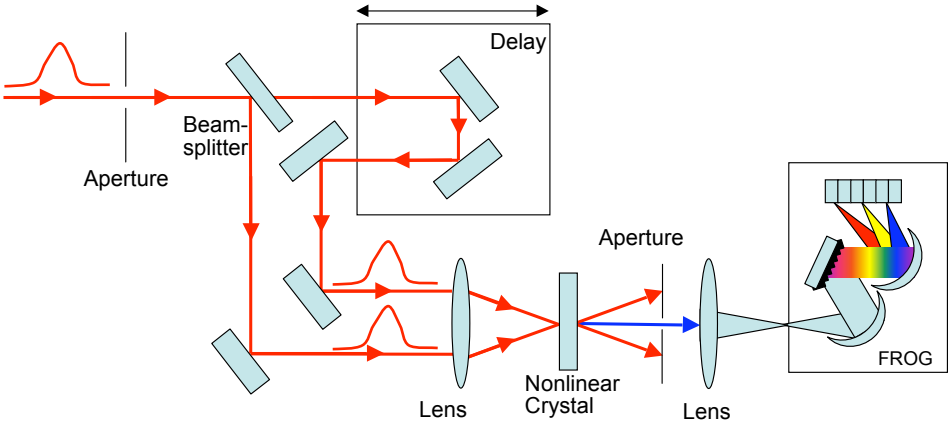

Figure 3.2: The FROG experiment used in this work is shown. It is different from the autocorrelation experiment shown in Fig. 3.1 in that the spectrum second harmonic signal is measured as a function of delay using a spectrometer.

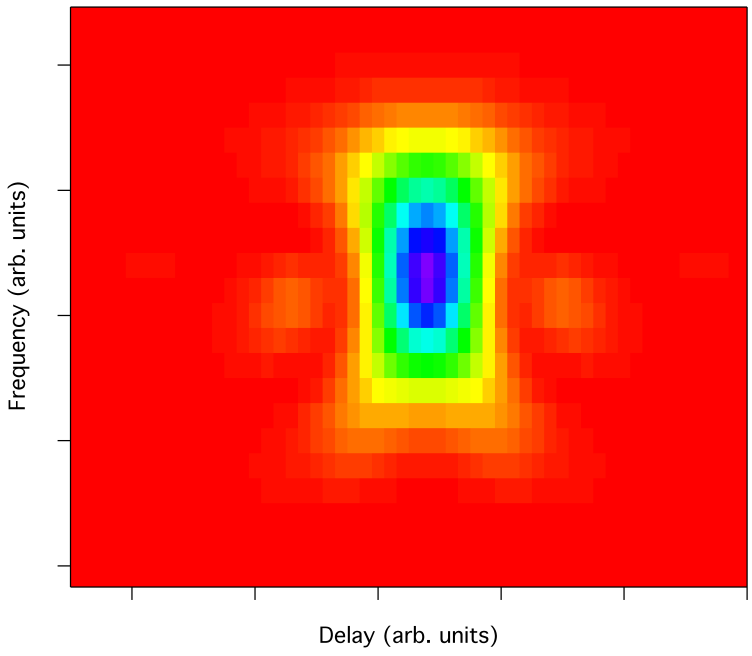

Figure 3.3: The FROG trace of a femtosecond pulse measured with the experiment shown in Fig. 3.2.

and Fourier domain while applying the known constraint and measured data in each domain respectively, improving the function g each time, yielding amplitude and phase information for the unique solution [159].

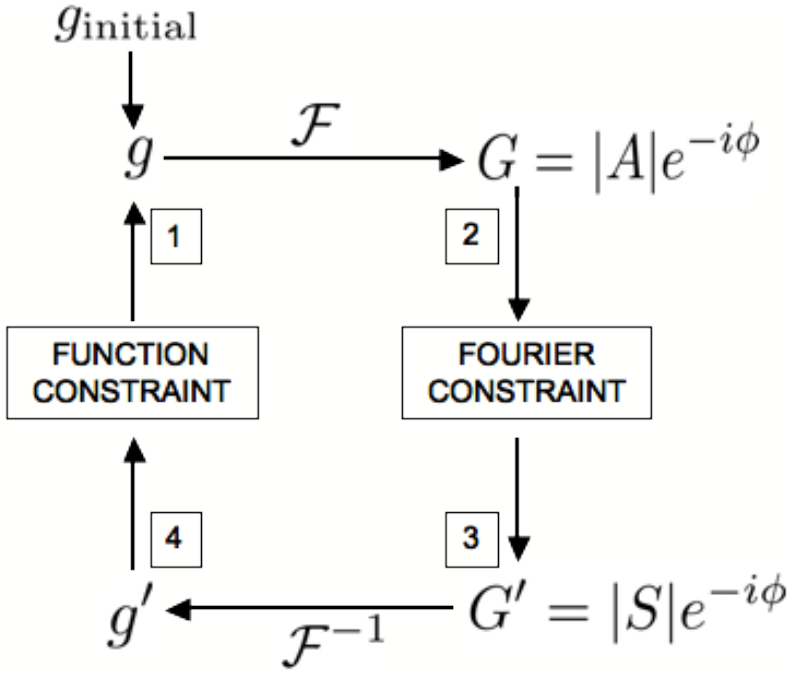

Figure 3.4: The function g is first Fourier transformed into G, which is composed of the amplitude A and phase ϕ. Replacing the amplitude A with the measured amplitude S is the constraint in the Fourier domain giving back G'. This function is inverse-Fourier transformed to g', where the second constraint acts on it giving the improved function g. Starting with an initial guess, g_{initial}, after performing this algorithm multiple times the function g approximates the solution.

To retrieve the solution for the FROG trace, the algorithm needs to be modified to include the nonlinear gating process. The function constraint in the original Gerchberg-Saxton algorithm acts on the function $g'^{(k)}$ itself to produce $g^{(k+1)}$. In the case of the FROG measurement the solution is not the best g but rather the field $E(t)$ that generates the best trace $g(t,\tau)$, where

$$g(t,\tau) = E(t)E(t-\tau) \tag{3.9}$$

In the case of the FROG-retrieval code, an initial guess E_{initial} of the solution is used to construct a signal field $g(t,\tau)$ in the time-delay domain. This trace $g(t,\tau)$ is Fourier transformed

into the frequency-delay domain, giving

$$G(\omega,\tau) = \int g(t,\tau)e^{-i\omega t}dt = |A(\omega,\tau)|e^{-i\phi(\omega,\tau)} \tag{3.10}$$

Here the calculated amplitude $|A(\omega,\tau)|$ is replaced by the measured amplitude $|S_{\mathrm{FROG}}|$ to form the trace $G'(\omega,\tau)$:

$$G'(\omega,\tau) = |S_{\mathrm{FROG}}(\omega,\tau)|e^{-i\phi(\omega,\tau)} \tag{3.11}$$

Where the amplitude S_{FROG} trace is found from the measured intensity I_{FROG} through the relationship $S_{\mathrm{FROG}} = \sqrt{I_{\mathrm{FROG}}}$. $G'(\omega,\tau)$ is now the complex signal field which is inverse Fourier transformed to $g'(t,\tau)$. At this point it is important to understand that the fields in the calculation are represented as a vector that consists of n complex numbers:

$$\vec{E}(t) = \begin{pmatrix} \mathrm{Re}E(t_1) + i\ \mathrm{Im}E(t_1) \\ \mathrm{Re}E(t_2) + i\ \mathrm{Im}E(t_2) \\ \vdots \\ \mathrm{Re}E(t_n) + i\ \mathrm{Im}E(t_n) \end{pmatrix} \tag{3.12}$$

Instead of using the function constraint at this point, the error Z between $g^{(k)}(t,\tau)$ and $g'^{(k)}(t,\tau)$ is calculated:

$$Z^{(k)} = \sum_{i,j=1}^{N} |g'^{(k)}(t_i,\tau_j) - E^{(k)}(t_i)E^{(k)}(t_i-\tau_j)|^2 \tag{3.13}$$

The gradient $\nabla_{E(t)}Z^{(k)}$ with respect to $E^{(k)}(t)$ is found (see Appendix A) and is added to $E^{(k)}(t)$:

$$\vec{E}^{(k+1)}(t) = \vec{E}^{(k)}(t) + x_{\min}\vec{\nabla}_{E(t)}Z^{(k)}(t) \tag{3.14}$$

Where the gradient $\vec{\nabla}_{E(t)}Z^{(k)}$ can be represented as :

$$\vec{\nabla}_{E(t)}Z^{(k)}(t) = \begin{pmatrix} \partial Z^{(k)}/\partial E^{(k)}(t_1) \\ \partial Z^{(k)}/\partial E^{(k)}(t_2) \\ \vdots \\ \partial Z^{(k)}/\partial E^{(k)}(t_n) \end{pmatrix} \tag{3.15}$$

A golden section search optimization process (function *mnbrak* from Numerical Recipes [152]) is used to find the $x_{\min}$ for which the difference between $g^{(k+1)}(t,\tau)$ and $g'^{(k)}(t,\tau)$ is minimal. The loop starts over with the new $g^{(k+1)}(t,\tau)$ minimizing the error between $g^{(k+2)}(t,\tau)$ and $g'^{(k+1)}(t,\tau)$. When the error is no longer changing for additional loops, $E(t)$ is the solution that contains both the complex amplitude and phase of the ultrashort pulse measured.

The gradient $\vec{\nabla}_{E(t)}Z^{(k)(t)}$ usually does not vary greatly from $\vec{\nabla}_{E(t)}Z^{(k+1)}(t)$, which in fact allows the reuse of $\vec{\nabla}_{E(t)}Z^{(k)}(t)$ for a number of loops m in the optimization process before the difference between $\vec{\nabla}_{E(t)}Z^{(k)}(t)$ and $\vec{\nabla}_{E(t)}Z^{k+m}(t)$ becomes significant, and the gradient has to be newly calculated at this point [173]. This allows for faster processing, since the calculation of the gradient is computationally expensive.

Progress of the algorithm is measured according to the difference between the measured amplitude trace in the frequency-delay domain and the amplitude trace of the generated trace $G(\omega,\tau)$:

$$G_{\text{error}}^{(k)} = \sqrt{\frac{1}{N^2}\sum_{i,j=1}^{N} |I_{\text{FROG}}(\omega_i,\tau_j) - (G^{(k)}(\omega_i,\tau_j)[G^{(k)}(\omega_i,\tau_j)]^*)|^2} \tag{3.16}$$

$I_{\text{FROG}}(\omega_i,\tau_j)$ is the measured intensity at ω_i and τ_j, and $G^{(k)}(\omega_i,\tau_j)[G^{(k)}(\omega_i,\tau_j)]^*$ gives the intensity of the FROG trace generated by the phase retrieval code.

Ambiguities in SHG-FROG measurements

There are several ambiguities inherent in SHG-FROG that still need to be addressed. Even thought the SHG-FROG measurement over-samples the complex electric field envelope, the technique actually yields two solutions: The field and its complex conjugate, as can be seen by rewriting Eq. 3.7:

$$I(\omega,\tau) = \int_{-\infty}^{\infty} E(t)E(t-\tau)e^{-i\omega t}dt \int_{-\infty}^{\infty} E^*(t')E^*(t'-\tau)e^{i\omega t'}dt' \tag{3.17}$$

Inserting the complex conjugate of the complex field E does not change the resulting FROG trace. Therefore the retrieval code cannot distinguish between the retrieved field and its

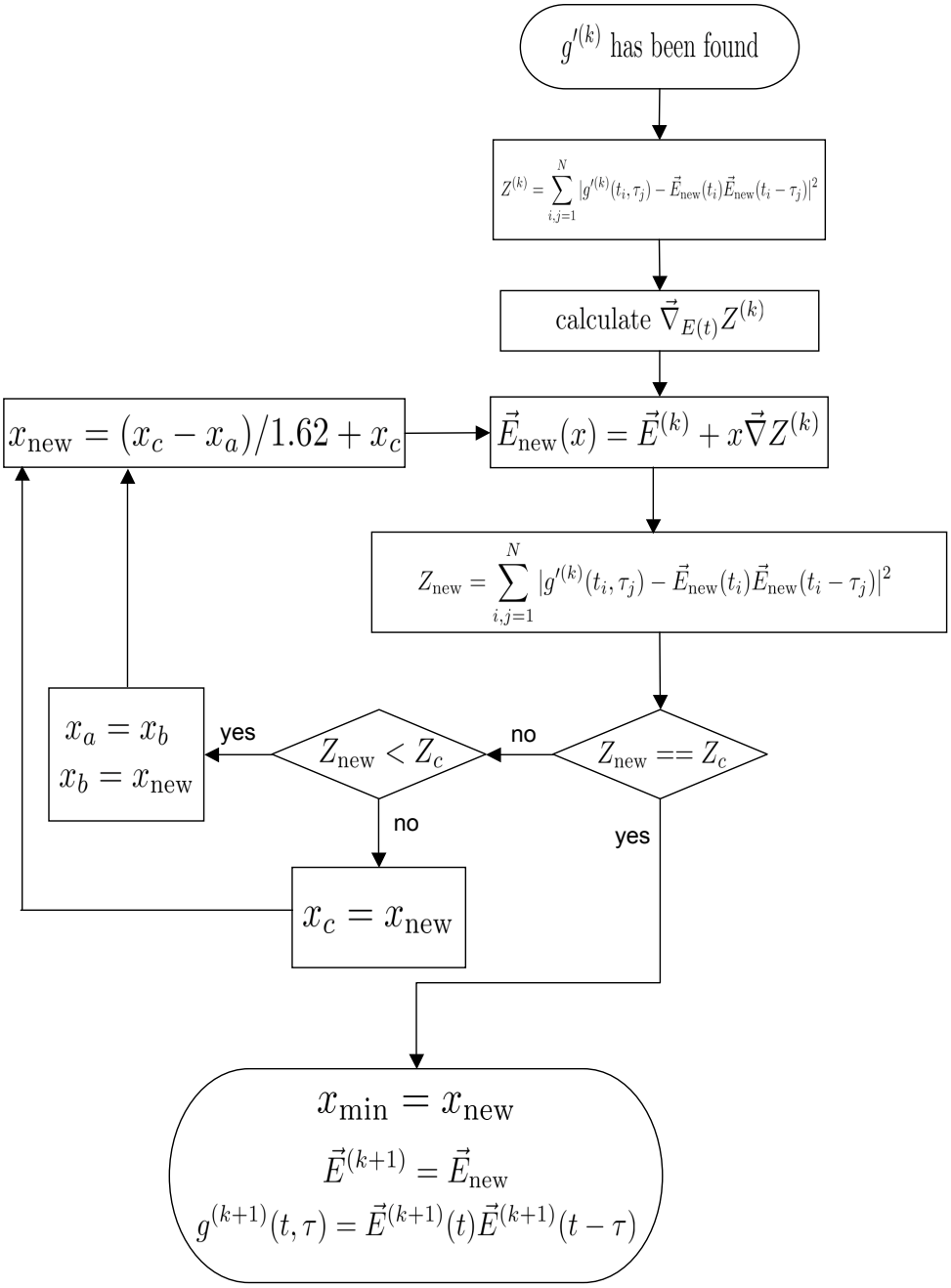

Figure 3.5: For the FROG retrieval algorithm, the function constraint step from Fig. 3.4 is changed into an optimization loop, which is used to find $x_{\rm min}$, for which the error Z is minimized. A new $g(t, \tau)$ is generated using the field $E_{\rm new}$ found using $x_{\rm min}$.

complex conjugate, which is time reversed. This ambiguity can be resolved by taking into account additional information, such as a known pre- or post-pulse, or a known or artificially introduced chirp.

Other ambiguities are the missing absolute phase and center frequency from the SHG-FROG solution, which can be found by integrating the measured FROG trace over all τ. While the absolute phase does not effect the data presented in this dissertation, it can present a problem when using pulses shorter than one optical cycle. Since the absolute phase determines where the electromagnetic field has its maxima with respect to the envelope function, in cases where the envelope is short enough, it can lead, for example, to an unequal distribution of energy in an otherwise symmetric pulse envelope.

3.2 Experimental Setup

The experiments described in this dissertation were performed in two different laboratories. The experiment was designed, tested and used for experiments first in the laboratory at the Department of Physics and Astronomy at the University of Georgia between the years 2004 and 2008. The experiment was transfered in the Summer of 2008 to Saint Étienne in France to the laboratory of Dr. Stoian at the Laboratoire Hubert Curien of the Université Jean Monnet. The experiment at UGA is shown in Fig. 3.6 and is described below.

3.2.1 Laser Systems

The laser system in Dr. Dennis' laboratory comprises a Spectra-Physics Tsunami oscillator and a Clark MXR CPU amplifier system. The oscillator is pumped by a continuous wave diode pumped Nd:YVO_4 laser system (Spectra-Physics, Millennia) which produces 5 W at $\lambda_0 = 532$ nm. The Ti:Sapphire Tsunami laser produces 130 fs FWHM pulses with a center frequency of 800 nm ($\pm$ 5 nm) and a spectral FWHM of 11 nm ($\pm$ 1 nm) with a repetition rate of 83 MHz and an average power of 0.5 W.

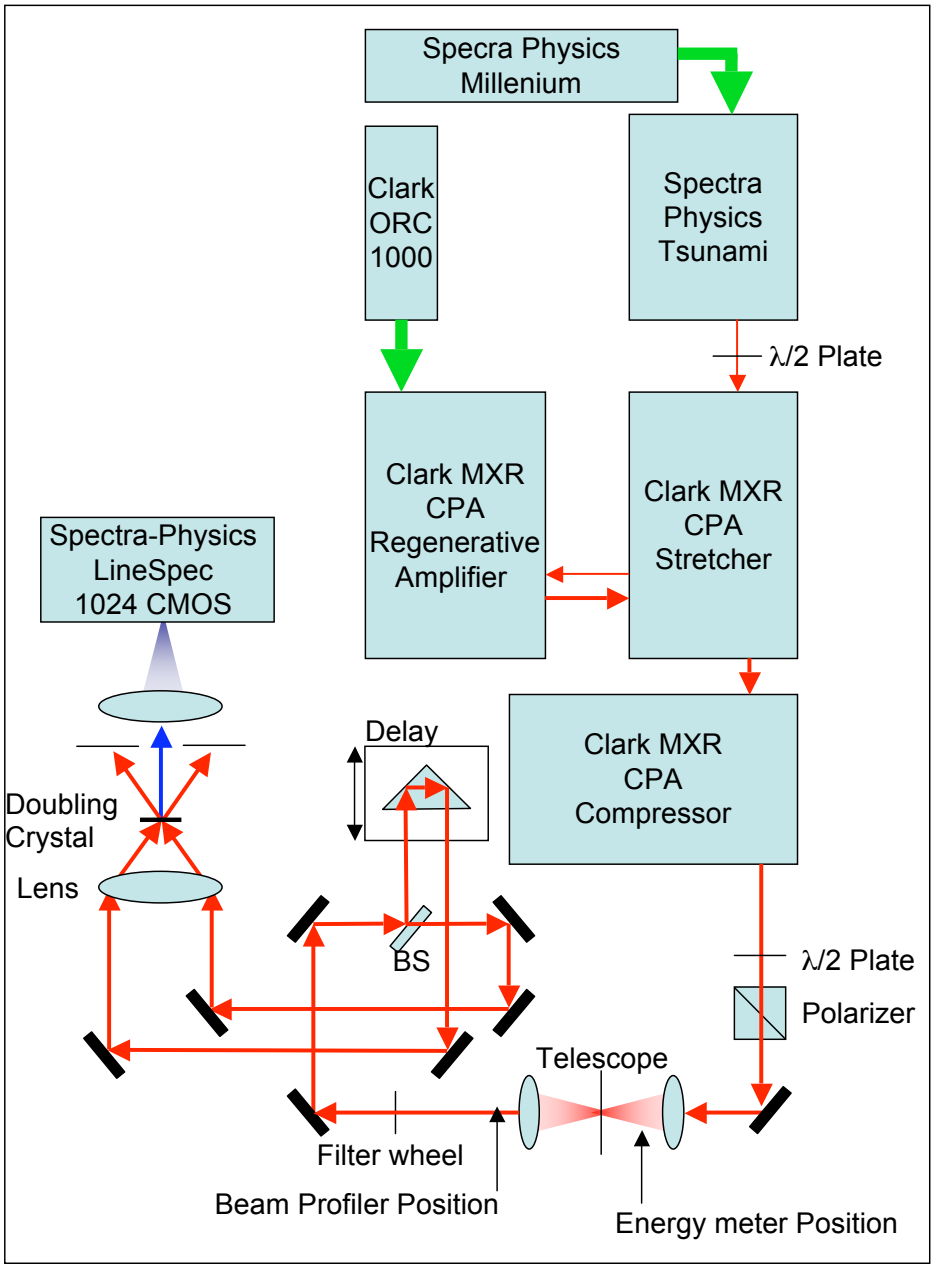

Figure 3.6: The complete experiment as used at UGA.

The oscillator pulse polarization and beam height are first changed to match the requirements of the amplifier system. The femtosecond pulses are amplified using a Clark MXR CPU regenerative amplifier system which contains three units (stretcher, amplifier, compressor) and one pump laser (a Clark MXR ORC 1000). The oscillator pulse, which has a spectral FWHM of $\Delta\lambda = 11$ nm centered around $\lambda_0 = 800$ nm, is stretched using a grating to impose a path length difference on the spectrum. The spectral components of the oscillator pulse are reflected off the grating at an angle which is a function of the wavelength. The beam path in the stretcher is now also a function of the wavelength, delaying the shorter wavelength components with respect to the longer wavelength components (positive chirp). It is necessary to stretch the pulse from around $\sim$100 fs to $\sim$ 200 ps in order to reduce the peak-intensity and thus to not damage the amplifier.

A Pockels cell - polarizer combination functions as a gate into the regenerative amplifier. The pulse is amplified by multiple passes through the Ti:Sapphire crystal which is pumped by the Clark MXR ORC 1000 mode -locked 10 ns Nd:YAG system with 1 kHz repetition rate and 10 W output at $\lambda_0 = 532$ nm. Upon reaching maximum amplification inside the amplifier, the Pockels cell is gated to switch the pulse polarization from horizontal to vertical (see Fig. 3.7). The pulse is redirected out of the amplifier by transmission through the polarizer. The pulse then enters the compressor unit and is recompressed. The system produced 0.3 W average power at a 1 kHz repetition rate. The amplified pulses were characterized to a pulse width of 140 - 150 fs FWHM and a center wavelength of 800 nm. Most of the results presented in this dissertation were taken using this system.

The Laser system at the Laboratoire Hubert Curien of the Université Jean Monnet in Saint Étienne was composed of a Ti:Sapphire oscillator (Coherent Inc.: Vitesse), which produces 100 fs FWHM pulses with a central wavelength of 800 nm. These pulses were amplified to 1.5 mJ/pulse using a Ti:Sapphire regenerative amplifier system (Thales Laser: Concerto) [174]. The pulses were shaped using a Jenoptic liquid crystal shaper (640 pixel) before entering the amplifier system.

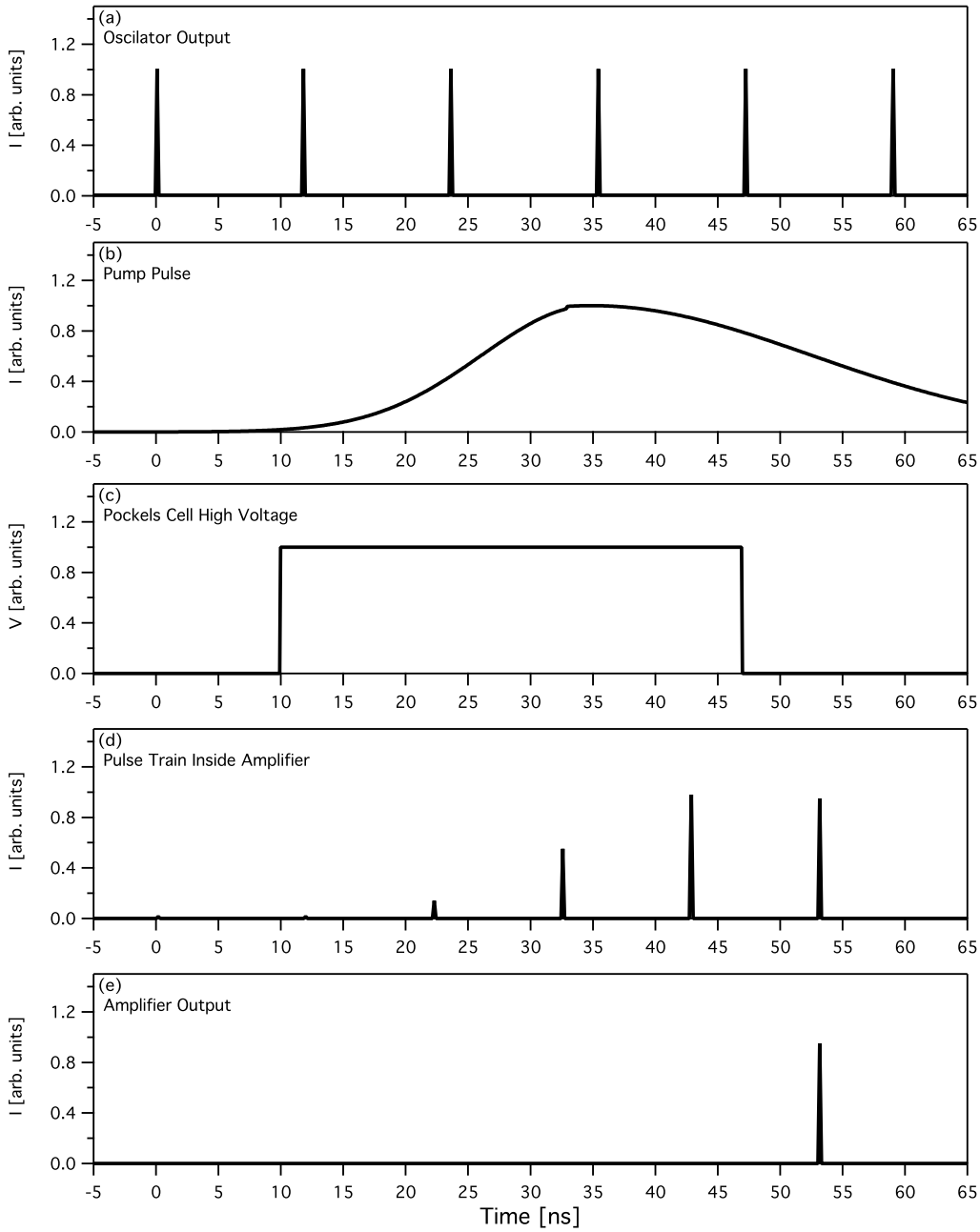

Figure 3.7: Amplifier timing diagram: (a) shows the oscillator output. The pulse at time $t = 0$ ns triggers the event sequence: (b) shows the triggered pump pulse. The high voltage gate is shown in (c), where the power supply sends a high voltage gate to the Pockels cell at $t = 10$ ns, which allows the oscillator output (a) to enter the amplifier at $t = 12$ ns. In the amplifier (shown in (d)), the pulse is amplified over multiple passes inside the amplifier and peaks shortly ($t = 42$ ns) after the peak of the pump pulse ($t = 35$ ns). The high voltage is turned off at this point allowing the amplified pulse to leave the amplifier which is shown in (e).

3.2.2 Telescope, Sample and Sample Holder

After the beam exits the compressor it is apertured by a pinhole to increase the quality of the beam profile (not shown in Fig. 3.6), after which it passes through an attenuator (composed of a $\lambda/2$ plate and a polarizer) in order to adjust the pulse power at the sample. The telescope is constructed from two 25 cm focal length quartz lenses with the sample surface at the focus of the first lens. The beam energy is measured behind the first lens and in front of the sample by a removable energy meter as indicated in Fig. 3.6. Measurements of the beam profile were performed after the second lens using a Newport LBP-2 USB beam profiler.

The sample holder was custom built from aluminum and teflon and was designed to fit into a standard 2" optical mount. The sample surface was positioned at the focus of the first lens of the telescope. The optical mount enables the adjustment of the sample's orientation in order to ensure that the beam is at normal incidence. 250 μm thick BK7 microscope cover slips were used for initial alignment and testing of the experiment. The experiments described in this dissertation were performed using 200 μm thick fused silica samples (a-Si_2O). The samples were polished on both sides. The experiments were conducted in air at room temperature.

3.2.3 FROG experiment

After transmission trough the sample, the laser pulse is recollimated and its energy reduced using a filter wheel.

The pulse is next split into reference and sample pulses by a thin film 50/50 beam splitter (BS in Fig. 3.6). The reference beam is redirected by mirrors to a lens which focuses it into the 0.6 mm thick nonlinear BBO crystal (Newlight Photonics). The sample pulse is then directed to a retroreflector located on an automatic translation stage (Newport UTM100PP.1 Motion Stage controlled by a Newport Universal Motion Controller Model ESP300) which serves as an adjustable delay. The sample pulse arrives at the lens, focusing it onto the BBO

crystal delayed by τ with respect to the reference pulse. The two pulses are in spatial overlap inside the crystal. The nonlinear correlation signal from the BBO crystal is apertured at this point by an adjustable pinhole and focused by an additional lens on the entrance slit of the Spectra-Physics LineSpec 1024 CMOS spectrometer. The resulting data are transmitted using a USB connection to a computer that records the spectrum and adjusts the delay for the next measurement.

Control Software

Since the FROG experiment was constructed using preexisting components, the software controlling the data acquisition was developed in-house. A Pentium III based PC running Windows 95 was used to control the spectrometer over the USB port and the motion controller was controlled over the ethernet IEEE 488 port (GPIB). The program was written in Microsoft Visual C++.NET version 2003. The program allows the user to set experimental parameters such as delay range, step size, exposure time of the CMOS array, and both on-chip and computer averaging. It also allows the user to take multiple sequential measurements with different integration times. The data and the parameters for which the trace is taken are saved in files with a predetermined name and an index number.

Problems with the FROG experiment used and their solutions

The dynamic range of the detector is crucial when measuring SHG-FROG traces. In order to collect complete data, which allows the retrieval of the correct complex field, low intensity signal components must be measured. Trebino *et al.* defines the minimum criterion for a sufficient data range of a FROG trace when "the intensity of the data points at the perimeter of the FROG trace grid are 10^{-4} or less of the peak of the trace" [170]. This is the minimal requirement to retrieve the general pulse shape. In order to retrieve low intensity parts of the field (*e.g* pre-pulses, details in the pulse tail), a higher dynamic range is often desirable. In general detectors have a limited dynamic range resulting from both a detection threshold

for low intensity signals and saturation effects at high intensity signals. The detector in the FROG experiment used for this dissertation is a Spectra-Physics LineSpec 1024 CMOS spectrometer and has a dynamic range of 2.9×10^3. The problem caused by the low dynamic range of this detector was solved by the multi-FROG technique that was developed as part of the dissertation.

While the dynamic range is defined by the ratio of the highest measurable signal to the lowest detectable signal, depending on the exposure time, different intensity regimes can be measured. The lowest detectable signal is a signal that is above the noise floor. This fact enables one to overcome the inherent dynamic range limitation of the spectrometer, by using different exposure times to measure the full range of the signal.

This method can be used not only for CMOS devices, but all detectors with adjustable detection sensitivity and limited dynamic range, and enables the acquisition of high dynamic range data with inexpensive components.

Note that the background caused by the detection threshold and dark current can be subtracted from the signal. The new ratio of maximum to minimum signal (distinguishable from the noise floor) is denoted the corrected contrast ratio (see Fig. 3.8).

MULTI-FROG

To date there have been two approaches to producing High Dynamic Range (HDR-) FROG traces. Billet and co-workers [171; 172] use a hardware based approach, *i.e.* they use a high dynamic range spectrum analyzer to measure the FROG trace with correspondingly high dynamic range. A second software based approach was used by Wang *et al.* [175] to generate a HDR-FROG trace in order to investigate the energy stored in the wings of a 24 fs amplified laser pulse. These authors used two SHG-FROG traces measured with different exposure times and merged them to produce a single trace with a higher dynamic range. The final result of both of these techniques is the generation of a FROG trace with the necessary

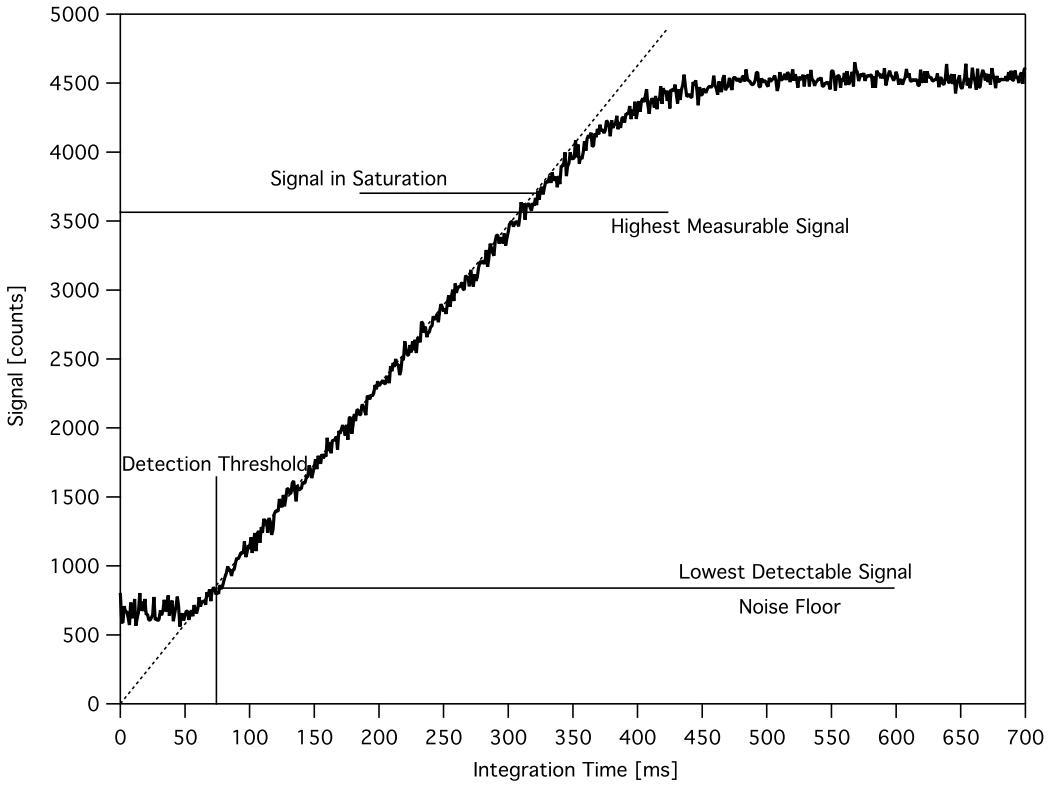

Figure 3.8: The response curve of a generic detector, which has for a given signal a minimum integration time of 75 ms. At this point the signal is above the noise floor and detectable. For integration times higher than 310 ms the detector begins to go into saturation and and is no longer linear.

dynamic range to retrieve details in the low amplitude range of the complex electric field *i.e.* an HDR-FROG trace.

To our knowledge, the work of Wang *et at.* is the only prior software based technique that has been used in the context of FROG to generate higher dynamic range traces. Their technique did not account for a detection threshold and the resulting offset so that the individual traces may not fit together perfectly, adding additional noise to the final trace [175]. The actual integration times used by Wang *et al.*, and the integration time ratios, were not reported by Wang *et al.* [175]. However, it is clear that the peak of the FROG trace was not in saturation for the shorter integration time and was in saturation for the longer integration time. The integration time ratio can be used to optimize the dynamic range and is therefore a critical parameter to which close attention must be paid when setting up the experiment. In Wang *et al.* [175] the merging of the two traces was performed manually, which is a time consuming process; their technique did not include any averaging in the region where both traces overlap.

In the current work, the approach of Wang and co-workers is extended, a technique has been developed whereby an optimum number of FROG traces are acquired at appropriate integration times and are merged to construct a high fidelity HDR-FROG trace. Throughout this dissertation, this technique is referred to as multi-FROG and abbreviated m-FROG. The result of this technique, *i.e.* a high dynamic range FROG trace, is still referred to as HDR-FROG.

While m-FROG was developed using second harmonic generation (SHG) FROG, the technique described in this dissertation is general and can be applied to other FROG measurement schemes. Note that m-FROG is based upon a well-established technique in photography [176; 177] that uses sets of two or more pictures taken with different exposure times to generate one picture with higher dynamic range. We will demonstrate that it is possible to leverage this technique to generate one HDR-SHG-FROG trace from multiple SHG-FROG

traces taken with different exposure times and successfully retrieve the complex field from the data.

Since the main problem addressed in the following is the limited dynamic range of the Spectra-Physics LineSpec 1024 CMOS spectrometer, it is useful to examine its response function and discuss its implications on the data acquired. Fig. 3.9a shows the detector response for different integration times and energies of a single pixel of the spectrometer. The response function $S(W,T)$, with W being pulse energy and T the integration time, is linear between 643 counts above the noise floor and the onset of saturation at 4143 counts; only data from this linear region will be used. Fitting the linear part of the response curve was performed using:

$$S_{\text{linear}}(W,T) = a + bWT \tag{3.18}$$

The offset a and slope b are found using the known exposure time for each trace. Note that a as well as b are independent of pulse power and integration time. When scaling the signal, one might find it desirable to scale to a virtual final integration time T_f. This can be useful when trying to compare to data measured at different integration times or to improve preexisting data with additional data. In this dissertation the longest integration time was used for T_f. In order to merge a series of FROG traces into a HDR-FROG trace, the response function for the HDR-FROG trace $S^*(W,T_f)$ must be used:

$$S^*(W,T_f) = a + \sum_{\text{i}} T_f \left(\frac{S_i(W,T_i) - a}{T_i} \right), \tag{3.19}$$

where T_i are the integration times of the measured traces with response function $S_i(W,T_i)$. When all of the data has been scaled using Eq. 3.19 the response function is shown in Fig. 3.9, of which only the linear part is used for generating the HDR-FROG.

The quality of the recovered complex field is generally measured in the form of the FROG error G_{error} defined as:

$$G_{\text{error}} = \sqrt{\frac{1}{N^2} \sum_{\text{i,j=1}}^{N} |I_{\text{FROG}}(\omega_i,\tau_j) - I_{\text{retrieval}}(\omega_i,\tau_j)|^2} \tag{3.20}$$

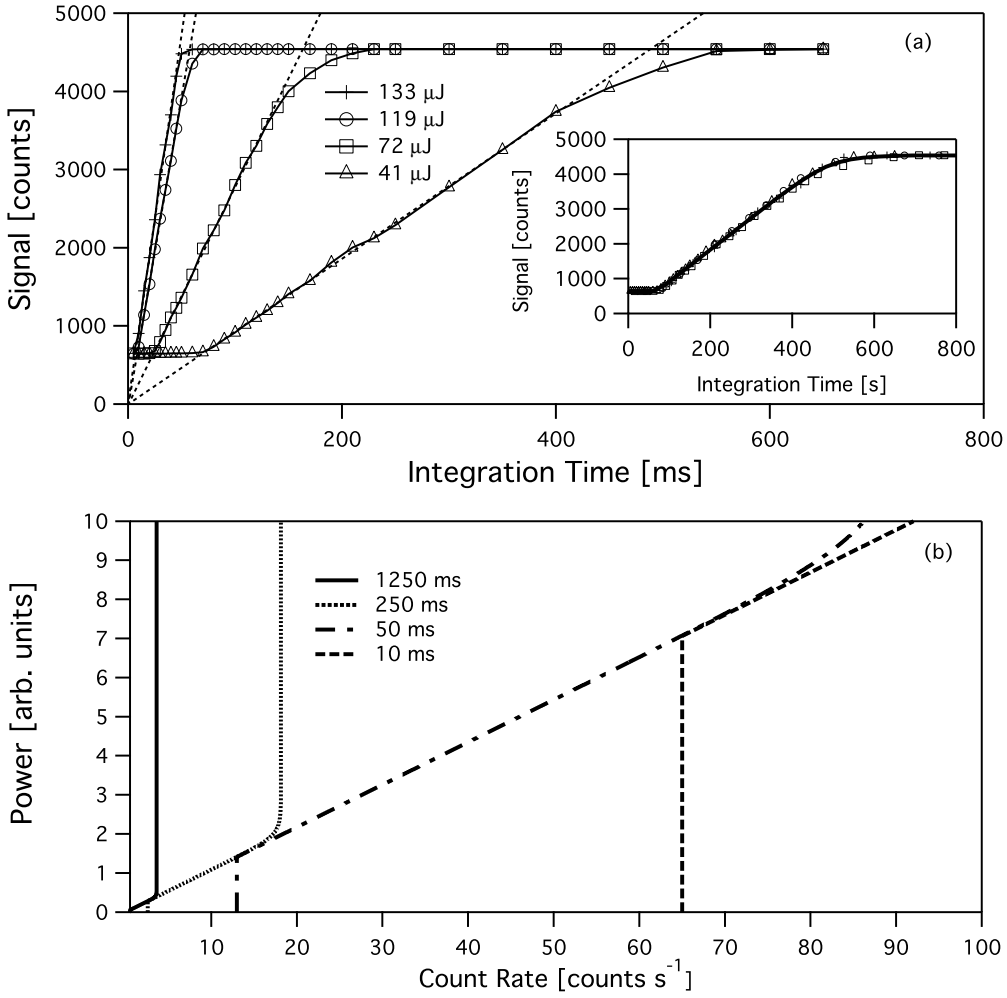

Figure 3.9: (a) Shows the measured counts as a function of integration time for four different pulse energies. The linear fit shows that the offset is pulse energy independent. The inset shows that the response curves for different energies are in fact self-similar and can be fitted by a single saturation function. (b) The response functions (power versus counts per second) measured with different integration times show that the linear region spans over a certain range of incident powers, and the dynamic range can be improved by merging data measured at different integration times. Note that even very low powers can be measured by using sufficiently long integration times.

with $I_{\mathrm{FROG}}(\omega_i, \tau_j)$ being the measured intensity at point ω_i, τ_j and $I_{\mathrm{retrieval}}$ the intensity of the FROG trace generated by the phase retrieval code using the best complex field (for a more detailed discussion see [170]).

In some cases the complex field can be retrieved from HDR traces that were generated without accounting for the offset a when merging the traces. HDR traces that do account for offsets are smoother, have a better dynamic range, are more reliable, and produce a lower G_{error} when used in the retrieval process. However, in general this neglect can cause the retrieval code to fail and result in falsely retrieved fields. The combination of using more than two traces and accounting for the offset in the merging procedure enables a lower noise higher contrast ratio HDR FROG traces to be generated. The best corrected contrast ratio possible, C_{best}, can be estimated as the product of the corrected contrast ratio of a single trace, C_{single}, and the ratio of the longest (T_l) to shortest (T_s) available exposure time:

$$C_{\mathrm{best}} = C_{\mathrm{single}} \frac{T_l}{T_s} \tag{3.21}$$

The choice of the exposure times is clearly very important if there are to be no gaps in the intensity coverage (Fig. 3.9.b). This would be the case when the exposure time ratios were too large, for example when the signal at a point in one trace goes into saturation before the signal at the same point in the next trace becomes detectable. For the regions in which two or more traces provide data, the signals are averaged after being scaled. Note that it is crucial that the FROG traces perfectly overlap in space and frequency domains.

By accounting for the background noise before merging, the process produces a smooth and complete HDR-FROG trace. The corrected contrast ratio is calculated by dividing the peak value of the final trace with the smallest detectable signal (with offset subtracted). To test m-FROG, both experimentally measured and computer generated FROG traces were used. Since the FROG experiment is based on an autocorrelation experiment, the SHG-FROG experiment includes a motorized delay stage, which is used to change the delay between the two beams and is synchronized with the spectral measurements. Acquisition of the individual FROG traces was performed using a Spectra-Physics LineSpec 1024 CMOS

spectrometer. This spectrometer uses a 1024 pixel CMOS array with integrated circuitry that enables the integration time to be set between 1 ms and 4000 ms and also provides an on-chip average function.

This device has a background of 567 ± 10 counts and is completely saturated at 4538 counts, and 7.1 dB is the upper limit of the dynamic range. Note that as delivered, the response curve of this device is biased so that the range 643–4538 counts is within the 0–4095 counter range.

For the experimental validation of this section, multiple SHG-FROG traces were recorded using the equipment described. The integration times for pulse energy of 10 μJ were chosen to be 1900 ms, 850 ms, 475 ms, 237 ms, 118 ms, 59 ms, 29 ms, 14 ms, 7 ms. The integration times were chosen so that all data between the lowest signal of the longest integration time and the strongest signal of the shortest integration time fell in the linear region of at least one trace.

The issue of noise from the sensor still has to be addressed. Since it is not possible to synchronize the start of the time window and the arrival of the laser pulses, the number of pulses detected may vary by $\pm$ 1, adding noise to a single exposure when the exposure time is short; this is an addition to the noise of pulse to pulse variation. In order to reduce effects from both kinds of noise, data is collected multiple times with the same integration time and then averaged.

In each trace there are regions for which the signal was lower than the detection threshold, regions where the signal is in the linear region of the detector, and regions for which the detector was in saturation. In order to merge the traces into a single trace, the linear signal regions are identified for all traces. For the sensor used in this dissertation the linear region extends from 643 to 4538 counts. The background (643 counts) is subtracted from the signal. Figures 3.10 (a) - (i) show the regions with usable signals of the individual traces. The regions with signal outside of the linear regions are black, while the signals inside the linear region

are shown in grayscale. It can be seen that the traces, when laid on top of each other, have overlapping linear regions where the signal is scaled and averaged.

These traces were used to construct a HDR-SHG-FROG (Fig. 3.10.j), following the procedure described above. In preparation for the phase retrieval code the HDR-FROG is converted from wavelength spacing to frequency spacing. This procedure included modifying the delay step size as described below [170]. This step is necessary because the trace is later Fourier transformed from the frequency delay domain into the time delay domain. In order to simplify the process it is desirable to have the same time and delay spacing. Since the time spacing δt is given by $\delta t = 1/\Delta\omega$, with $\Delta\omega$ being the frequency range of the FROG trace, it is necessary to change the delay spacing when changing the frequency range. Additionally it can be necessary to zero pad the trace either in frequency or time in order to ensure a sufficient sampling rate in the other domain. Finally, the prepared HDR-FROG trace was analyzed by the phase retrieval code [170].

Fig. 3.11 shows retrievals from three data sets with each a different dynamic range. The trace in Fig. 3.11.a was constructed using the FROG traces acquired with integration times 7 ms - 59 ms shown in Fig. 3.10 which resulted in a corrected contrast ratio of 32019. The trace with the next best corrected contrast ratio of 65007 is shown in Fig. 3.11.c, which was constructed using the FROG traces with integration times 7 ms - 118 ms. When using all available traces from Fig. 3.10, a corrected contrast ratio of 1.124×10^6 was achieved.

It is evident that the complex field shown in Fig. 3.11b retrieved from the trace with corrected contrast ratio of 32019 (Fig. 3.11.a) shows an essentially symmetric amplitude and an essentially cubic phase. The retrieval was performed at a trace size of 128 $\times$ 64 pixels and had a final G_{error} of 0.0129.

At a corrected contrast ratio of 65007, the phase is still essentially cubic but the amplitude shows a strong asymmetry in the pulse wings (Fig. 3.11.d). With the same trace dimensions as before, this retrieval has a final G_{error} of 0.0114. The complex field retrieved from a trace with a corrected contrast ratio of 1.124×10^6 has its main features unchanged but has

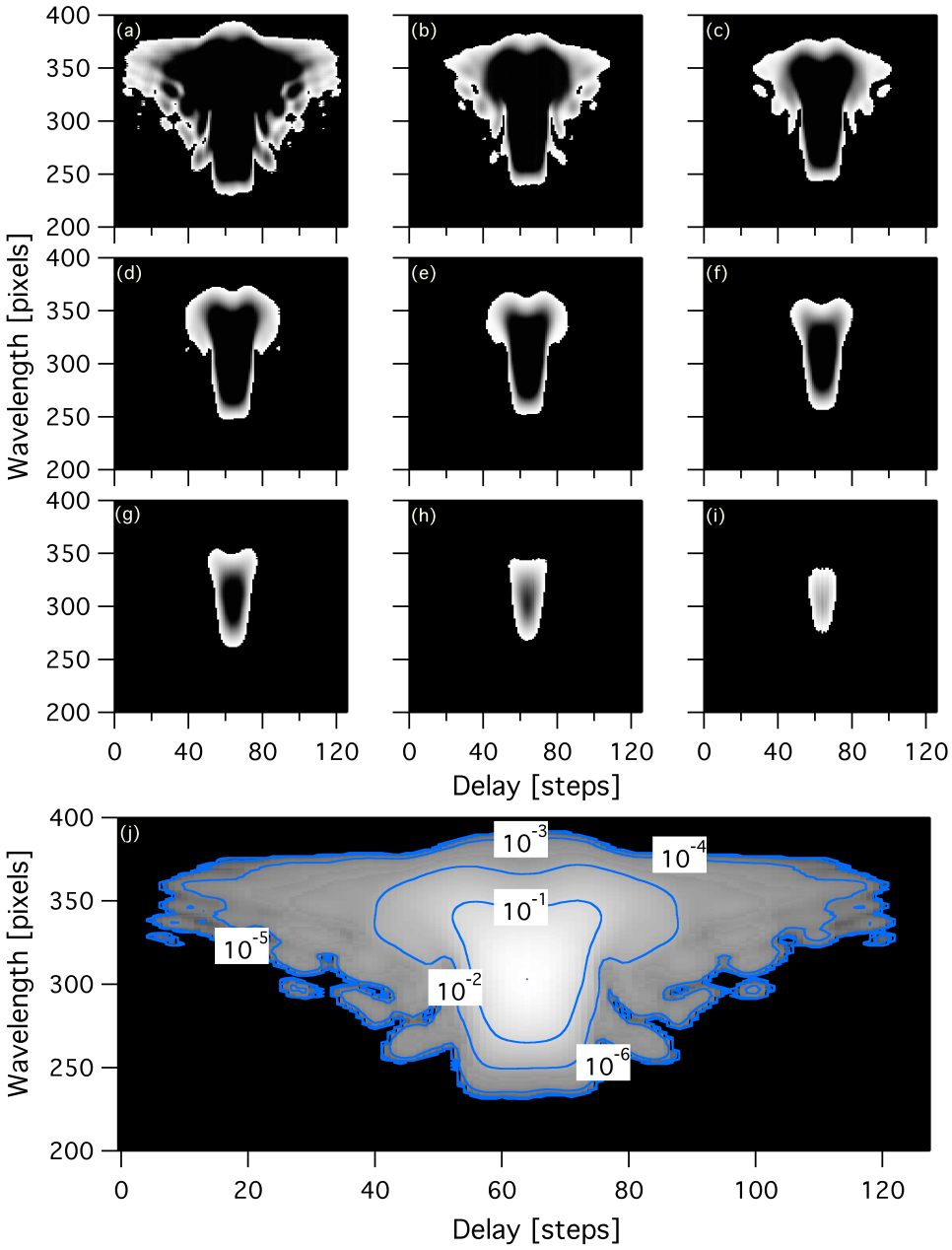

Figure 3.10: (a) - (i) show the usable signals of the SHG-FROG traces using a linear grayscale. The integration times are (a) 1900 ms, (b) 950 ms, (c) 475 ms, (d) 237 ms, (e) 118 ms, (f) 59 ms, (g) 29 ms, (h) 14 ms, (i) 7 ms. (j) shows the full HDR-SHG FROG trace using a logarithmic grayscale.

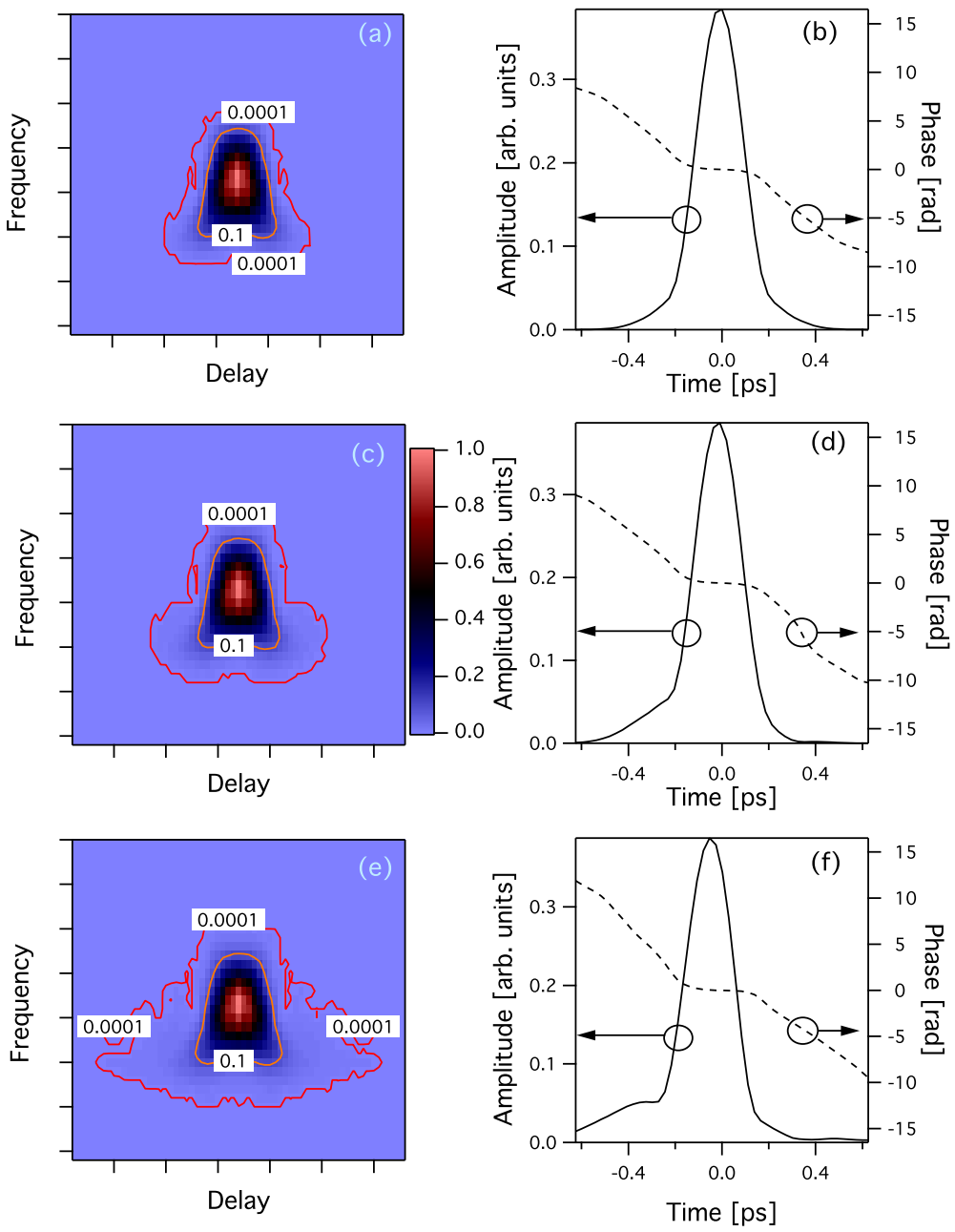

Figure 3.11: The trace shown in (a) has a corrected contrast ratio of 32019 and when used in the phase retrieval process leads to the complex field shown in (b). The trace shown in (c) has a corrected contrast ratio of 65007 and when retrieved has the complex field shown in (d) as its solution. The trace with the highest dynamic range is shown in (e) which has a corrected contrast ratio of 1.124×10^6 and leads to the complex field shown in (f) when retrieved.

more details at lower amplitudes (Fig. 3.11.f). The G_{error} for the retrieval from this HDR-FROG trace is 0.01127. To support the experimental results a computer generated complex field was used to generate one HDR-SHG-FROG trace (512 × 256 pixel) with a corrected contrast ratio of 10^{31}. The data in this HDR-FROG trace was used to generate 11 traces with limited dynamic range, corresponding to traces found from 11 measurements with different integration times. The data was scaled for all of the 11 traces according to the specific integration time of the single trace and an offset was added to simulate experimental data. The 11 limited dynamic range traces each contain data comparable to that which would have been gathered in an experiment with a given integration time. The integration times for this process were doubled between traces, starting with 1 ms, corresponding to the experiments presented. A HDR-FROG trace was then reconstructed using both the methods of Wang *et al.* [175] and of m-FROG. The method described in Ref. [175] leads to a HDR-FROG trace with a corrected contrast ratio of 2.5×10^6, while the trace constructed using m-FROG had a corrected contrast ratio of 3.1×10^6. Two examples are shown in Fig. 3.12. The first case (Fig. 3.12. and 3.12.b) is a rather simple pulse (inspired by the self- phase modulated pulse shown on page 118 in [170]). The phase retrieval code converged for the traces prepared with the method of Ref. [175] and m-FROG with a G_{error} of 0.0044 and 0.001, respectively. While both retrieved fields show good agreement with the features of the original field for the central part of the pulse, the field coming from the trace prepared using the technique of Ref. [175] is shorter and the phase shows strong variation closer to the pulse peak than the phase retrieved from the m-FROG trace. These differences become more significant for the second case, which was chosen for its detail rich structure. Pulse shaping technology enables the production of such pulses, and therefore recovering these details is important. For this example the code converged for both traces with a G_{error} of 0.0061 and 0.0017, respectively. While the field retrieved from the m-FROG trace agrees very well over most of the field in amplitude and phase, the field from the traces prepared using the technique of Ref. [175]

shows only approximate similarity to the original field amplitude. This demonstrates that for those cases the G_{error} is a reliable measure of the performance of the pulse retrieval process.

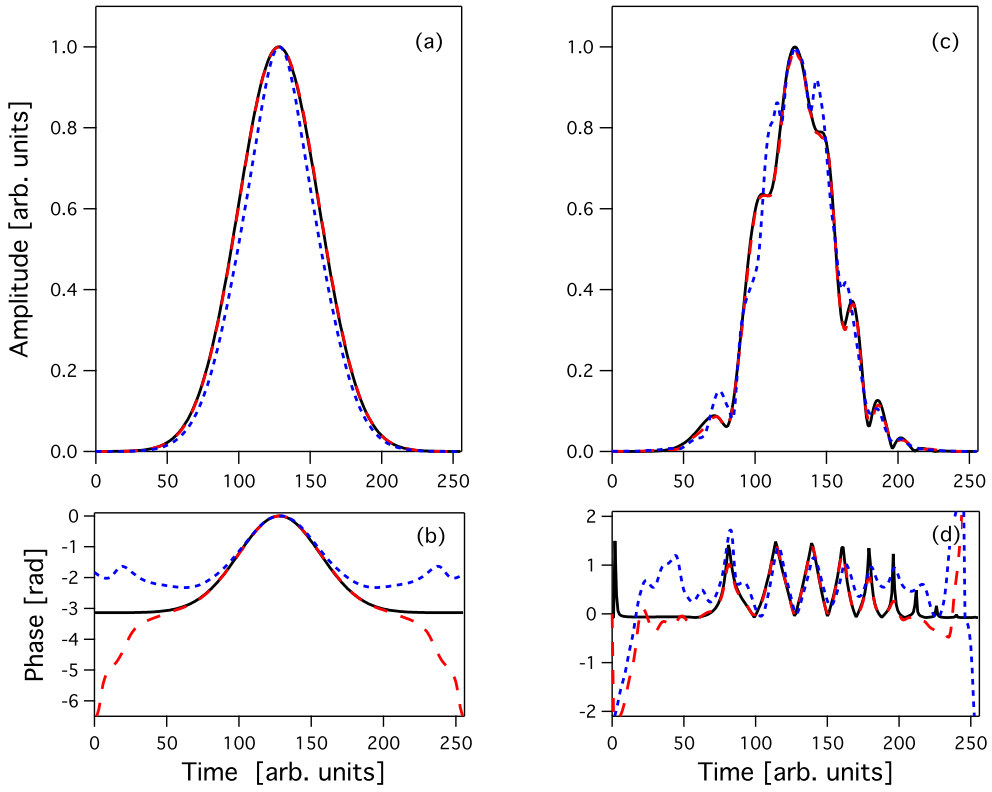

Figure 3.12: The original field (solid black line) in comparison with retrieved fields from traces prepared using the technique of [175] (dotted blue line) and m-FROG method (dashed red line) for two cases. A simple case with amplitude (a) and phase (b). A case with more detail rich structure with amplitude (c) and phase (d).

Despite the impressive performance of the m-FROG technique demonstrated above, there are still some problems to address. The noise in the short exposure time traces is amplified when the signal is scaled. Due to the use of multiple scans, a complete set can take up to one and a half hour, which leads to stringent requirements on the stability of both the laser and the experiment. There is a trade-off between the constant exposure time ratio between scans and the varying signal resolution of the final HDR trace. Since all traces a scaled to a final integration time, the noise is scaled accordingly as well, which means the noise level in the final traces is amplitude dependent [178].

3.3 FROG analysis Software

All software for data analysis and phase retrieval was written in C++ by the author of this dissertation. The data that was collected using the m-FROG technique needed to be preprocessed in order to fulfill the requirements of the phase retrieval process. In order to speed up the discrete Fourier Transformation in the retrieval code and in the $\vec{\nabla} Z$ calculation, which are the most time consuming steps in the retrieval process, the trace used for the recovery is kept as small as possible. To define the region of interest a program was written that shows the full trace as well as the footprint of the data, which is a trace in which all pixels with amplitude in excess of a certain threshold are represented by 1 and all other pixels are represented as 0. This allows the user to better determine which regions must be included in the final trace while still enabling the user to see the general shape of the trace for the purpose of detecting experimental errors (as evidenced by asymmetries or strong noise). Once the trace has been windowed approximately, the trace needs to undergo two more transformations before the phase retrieval process can be started.

The experimentally measured FROG trace is a function of wavelength λ and delay τ. The phase retrieval code needs traces to be in terms of angular frequency ω and delay τ. Furthermore the conversion from wavelength to frequency requires a conversion in data point spacing from $\delta\lambda$ to $\delta\omega$, the phase retrieval is fastest when delay and frequency have the relation:

$$\delta\omega = \frac{1}{\Delta\tau} \quad \text{and} \quad \delta\tau = \frac{1}{\Delta\omega}$$

Here, δ indicates for the spacing on an axis and Δ indicates for the total range of the trace along the axis. Additionally the Nyquist limit, which requires that the highest frequency component of a signal needs to be sampled at least twice per period, must be exceeded. So in order to find the smallest possible, yet complete, trace that meets all those criteria the code analyzes the trace and finds the Nyquist frequency necessary for that specific trace and then the best spacing in time and frequency. In order to speed up the Fourier transformation in the phase retrieval code the dimensions of the final traces were chosen to be $\frac{\Delta\omega}{\delta\omega} = 2^n$ by

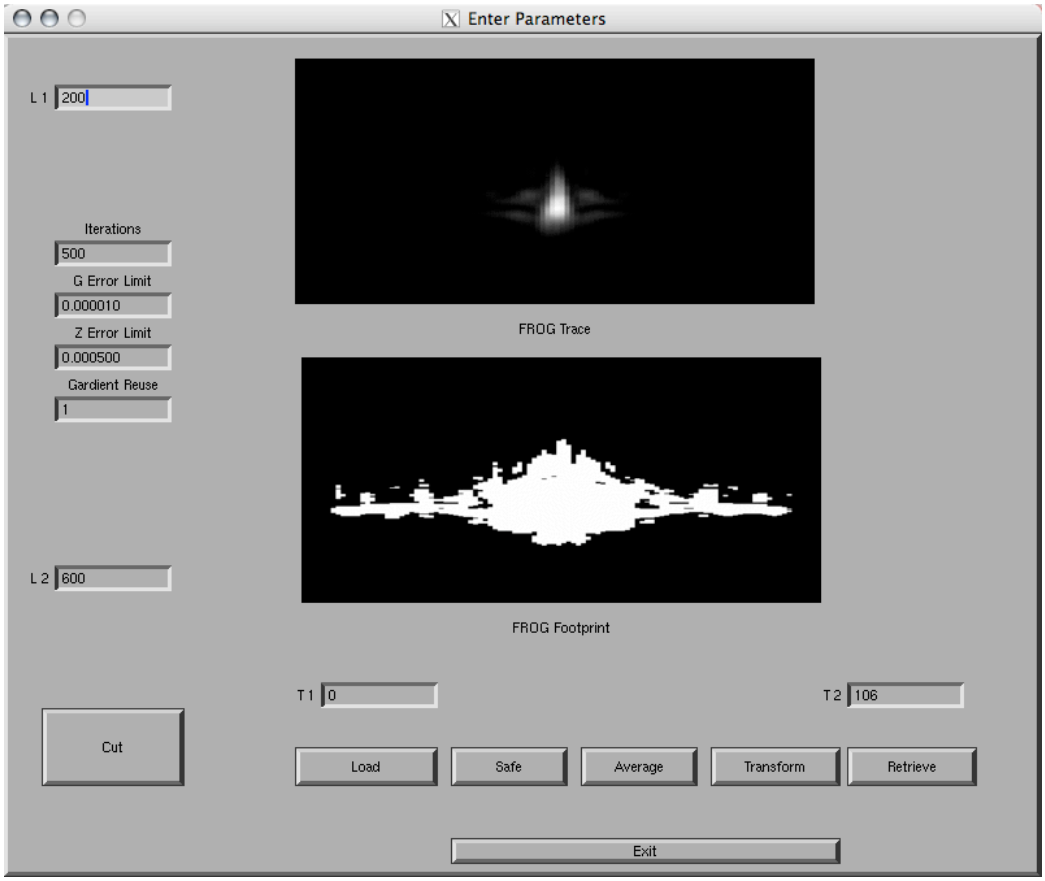

Figure 3.13: Screen shot of the windowing-transform-retrieval program which enables the user to set parameters for the retrieval process. The grayscale FROG trace in the uppermost image in the window is the untransformed trace. The black and white trace below is the footprint of the trace above, showing the regions in which data can be found. It can be seen that the above trace, while being complete, doesn't show all the data due to the limited contrast of the grayscale.

$\frac{\Delta\tau}{\delta\tau} = 2^{n+1}$. The code then interpolates the trace first in the frequency direction (using the spline routine from [152]) and chooses the right values for the desired frequencies. It repeats this process for the τ direction.

The output trace is now ready to be retrieved. The retrieval code allows the user to find the complex field. In cases of doubt the users can test the solution using different retrieval parameters, like different data point spacing, or renewing the $\vec{\nabla}Z$ more frequently. Traces for retrieval can be loaded from a file, as is performed for retrieving the experimental traces, or they can be internally generated from a set of special complex fields. This last option is mainly used for debugging. The code allows additional options for the initial guess E_{initial} with which the program starts the retrieval process. Random initial guesses are allowed, as are specific intrinsic functions or complex fields loaded from a file.

Several parameter can be set to determine when the algorithm terminates. For example the difference between the last and the 20th to last found G_{error} are taken ($\Delta G_{\text{error}} = G_{\text{error}}^{(k-20)} - G_{\text{error}}^{(k)} < \epsilon_1$). If ΔG_{error} falls below ϵ_1, which is typically on the order of 10^{-6}, the retrieval process is considered in stagnation and most likely completed. A similar threshold ϵ_2 can be given for $G_{\text{error}} < \epsilon_2$ itself. Additionally a maximum loop number can be given, after which the retrieval process is stopped. This can be useful when debugging or when in doubt that the FROG trace has sufficient dynamic range.

The code also allows to reuse the $\vec{\nabla}Z$ for a predetermined number of loops m. When $\vec{\nabla}Z$ is recalculated every time $m = 1$.

When the retrieval process is stopped due to one of the above mentioned criteria, the program saves the following data: the complex field (amplitude and phase), intensity profile, the FROG traces generated from this field (as a function of frequency and delay), the measured FROG trace, the autocorrelation signal, the spectrum, the time and frequency spacing, the parameter file and the error of the saved field (Fig. 3.14). With this step the retrieval process is completed.

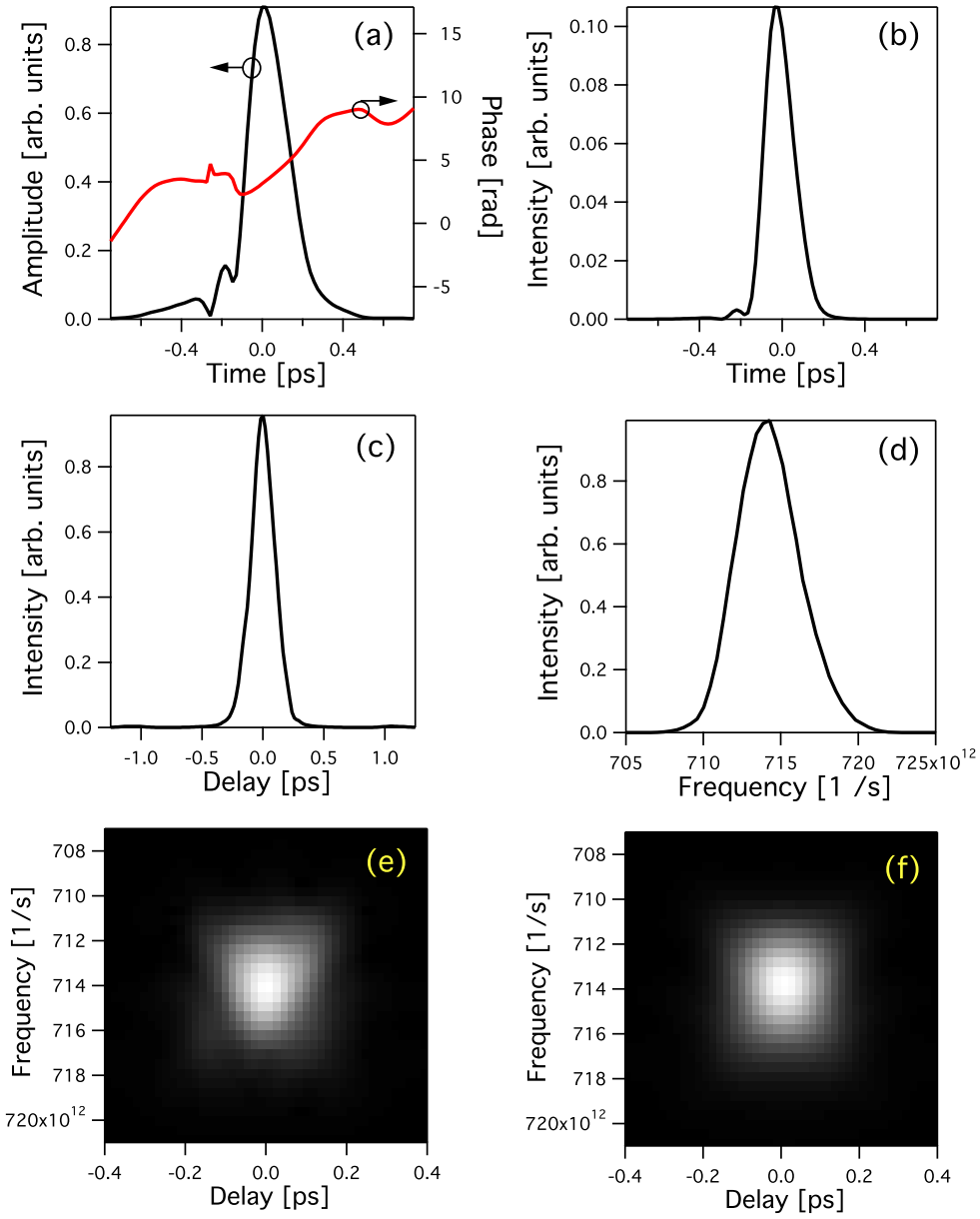

Figure 3.14: The retrieval algorithm produces the following set of results: (a) the amplitude and the phase of the complex field as a function of time. (b) the intensity as a function of time. (c) the autocorrelation signal of the measured trace, obtained by integrating over frequency. (d) the spectrum of the measured trace, obtained by integrating over delay. (e) the measured FROG trace and (f) the FROG trace constructed from the complex field shown in (a).

Smoothing of FROG traces

For some experiments it was not possible to average over sufficient points when acquiring the data. Those traces were often taken at the beginning of the alignment or at the end of the day, as cross checks or to test new settings and showed often considerable noise. While the retrieval code is rather robust against the effects of noise, most of the software used to prepare the trace for retrieval was sensitive to noise. In order to ensure the right choice of frequency and time spacing, grid size and delay, the traces were smoothed using a simple averaging process: *i.e.* to each point the neighboring points were added and averaged, thus acting as a strong low pass filter, thus smoothing out the signal. Only traces with a low signal to noise ratio required this additional processing.

Zero Delay adjustment

Since a SHG-FROG trace is symmetric about $\tau = 0$, the preparation code finds the center of the pulse not from the user defined window (which may not be centered correctly), but by finding the maximum of the autocorrelation signal. This method gave a good estimate but was not always absolutely accurate, due to the noise from the laser system and the low resolution in the delay. While the retrieval process still works correctly, the G_{error} from a FROG trace which is not centered is not meaningful and is no longer an indicator of the quality of the solution. The retrieval code checks at user-defined times in the retrieval process if the delay $\tau = 0$ is correctly centered, and it readjusts if necessary. It does so by calculating the G_{error} for different delays around $\tau = 0$, and selects the delay with the lowest error. This ensures that the correct G_{error} is used throughout the retrieval, thus providing an accurate indicator of the quality of the solution.

Offset Adjustment

To find the correct solution, every phase retrieval algorithm needs a complete set of data in the sensitivity range of interest. While noise, insufficient dynamic range or a detection

threshold of the experiment limits the completeness, the computer generated data has none of these limitations. Comparing incomplete experimental data to computer generated data without taking the limitations of the experiment into account can result in an incorrect interpretation of the data, especially when looking at the low amplitude parts of the solution. As an example, Fig. 3.15 shows a gaussian bell curve the base of which is occluded by the detection threshold and two fitting functions. This data is then fit using two fitting functions. The first fit function only took those values of the bell curve into account which were above the detection threshold and was not allowed to take negative values. It can be seen that the fit to a gaussian is clearly not perfect, *i.e.* the peak is higher and the pulse width is shorter than the original signal. When the the same data is fit using a function that is allowed to negative values (*i.e.* values below the detection threshold), the fit is perfect.

This section presents a way of measuring how much of the low intensity signal is missing and at the same time relaxes the optimization process from its requirement to optimize to incomplete data. This is performed by introducing an adjustable simulated offset to the computer generated data (Fig. 3.16). The method is shown to work for the example of phase retrieval from artificial SHG-FROG traces with different offset levels.

The cornerstone of the phase retrieval algorithm is the minimization of the difference between the measured data set and a generated set of potential solutions. If the measured data lacks low intensity features found in the desired correct solution, the optimization process will try to suppress the low intensity features in the solution. To avoid this problem an artificial offset is imposed on the computer generated data so that it does not show any signal in regions where the measured data set is zero. The minimization process is now free to accept solutions that show low intensity signal in those regions where no signal was detected. The solution will be unique so long as enough data remains so that the problem is overdetermined (with a problem-specific complex conjugate ambiguity). As before a steepest-descent method is used to retrieve the complex field from SHG-FROG traces [130; 159].

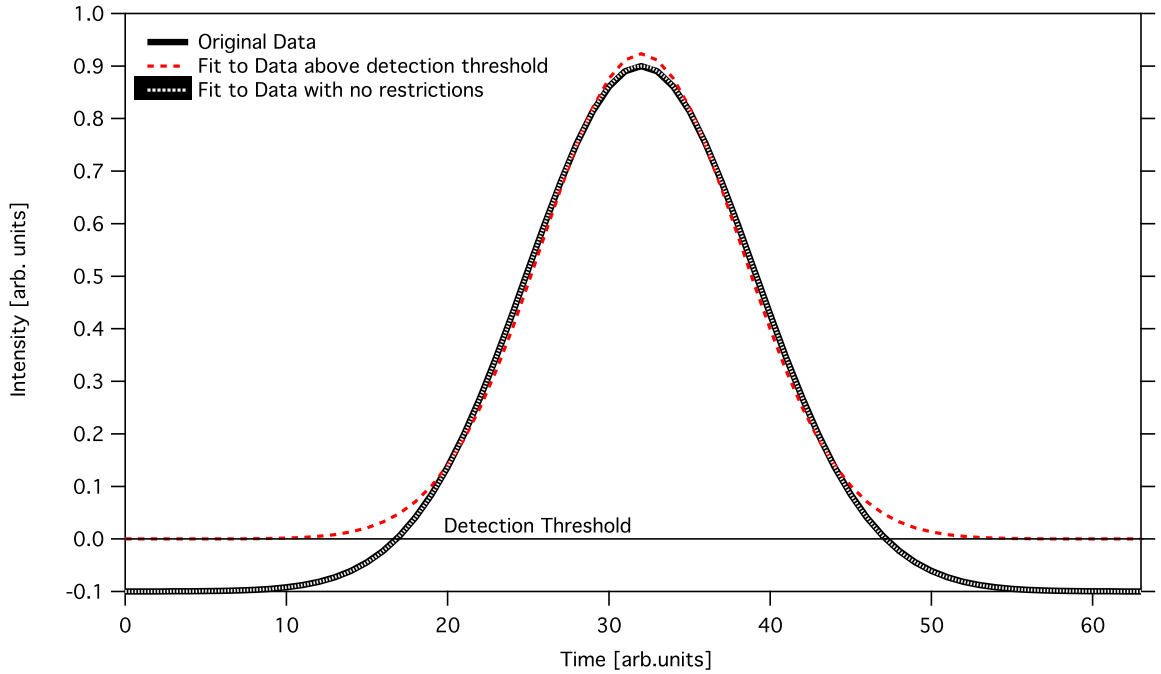

Figure 3.15: The solid black graph shows the original data, the red dashed line the fit which is not allowed to take negative values, and the white dotted line is the fit which uses the same data as before but has no restrictions on the value taken.

The offset compensation (OC) takes place in the optimization step (Fig. 3.16) which leads to $g^{(k+1)}(t)$. In order to find the optimal $x_{\min}$ temporary fields $E_{\text{temp}}(t)$ are constructed using different scaling factors x. From these $E_{\text{temp}}(t, x)$ a trace $g_{\text{temp}}(\tau, t, x)$ is constructed to be compared with $g'(\tau, t)$. Now a second, embedded optimization process determines the offset of $g'(\tau, t)$ before comparing it with $g_{\text{temp}}(\tau, t)$. In order to do so, $g_{\text{temp}}(\tau, t)$ is Fourier transformed into the frequency domain $G(\omega, \tau)$ and its footprint is compared to the footprint trace of the original measured trace. The footprint trace shows a 1 for every point with signal and a 0 for every point without signal on the original trace. The footprint of $G_{\text{temp}}(\omega, \tau)$ is recalculated for different offsets and compared to the footprint of the original trace. The offset O for which both footprints overlap best is used to generate a new trace $\hat{G}_{\text{temp}}(\tau, t)$.

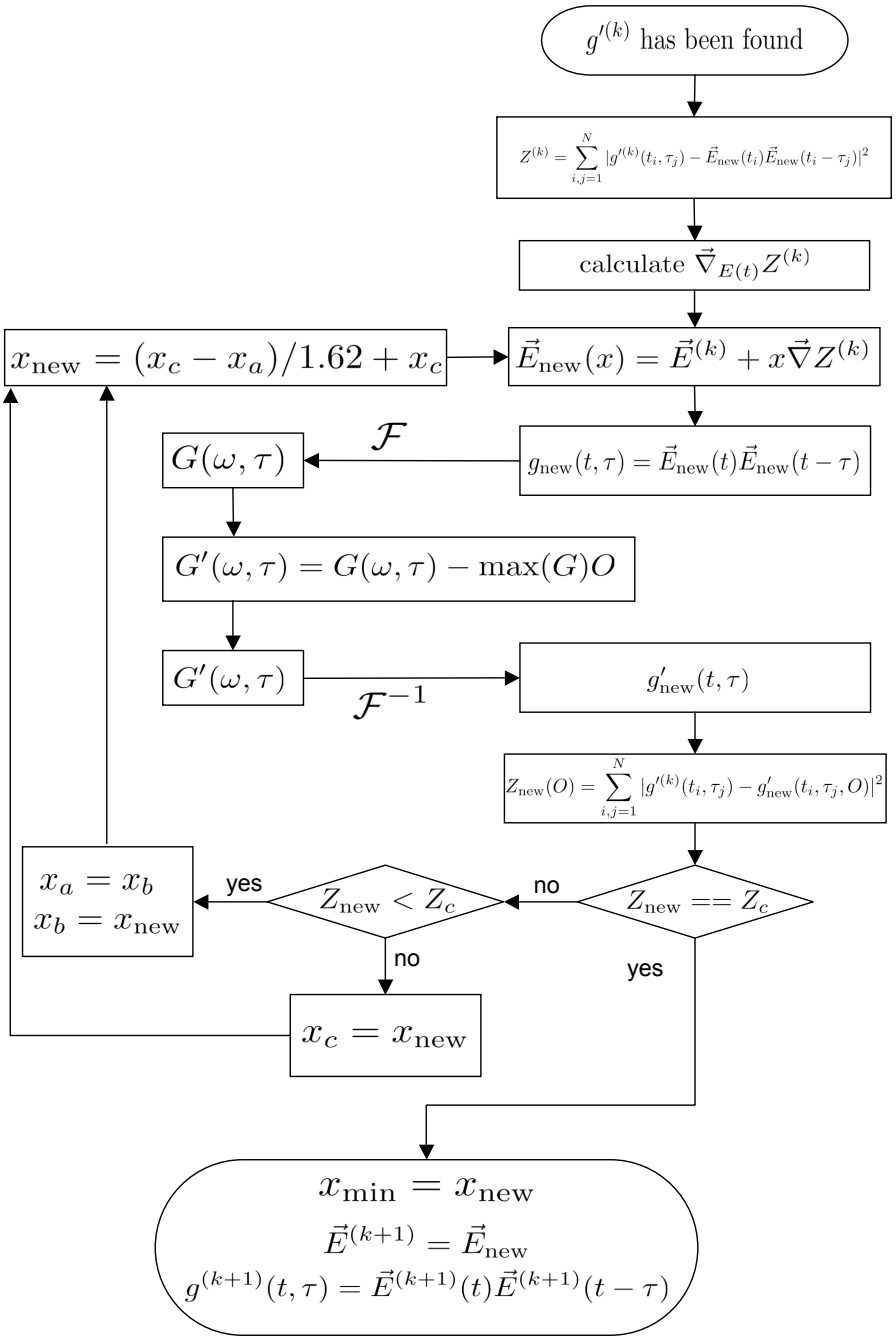

Figure 3.16: shows the standard FROG retrieval code including the OC loop. In order to safe computational resources the OC loop is only used when required or wanted in the retrieval process.

$$\hat{G}_{\text{temp}}(\tau, f) = \begin{cases} G_{\text{temp}}(\tau, f) - O & \text{if } G_{\text{temp}}(\omega, \tau) \geq O; \\ 0 & \text{if } G_{\text{temp}}(\tau, f) < O. \end{cases} \tag{3.22}$$

Here $\hat{g}_{\text{temp}}(\tau, t)$ is the back Fourier transformed function and used in the optimization process for $x_{\min}$.

The method is computationally expensive, since every optimization step requires at least two additional Fourier transformations and an additional optimization process. This disadvantage is partly compensated for by a faster convergence of the solution for the investigated test cases and the advantage of the offset as an additional quality parameter. To further reduce the computational cost, the offset optimization step is only included after the progress of the standard phase-retrieval process has slowed down. This is the case when the algorithm has found a field that agrees in the high amplitude parts with the solution. The OC method only effects the low amplitude regions of the solution, which are found at a later stage of the optimization process.

Table 3.1: G_{error} depending on offsets with and without the OC.

Threshold O in Percent	G_{error} without OC	G_{error} with OC	O Measured by OC in Percent
0	0.0013	0.0013	0
0.5	0.0070	0.0049	0.5
1.0	0.0145	0.0095	1.0
2.0	0.0290	0.0190	2.0
3.0	0.0432	0.0338	3.0
4.0	0.0557	0.0454	4.0
5.0	0.0648	0.0567	5.5

In order to test this method a pulse train with five pulses of different maximum amplitude and flat phase was constructed. Different detector thresholds were simulated by subtracting different percentages of the maximum intensity from the traces in the frequency domain, simulating a detector with a detection threshold or a limited dynamic range. Those traces were used in the phase retrieval processes with and without the use of the OC-method

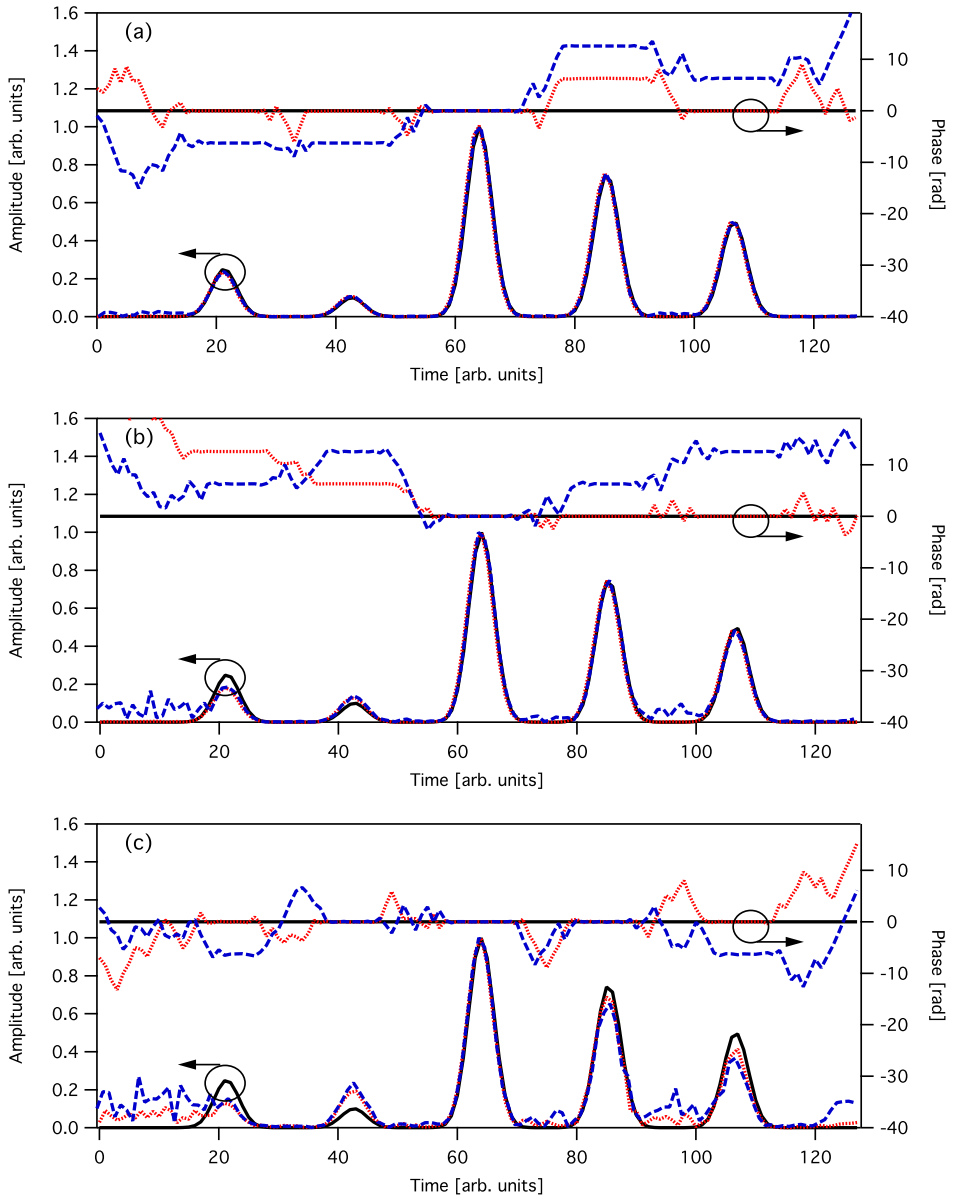

Figure 3.17: Amplitude and phase of the original complex field (solid lines), solution found by the phase retrieval using the OC method (dotted lines), and solution found by the phase retrieval without using the OC method (blue dashed line), for an data offset of (a) 0.5%, (b) 2.0%, and (c) 3.0%.

introduced here. The original complex field and the retrieved solutions are shown in Fig. 3.17. The peak pulse amplitude was normalized to 1 so the ratios between the pulse amplitudes give good indication of the quality of the solutions. It can be seen that at an offset of 0.5 % (Fig. 3.17.a) of the maximum value of the measured trace does not significantly affect the overall solution in either case. The only notable difference is that the solution found without the OC method shows some low level amplitude and phase noise in the regions between the pulses. The reader may wish to note that even though both solutions show a flat phase for all pulses, the flat regions are shorter in the unadjusted solution, which causes low level amplitude noise. For offset of O = 2.0% (Fig. 3.17.b) both solutions show deviations from the original complex field for the lowest amplitude pulses. While the OC method solution still shows no sign of amplitude noise between the pulses, the solution found without OC does show significant amount of noise, making it difficult to distinguish between pulses and noise. At 3.0% (Fig. 3.17.c) both solutions show significant changes in the amplitude ratios between the pulses and noise in the regions between the pulses. The offset adjusted solutions show less noise and little change from the correct solution for the three high amplitude pulses. While the noise level of the solution obtained with the OC method is now high enough to possibly obscure the first pulse on the right, it is considerable lower than the noise level in the solution found without OC. Note that the solution without OC found a spurious pulse on the right for which there is no equivalent in the original pulse train. The correct amplitude of the smallest pulse was found by neither method at this offset level.

The G_{error} calculated when using the OC method is significantly lower than that obtained without (Table 3.1). All traces used here were 128 by 256 points. The offset measurements made by the OC method are in good agreement with the real offsets, O. (Table 3.1) .

It has been shown that the introduction of an artificial offset to the steepest descent phase retrieval method [130] makes the solution less sensitive the data that are incomplete due to a detection threshold. The solution yields less noise and stays closer to the original field for higher detection thresholds while the G_{error} is significantly reduced. The amount

of missing data can be measured by the OC method in order to give a better estimate of the accuracy of the retrieved solution than does the G_{error} alone. Measurements with high dynamic range, such as high dynamic FROG [171; 172] clearly benefit from this addition to the algorithm.

3.4 FROG Simulation

The results from a series of pulse propagation simulations were used to interpret the results found in the experiments. In order to usefully compare the computer simulations with the experimental data, it is necessary to simulate the entire experimental measurement process rather than simply examine the raw results from the pulse propagation simulation.

3.4.1 spatio-temporal Dependenc

For the FROG experiment, one has to make the important assumption when recovering the complex field from the FROG trace, that the pulse does not exhibit a spatio-temporal dependence, *i.e.* the pulse shape has no spatial dependence and that the full field $E(x, y, z, t)$ can be expressed in the form $E(x, y, z, t) = f(x, y)g(z, t)$, with $f(x, y)$ and $g(z, t)$ describing the beam shape and pulse shape, respectively. This assumption is necessary since in the experiment, pulses from different points of the beam interact with each other, creating a signal beam Fig. 3.18. For the case of spatio-temporal dependences in the correlated beams, the signal will have a spatial component as well. In the experiment, the detector averages over the whole signal beam when measuring the spectrum. This leads to a FROG trace in which the pulse shapes at different positions in the beam have been mixed with each other. If there is a spatial dependence of the temporal pulse shape, the FROG trace looses its uniqueness, since the solution for an asymmetric beam must now be three dimensional (x, y, t) instead of one dimensional (t). The FROG trace is a two dimensional object (ω, τ) that is averaged over x and y. This means that for the case of a field with a spatio-temporal dependence the problem is under-sampled, *i.e.* no unique field can be found from the information provided. It

is furthermore impossible to retrieve the full field with spatio-temporal dependence without further knowledge about the spatial distribution of the pulses.

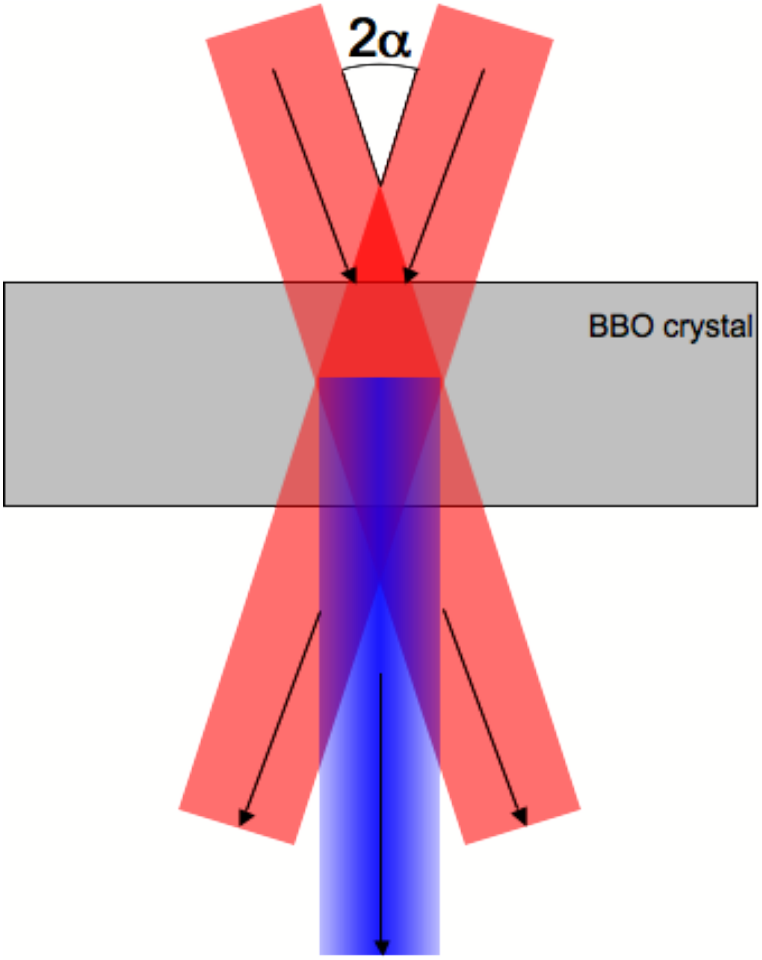

Figure 3.18: This schematic shows the two beams (in red) enter the BBO crystal at angle α creating a doubled autocorrelation signal (in blue), which leaves the crystal at normal incidence. It can be seen that, under certain circumstances, the potential interaction zone between the original beams is longer than the BBO crystal thickness. The FROG simulation code limits the interaction to the inside of the BBO crystal.

For measurements without a sample, or pulse energies of 10% or less of the destruction threshold, computer simulations indicate that it is reasonable to assume that the pulse shape does not vary significantly over the beam profile.

In order to compare the experimental data for energies close to destruction where computer simulations predict a strong spatio-temporal dependence, a program was written to

simulate the second harmonic generation for two interacting beams with spatio-temporal dependences at different delay times τ, interaction angle α (as shown in Fig. 3.18). The SHG signal is Fourier transformed into frequency space. For each delay time τ the spectrum is averaged over the beam, generating a FROG-like trace which resembles an experimental FROG trace from a beam with spatio-temporal dependences.

The interaction angle α for the experiments was in the range $\alpha = 2.5° - 5.0°$. The incoming pulse was tilted by an angle α and transfered onto a separate grid, with accordingly adjusted spacing. Note that the relation between the sampling frequency in x and the sampling frequency in z are now related by $\tan\alpha = \delta x/\delta z$, where δx and δz are the space increments in the respected direction, due to the fact that every time step includes one step in the x and the z direction. The second harmonic signal was found from multiplying the regions in which the two beams overlap and adding the result to a third grid, which stores the second harmonic signal. Since the interaction zone in the laboratory is limited to the nonlinear crystal, the program calculates the time steps for which the pulses are in the interaction zone and takes only second harmonic signals from inside the crystal into account.

In the next stage, the pulse at every point in the second harmonic beam is Fourier transformed into frequency space. The Fourier transformed signals are then averaged over the beam into a single spectrum. In a manner similar to the experiment, where the beam is first spectrally resolved by a grating and then focused on a CMOS array to average over the beam. To speed up this process the beam is split into multiple sections along the y axis, which are calculated separately. This is possible since only electric fields with the same y-value interact, therefore allowing the calculations to be run independently on different CPU's. The results are then combined to reconstruct the final pulse.

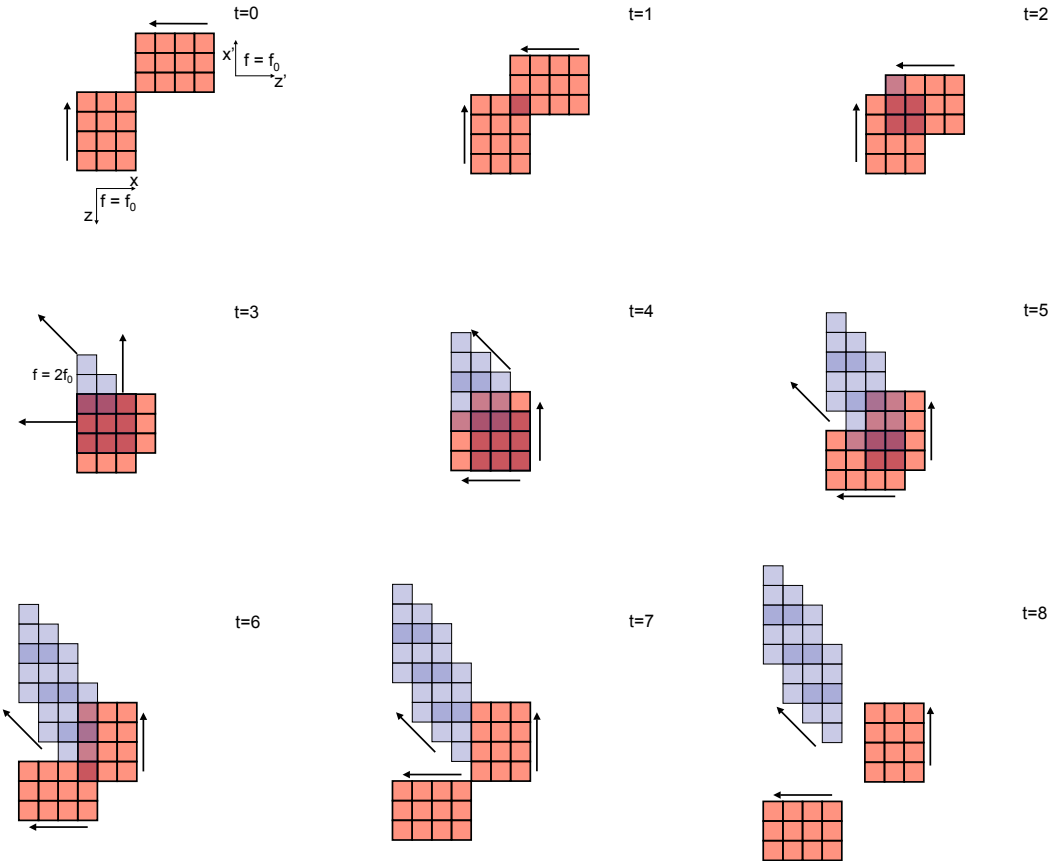

Figure 3.19: Step by step second harmonic generation for the special case of interaction angle $\alpha = 45°$ and delay $\tau = 0$. The two dark rectangular grids represent the two pulses interacting in the crystal with each other. The lighter gray cells represent the second harmonic generation signal, produced by the interaction between the two initial pulses. The darker cells represent points for which different SHG signals have been added together.

3.4.2 Simulation of the Experiment

As shown in Fig. 3.6, the experiment uses a lens to focus the beam on the sample surface. It was not possible to measure the beam profile and spatial phase of the beam at the sample surface. Therefore a beam profile taken before the telescope was Fourier transformed to simulate the beam propagation to the sample surface and used to construct the input field used by the pulse propagation code.

After the sample, the field has spatial temporal dependences, which means that the beam profile varies with time. For this reason each time slice as given by the pulse propagation simulation, was inverse-Fourier transformed individually to the lens. This process clearly cannot include any nonlinearities in air and so was cross checked against a full pulse propagation calculation which included the nonlinearities in air. As shown in Fig. 3.20, the methods agree with each other. The pulse propagation algorithm produces beam profiles with a lower resolution due to computer memory requirements of the technique, while the Fourier transform technique can work with each time slice at the time, which greatly reduces the memory requirements and thus allowing the use of higher spatial resolution.

The user can choose to aperture the beam with a pinhole of a given size after the inverse-Fourier transform. This corresponds to the pinhole which was positioned at the beam profiler position in Fig. 3.6. The apertured beam is then Fourier transformed again to simulate the focusing into the nonlinear crystal. The generation of the FROG trace from this field is simulated using the code described in the previous section.

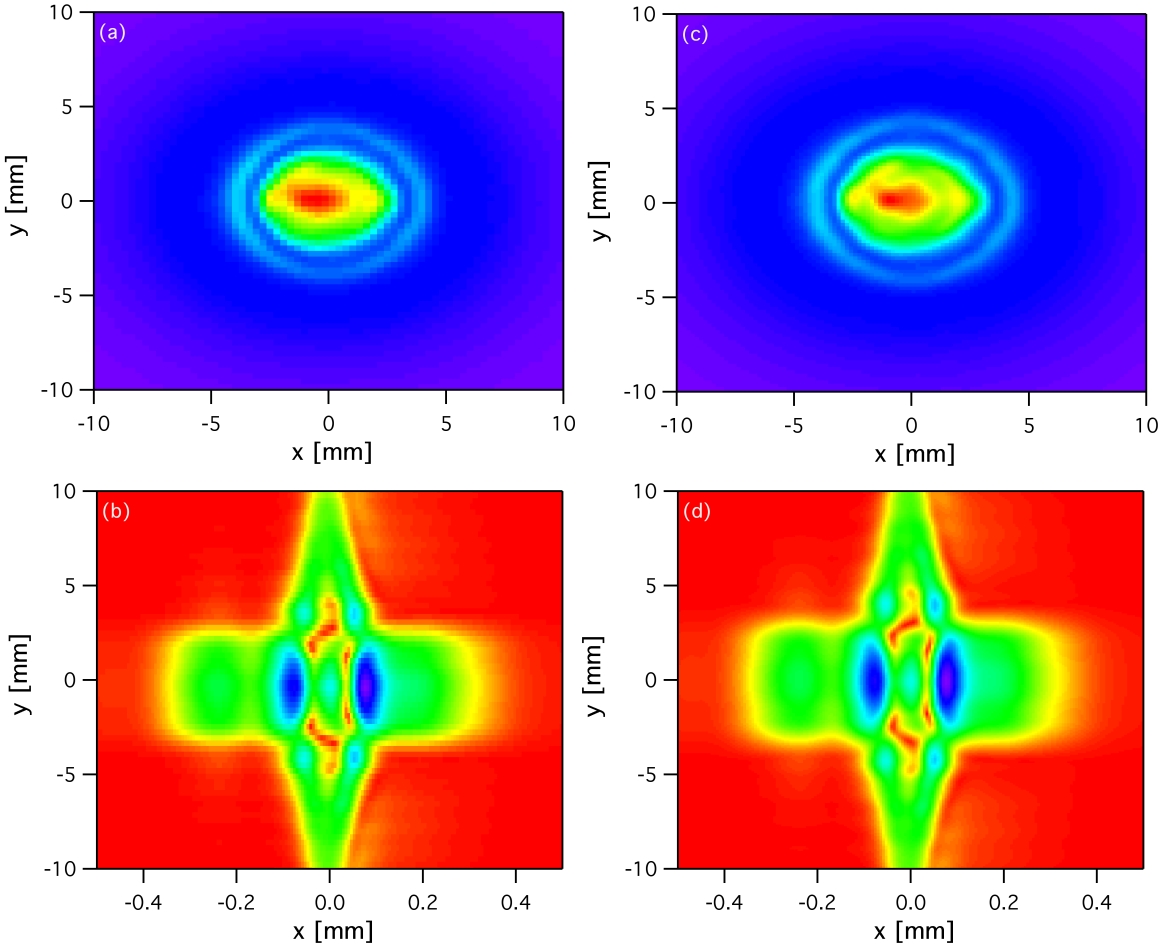

Figure 3.20: (a) and (c) show the beam profile and amplitude of a field respectively obtained using the pulse propagation code. The beam profile in (b) and the amplitude map in (d) show the same initial field as before and were obtained using the Fourier transformation method.

Chapter 4

Experimental Results and Comparison with Computer Simulation

4.1 Experimental Results

FROG data from different experiments exhibit varying degrees of spatio-temporal dependence. While many traces are therefore not retrievable they do show interesting features and enable one to draw useful conclusions about the field. The FROG results presented in this chapter are divided into (i) FROG data with strong spatio-temporal dependences which are not retrievable, and (ii) FROG data that was retrievable. Data on beam profiles is also presented, analyzed and discussed.

4.1.1 "Unapertured" FROG traces

In all of the work described below, reference FROG traces were taken by performing measurements either without a sample or at very low energy.

It is important to note that the inherent instability of the laser system is amplified by both the nonlinear effects in the sample and the measurement process. For energies close to the destruction threshold, these effects become more prominent. It is therefore expected that when the retrieval results from low pulse energy experiments are compared with retrieval results from of high pulse energy experiments, the G_{error} increases with energy. Additionally, with increasing energy, the measured FROG traces develop features that are absent in the FROG traces constructed from the retrieved solution. In particular, there is a prominent characteristic splitting of the center maximum, which is accompanied by a lengthening of the pulse. It is noteworthy that the retrieved solution does not show the splitting of the center maximum. The pulse evolution described above is exhibited by the FROG traces shown in

Fig. 4.1. Note that the autocorrelation signals give no indication of this evolution. If the experiment had been performed using an autocorrelation measurement instead of FROG to analyze the output field, the signal would certainly have been interpreted as a simple lengthening of the pulse.

For the FROG data shown in Fig. 4.1, the solutions for the complex fields found by the retrieval code are shown in Fig. 4.2. For comparison, the fields have been normalized to the small pre-pulse on the left. It can be shown that this is the front of the pulse. Computer simulations indicate that a small trailing pulse would be absorbed for higher pulse energies, which is not observed here, hence the smaller pulse must be preceding the main pulse [151]. It should be noted that even when comparing the solutions found by the retrieval algorithm, one might presume that the pulse has been stretched. The fields found for energies well below the destruction threshold (60μJ for data in Fig. 4.1) show good agreement with each other. With increasing energy the phase stays flat while the amplitude in the center decreases and the pulse lengthens in time. Only when comparing the measured FROG traces with the retrieved FROG traces does it becomes apparent that the field cannot be retrieved for energies of 35 μJ and higher.

Misalignment of the experiment can be ruled out as the cause for this behavior, since the lower pulse energies yield a valid solution, which would not be the case otherwise. It is very unlikely for instabilities in the laser resulting in a slow drift of the beam or the pulse shape over the time of the experiments to be responsible, since the different traces were taken in a non-sequential order. As a result the traces taken in sequence should show more similarity than the traces with similar energies, which is clearly not the case.

Spatio-temporal dependences in the field are therefore the most likely cause of the unretrievable features in the FROG traces. While no pinhole was used to aperture the beam for this set of experiments, the optics in the experiment restrict the beam to a maximum of 1" diameter. The beam was 6 mm in diameter before the first lens. After the telescope, the diffraction caused by the interaction with the sample can dramatically increase the spatial

extent of the beam. This leads to a loss of information when the pulse propagates through the remaining optical components, furthermore computer simulations indicate aperturing at this level can lead to a major reshaping of the pulse.

Table 4.1: G_{error} and offset compensation (OC) for the retrieved complex fields in Fig 4.2.

Pulse Energy	Trace Dimensions	G_{error}	OC
10 μJ	256×128	0.00692	0.013
22 μJ	256×128	0.00645	0.0165
35 μJ	256×128	0.00906	0.012
40 μJ	256×128	0.00968	0.018
60 μJ	256×128	0.01657	0.026

The FROG traces shown in Fig. 4.3 were measured using different amplifier and compressor settings, thus explaining the different shape of the FROG trace, which were taken as an alignment check for the experiment at the time. While the FROG trace for the low pulse energy is retrievable, the trace for 30 μJ input pulse energy indicates significant spatio-temporal dependences in the field and is thus unretrievable. The center maximum has split into two maxima, and the center region becomes wider. It will be shown later that this feature is recreated in FROG traces generated from computer simulations.

Fig. 4.4 illustrates the change in the FROG traces for pulse energies close to the destruction threshold. The measured FROG traces in Fig. 4.4 show a dramatic change in form as the damage threshold is approached, as do the retrieved solutions, even though the experimental and retrieved traces clearly differ in shape. The destruction threshold for this series was observed at 45 μJ since the sample was burned while acquiring the FROG trace at this pulse energy. It will be shown later that this kind of change is expected close to the destruction threshold as the pulse develops strong spatio-temporal dependences due to the laser pulses interaction with the material and the resulting electron plasma.

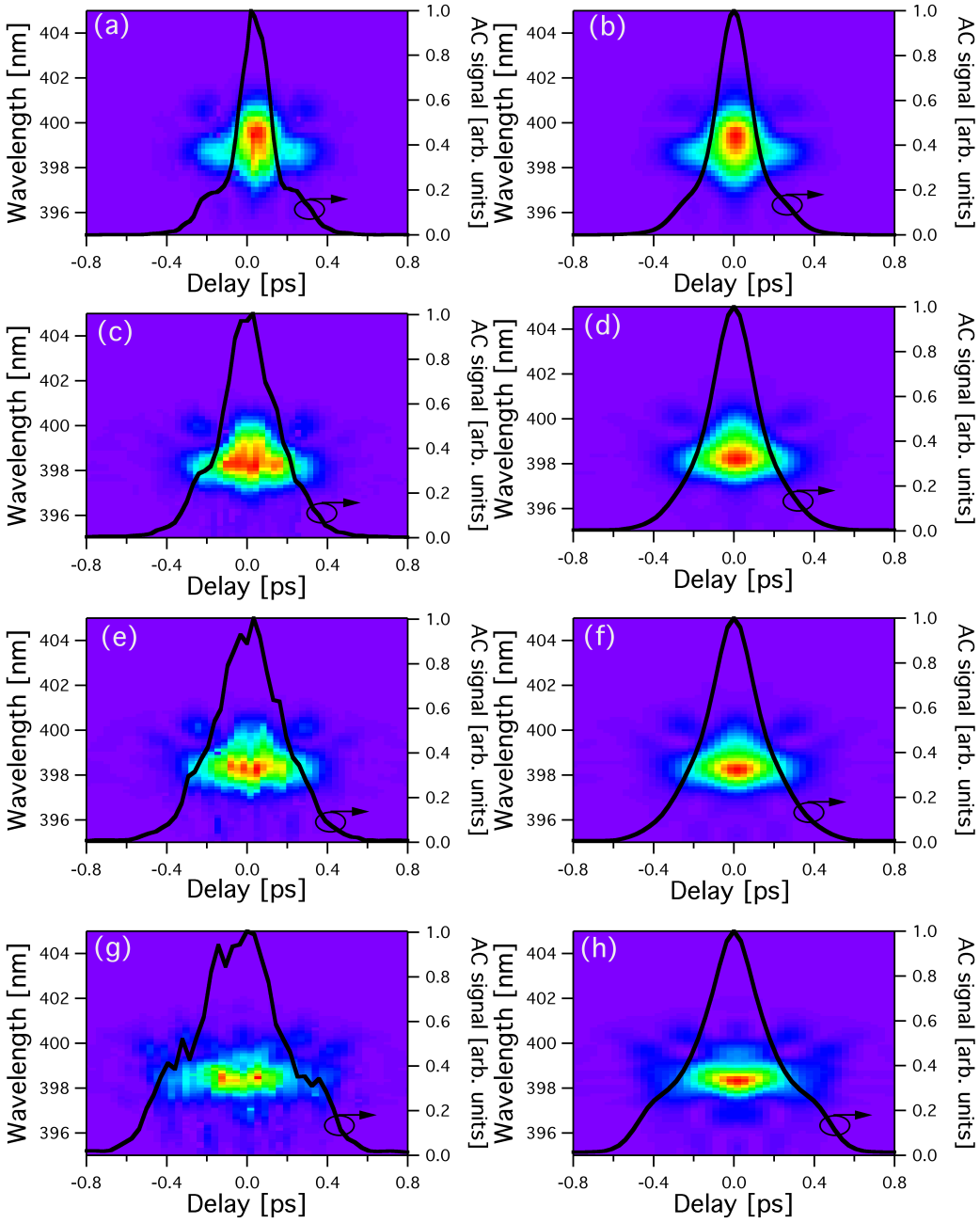

Figure 4.1: Measured FROG traces and their corresponding autocorrelation signal (full line) and the FROG traces found by the retrieval code. Fig. (a) and (b) are the measured and retrieved FROG trace respectively for a pulse energy of 10 μJ. Fig. (c) and (d) are the measured and retrieved FROG trace respectively for a pulse energy of 35 μJ. Fig. (a) and (b) are the measured and retrieved FROG trace respectively for a pulse energy of 40 μJ. Fig. (g) and (h) are the measured and retrieved FROG trace respectively for a pulse energy of 60 μJ. Destruction of the sample was observed at 60 μJ.

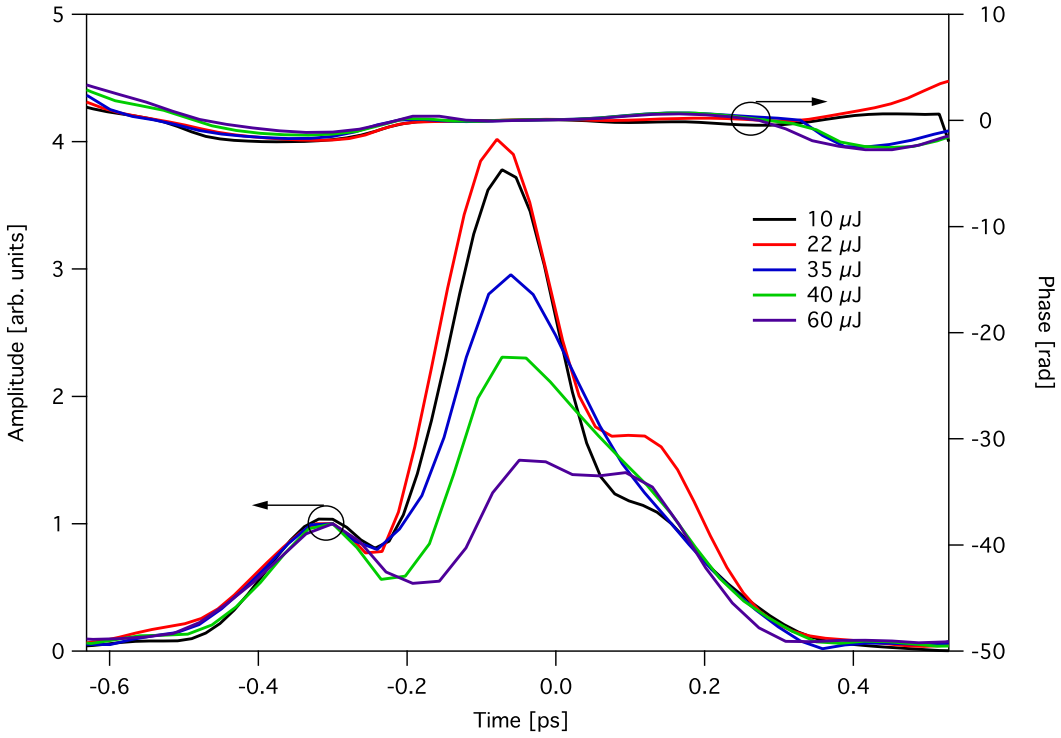

Figure 4.2: The amplitude and phase of the retrieved complex fields for different input pulse energies. The solutions for 10 μJ and 22 μJ show great similarity in both phase and amplitude, while the solutions for higher energies change greatly in terms of pulse shape. The complex fields were retrieved from the FROG traces in Fig. 4.1.

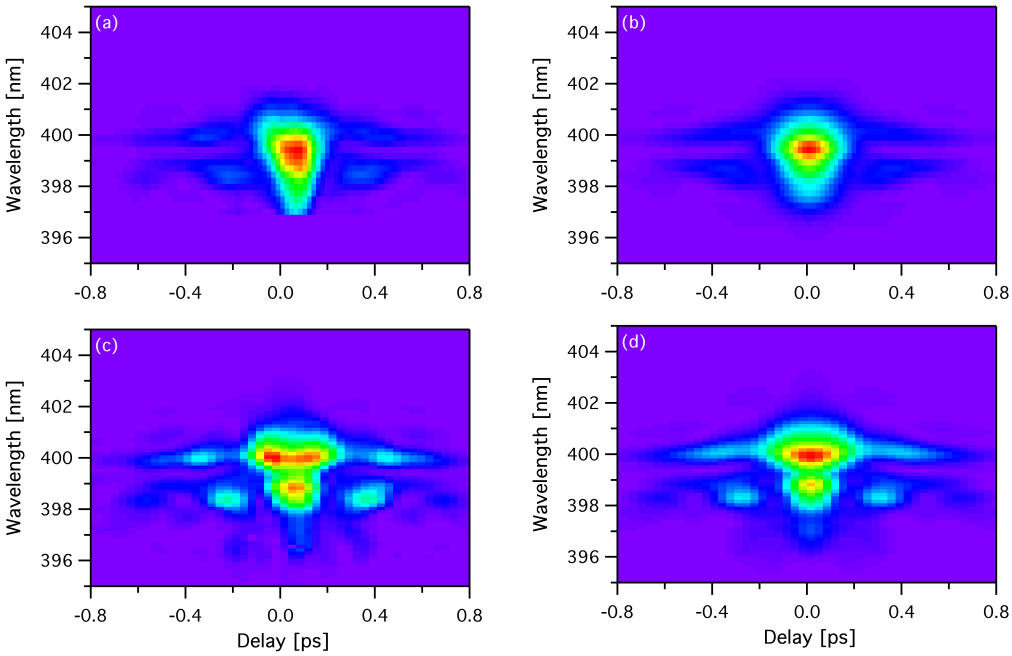

Figure 4.3: The measured FROG traces that occurs of pulses with (a) 10 μJ and (c) 30 μJ input energy. (b) and (e) are the retrieved solutions for the measured traces (a) and (c) respectively. Destruction of the sample was observed at 55 μJ.

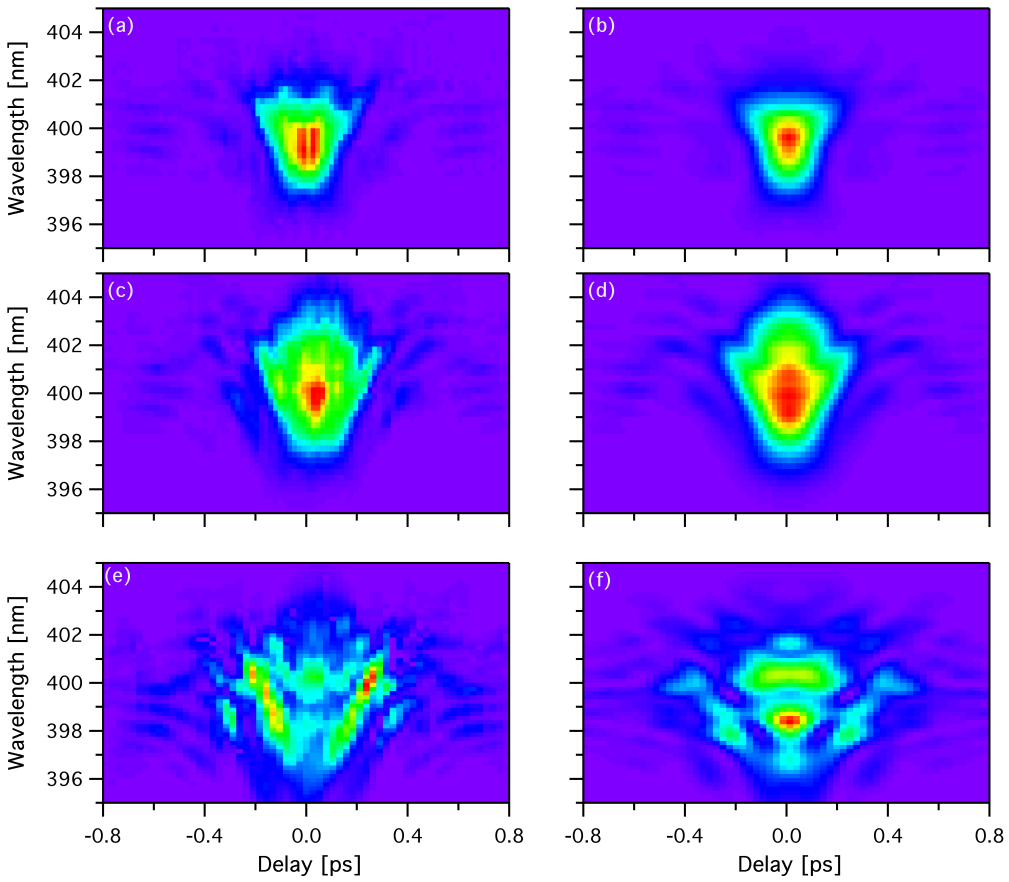

Figure 4.4: (a) and (b) are the measured and retrieved FROG traces for a pulse energy of 10 μJ respectively. (c) and (d) are the measured and retrieved FROG traces for a pulse energy of 40 μJ respectively. (e) and (f) are the measured and retrieved FROG traces for a pulse energy of 45 μJ respectively. The destruction threshold of the sample was observed at 45 μJ.

4.1.2 Apertured FROG traces

When the beam is apertured with an adjustable pinhole placed just behind the recollimating lens, the traces acquired at low pulse energies remain unchanged, while the acquired FROG traces at high pulse energies become retrievable. Fig. 4.5 shows the FROG traces from an apertured beam at different energies with the matching autocorrelation signals and the FROG traces found from the retrieved solution. The destruction threshold for this sequence was 55 μJ. Again, at energies close to the destruction significant differences between the measured and retrieved FROG traces become apparent. These differences are considerably less than those observed when using the full beam, but are nonetheless still present. This indicates that even though the spatio-temporal dependences have been reduced, some are still present. The retrieved fields for this experiment are shown in Fig. 4.6, while the errors associated with the retrieval process are listed in Table 4.2. With the apertured beam profile the retrieved fields at higher energies decrease in contrast ratio between the pulse peak and the pre-pulse amplitude while the phase does not show any sign of self phase modulation. Retrievals from artificial FROG traces show that the phase information is lost when strong spatio-temporal dependences are present. Simulations also indicate that using a pinhole to reduce the spatio-temporal dependences greatly reduces the phase modulation in the center of the pulse.

A possible explanation for the increase in the peak-power for low energies is self-focusing. The computer simulations show that the beam is self-focusing at the pulse center ($t = 0$) for pulse energies in excess of 10 μJ. Therefore, more energy passes through the pinhole in the beam path for the self-focused parts of the pulse, which is reflected in the retrieved solutions by an increase of the pre-pulse to peak ratio. The decrease in the peak-power for higher energies can be explained with the development of spatio-temporal dependences and absorption in the electron plasma. The spatio-temporal dependences lead to an increase in beam width at the pulse center ($t = 0$) and an increased energy loss at the pinhole.

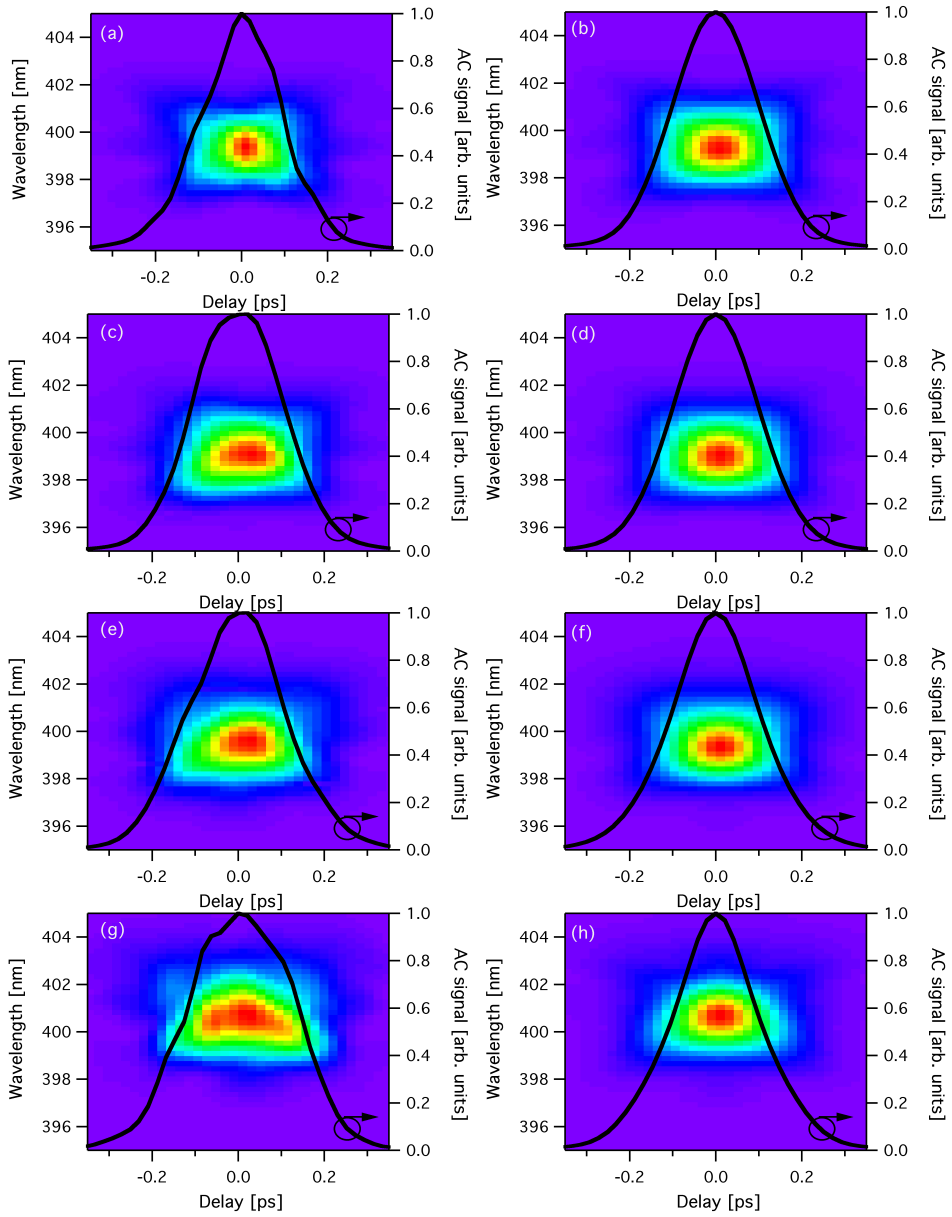

Figure 4.5: Measured FROG traces with the corresponding autocorrelation signals (full line) and the FROG traces found from the solution for an apertured beam. (a) and (b) are the measured and retrieved FROG traces for a pulse energy of 1 μJ respectively. (c) and (d) are the measured and retrieved FROG traces for a pulse energy of 10 μJ respectively. (e) and (f) are the measured and retrieved FROG traces for a pulse energy of 35 μJ respectively. (g) and (h) are the measured and retrieved FROG traces for a pulse energy of 46 μJ respectively. The destruction threshold for this sequence was 55 μJ. The complex field solutions for this set are shown in Fig. 4.6.

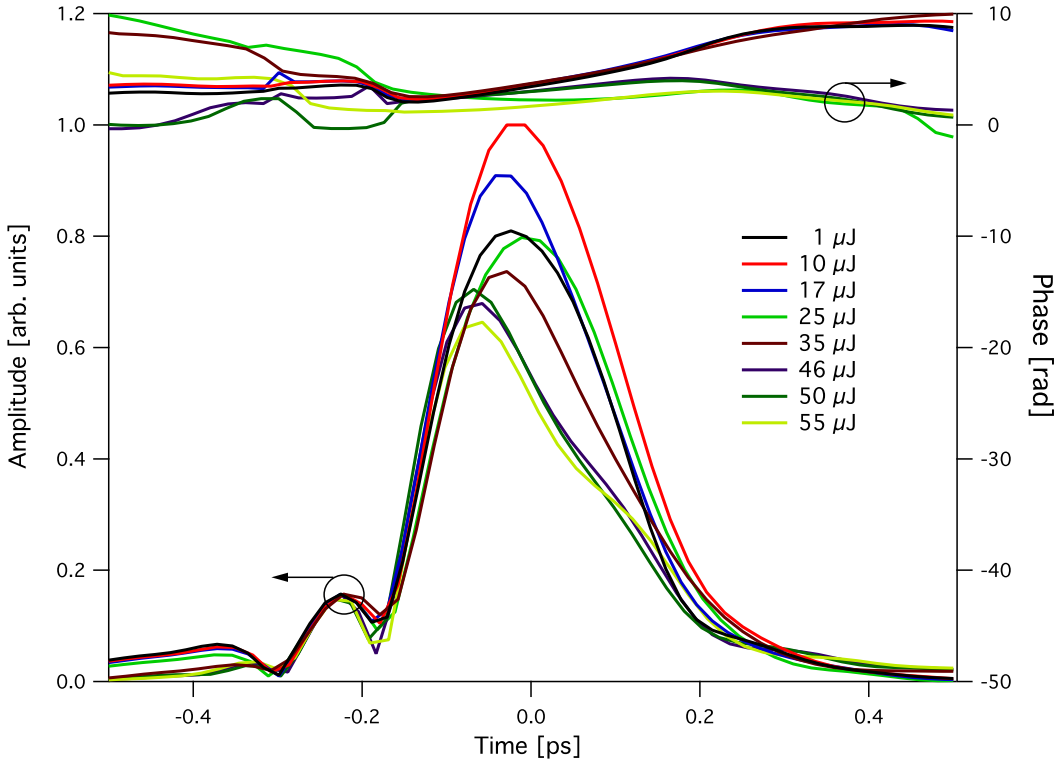

Figure 4.6: The complex field (amplitude and phase) retrieved from FROG traces (shown in Fig. 4.5) measured at different pulse energies. The front of the pulse is on the left (earlier in time). The errors for the retrieval processes are given in Table 4.2.

The amplitudes of the fields were normalized to the small pre-pulse on the left, since the nonlinearities have little or no effect on the behavior of the pulse, but this feature is in all cases well above the noise. The experimental results shown in Fig. 4.5 and Fig. 4.6 were conducted using a laser system at the Laboratoire Hubert Curien of the Université Jean Monnet in Saint Ètienne.

The pulses shown in Fig. 4.7 are the retrieved from FROG traces of apertured fields measured at UGA. The destruction threshold of the sample was reached at 50 μJ. The solutions show similar behavior to that shown in Fig. 4.6. It is notable that the phase stays flat for all energies and the maximum peak amplitude / pre-pulse amplitude ratio is reached at an intermediate energy that is well below the destruction threshold.

Table 4.2: G_{error} and offset compensation (OC) for the retrieval process of the complex fields in Fig 4.6.

Pulse Energy	Trace Dimensions	G_{error}	OC
1 μJ	256×128	0.00319	0.0115
10 μJ	256×128	0.00417	0.0135
17 μJ	256×128	0.0036	0.0105
25 μJ	256×128	0.0041	0.008
35 μJ	256×128	0.00623	0.01
46 μJ	256×128	0.0051	0.011
50 μJ	256×128	0.00536	0.0095
55 μJ	256×128	0.0062	0.01

Table 4.3: G_{error} and offset compensation (OC) for the retrieved complex fields in Fig 4.7.

Pulse Energy	Trace Dimensions	G_{error}	OC
No Sample	128×64	0.0096	0.0115
10 μJ	128×64	0.0059	0.0085
20 μJ	128×64	0.0063	0.0135
40 μJ	128×64	0.0066	0.0105
50 μJ	128×64	0.0117	0.013

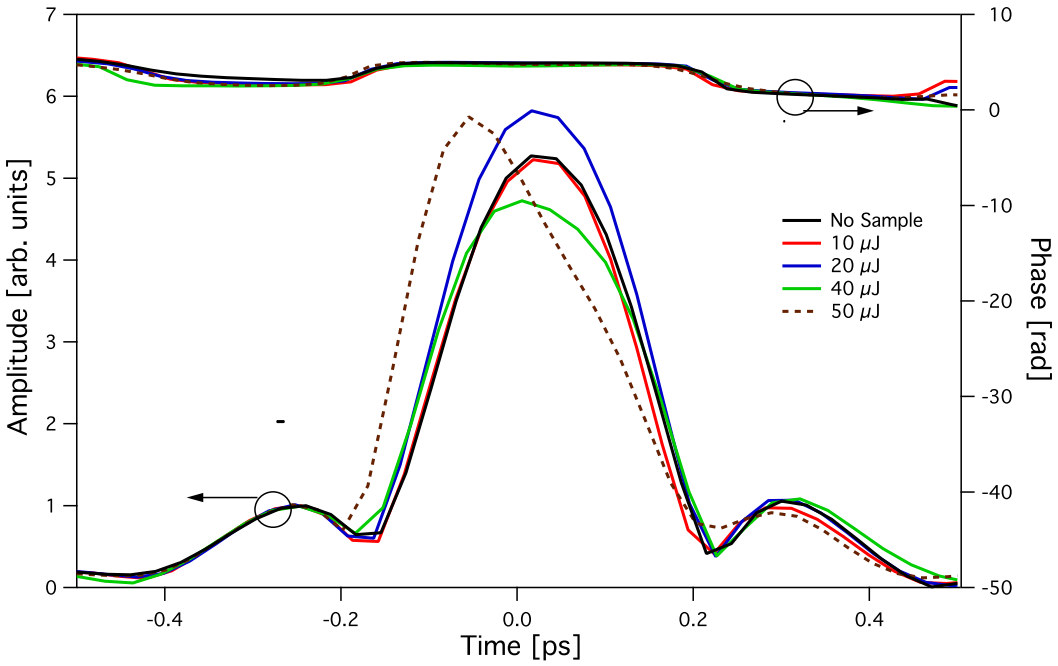

Figure 4.7: The complex field (amplitude and phase) retrieved from FROG traces at different pulse energies. The front of the pulse is on the left (earlier in time). The errors for the retrieval process are given in Table 4.3. Destruction of the sample occurred at a pulse energy of 50 μJ. The field from the FROG trace measured at 50 μJ is shown with the dashed line to distinguish it.

4.1.3 Beam profiles before and after the sample

In order to better understand the results from the FROG measurements, beam profile measurements were acquired before the first lens and at different pulse energies after the recollimating lens. The pulse profile before the lens, as shown in Fig. 4.8(a), exhibits diffraction rings due to aperturing by the polarizing cube used in the attenuator for the power regulation. The pulse profiles behind the lens without a sample and at low energies are very similar to the input beam profile at measured before the sample. For increasing pulse energies the center of the beam loses energy while a clear visible outer ring with hot spots becomes the dominant feature. The ring does not change greatly for different input pulse energies. Note that the integration time was adjusted to provide maximum dynamic range, furthermore the profiler was exposed to multiple pulses depending on the integration time.

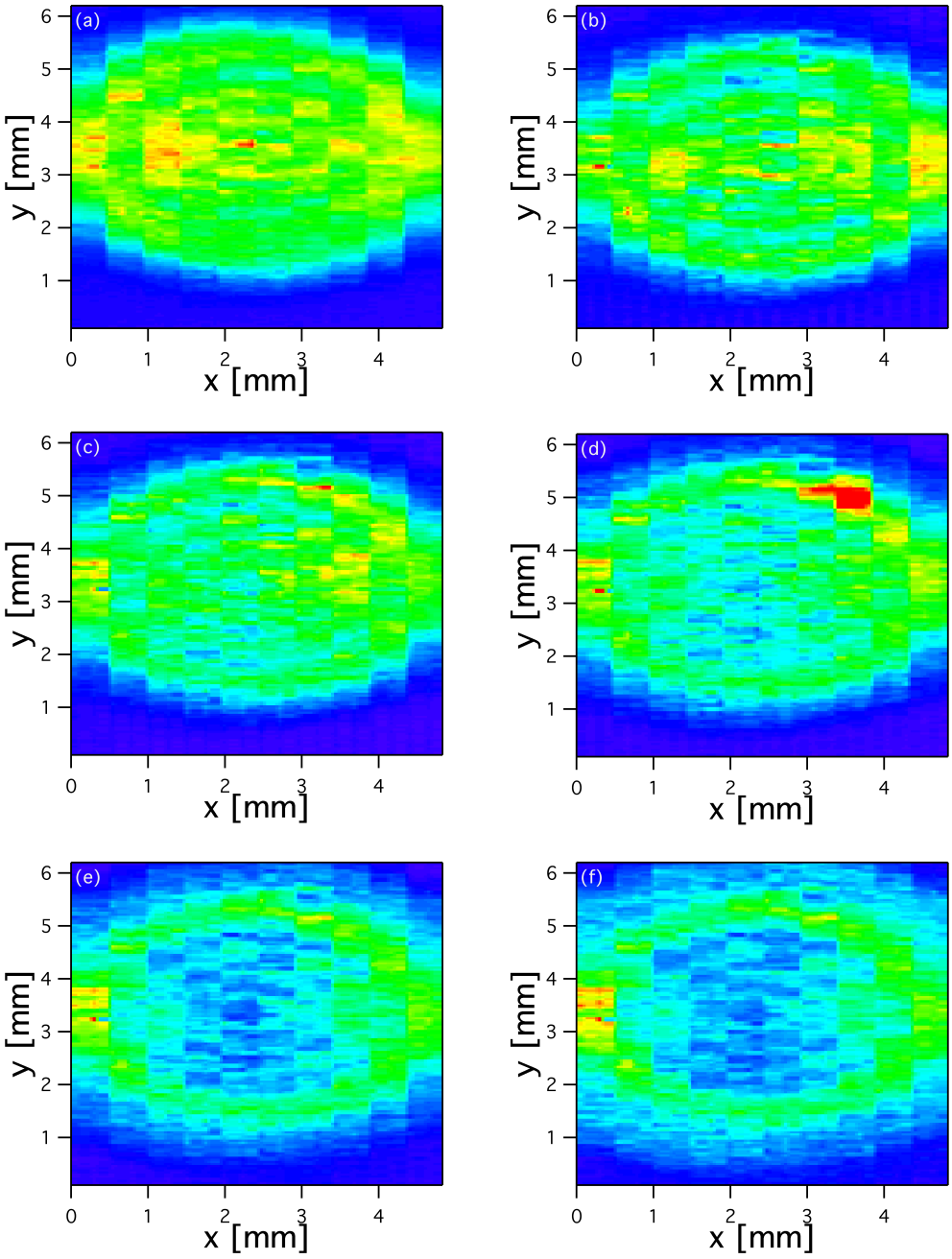

Figure 4.8: Beam profiles: (a) before the lens, (b) behind the telescope without a sample, (c) behind the telescope with a sample pulse energy 10 μJ, (d) behind the telescope with a sample pulse energy 30 μJ, (e) behind the telescope with sample pulse energy 50 μJ, (f) behind the telescope with a sample pulse energy 80 μJ. The destruction threshold of the sample was observed to be 60 μJ. The beam profiles were taken on the same day as the FROG traces in Fig. 4.1.

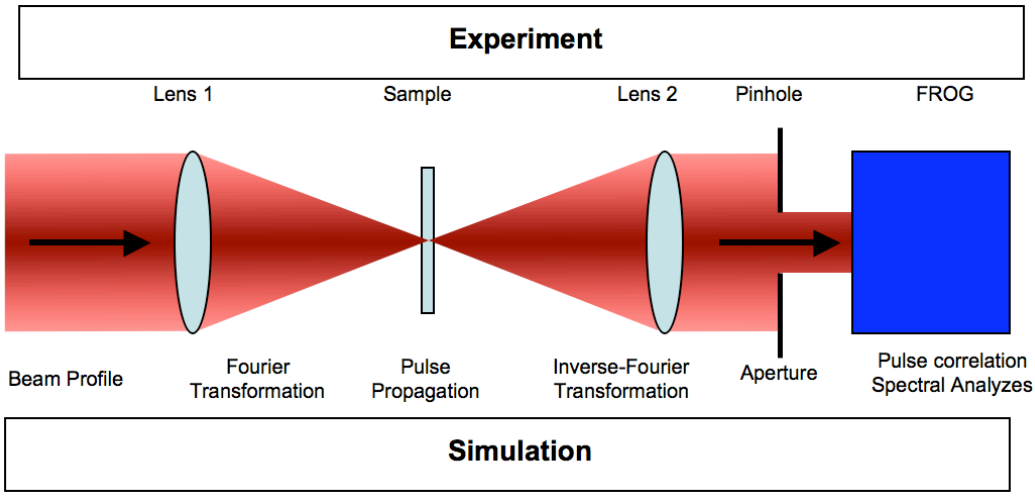

Figure 4.9: Comparison of steps in the experiment and computer simulation.

4.2 Comparison of the Experimental Results to Computer Simulations

In order to interpret the experimental results a sequence of computer simulations was used to reproduce each process in the experiment (Fig. 4.9).

Experimental measurements of the beam profile (Fig. 4.8(a)) and pulse shape (Fig. 4.2, 10 μJ) before the telescope are used as input to the computer simulation. Since the beam profile was clipped due to the finite size of the pulse profiler, it was smoothed at the edges in order to suppress high spatial frequency artifacts caused by the hard edges. The first step was to calculate the beam shape on the sample surface using as input the beam profile before the lens. Here a Fast Fourier Transfom (FFT) algorithm [153] was employed to simulate a collinear beam focused by a lens with focal length $f = 25$ cm [140; 143]. The amplitude and phase at the front face of the sample was used to construct the input field required for the pulse propagation code. Both the resolution and width of the field were reduced in order to make the pulse propagation simulation possible and consequently of this high spatial frequency components in the beam profile were filtered out (see 4.10). Simulations using

the original grid size would have exceeded available computational resources. In order to ensure that this process reproduces a realistic beam profile on the sample surface, the field was inverse-Fourier transformed to ensure that the original beam profile was reproduced. The results of this process are shown here for both a flat-top beam profile and a smoothed experimental profile (Fig. 4.10).

Fig.4.10(a) shows the flat-top beam profile which was used as an approximation of the experimental profile and as a reference. Fig.4.10(b) shows the beam profile of the Fourier and then inverse-Fourier transformed flat-top profile. 4.10(c) is a line-out at $y = 0$ from Figure (a) and (b) Fig. 4.10(b) shows the experimental smoothed measured beam profiles and Fig. 4.10(d) the output beam profiles. Here the Fourier transform and the field creation process did not introduce additional noise but acted essentially as a filter, suppressing the high frequency components in the original beam profile. This can be easily seen when comparing the intensity in both profiles at $y = 0$, shown in the lower right graph in Fig. 4.10 (f). The output beam profile is 5% wider but otherwise very similar to the original profile.

The beam waist at the sample surface is 32 μm (FWHM). The field is propagated at different pulse energies through 200 μm of fused silica using the "pulsesuite" code (see Fig. 4.9). After which the field is inverse-Fourier transformed, to model propagation to and through the recollimating lens. At this point the field is integrated over time and beam profiles are constructed; these are compared to the measured beam profiles shown in Fig. 4.8.

The "pulsesuite" code allows one to monitor the maximum plasma density inside the sample throughout the propagation process. For plasma densities higher than 1×10^{27} m^{-3} the plasma frequency is greater than the driving frequency and the plasma becomes highly absorbing and permanent damage in the sample is predicted. In practice, the simulation slows down considerably at this point and has tendency to stop. The lowest pulse energy for which the critical plasma density is reached is determined to be the damage threshold.

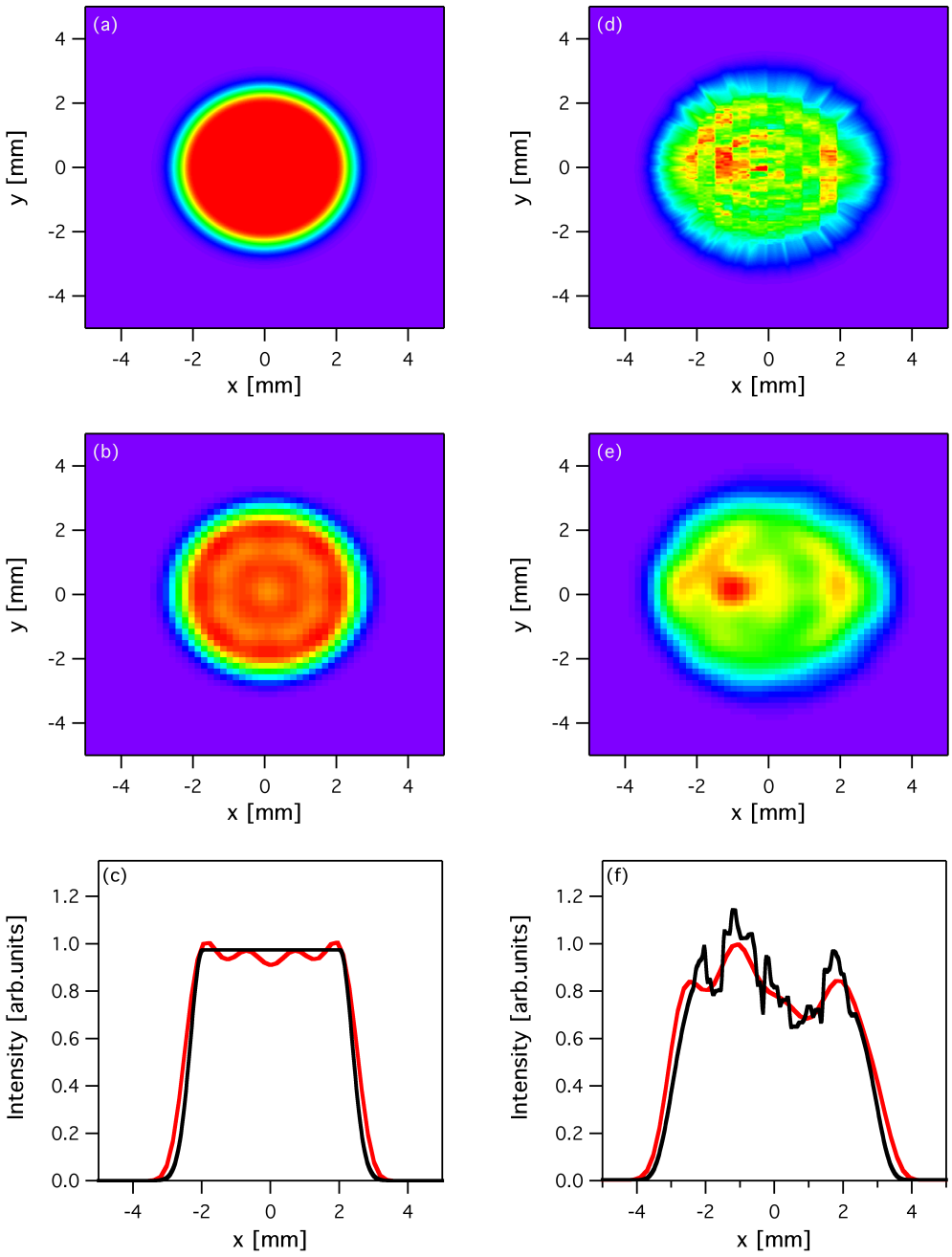

Figure 4.10: (a) shows a flat-top beam profile, (b) shows the beam profile from an integrated field constructed from (a), and (c) is the intensity line-out at $y = 0$ in (a) (black line) and (b) (red line). (d) shows the smoothed measured beam profile, (e) is the beam profile from an integrated field constructed from (d), and (f) is the intensity line-out at $y = 0$ in (d) (black line) and (e) (red line).

Since a wide variety electron collision times for fused silica have been reported in the literature, multiple computer simulations were performed using different collision times. The results presented here used a collision time of 10 fs and showed single shot destruction of the sample at an input pulse energy of between 80 μJ and 85 μJ. Sudrie *et al.* report a decrease of 10 % of the destruction threshold for multi shot damage, which would indicate a multi shot destruction threshold of $\sim$ 75 μJ. When lowering the collision time to 4 fs, the single shot destruction threshold decreases to 60 μJ, which is the experimentally found value. This study is to the author's knowledge the first successful prediction of the optical destruction threshold in fused silica using computer simulations to predict the critical plasma density.

Simulations were performed to investigate the influence of the Drude dispersion term in the NLSE (Eq. 2.31) on the pulse propagation and the damage threshold. It was found that the damage threshold was underestimated by a factor of 2 when the term was not included in the simulation. All results of computer simulations presented in this dissertation used the Drude dispersion term from reference [116] and predicted a single damage threshold that is higher by a factor of $\sim$ 1.5 greater than the observed multi-shot damage threshold. It is important to note that the results from computer simulations in the literature often underestimate the damage threshold by a factor 2 [128].

The simulated beam profiles calculated for a collision time of 10 fs are shown together with the experimentally found beam profiles in Fig. 4.11. The simulated beam profiles are shown for energies of 1 μJ, 10 μJ, 35 μJ, 50 μJ, 60 μJ and 70 μJ while the experimentally measured beam profiles are shown before the lens, and behind the telescope for pulse energies of 1 μJ, at 10 μJ, 30 μJ, 50 μJ, and 80 μJ. The simulated beam profiles show that for pulse energies lower than 50 μJ that the center region gains prominence over the features outside. The diffraction ring seen in the experimental beam profiles seems to fade in comparison with the center. For pulse energies greater than 50 μJ this tendency is somewhat reversed, as a clear ring develops while the center region fades. An interesting detail is the development of hot spots in the ring, which was seen in the experimental beam profiles for pulse energies of

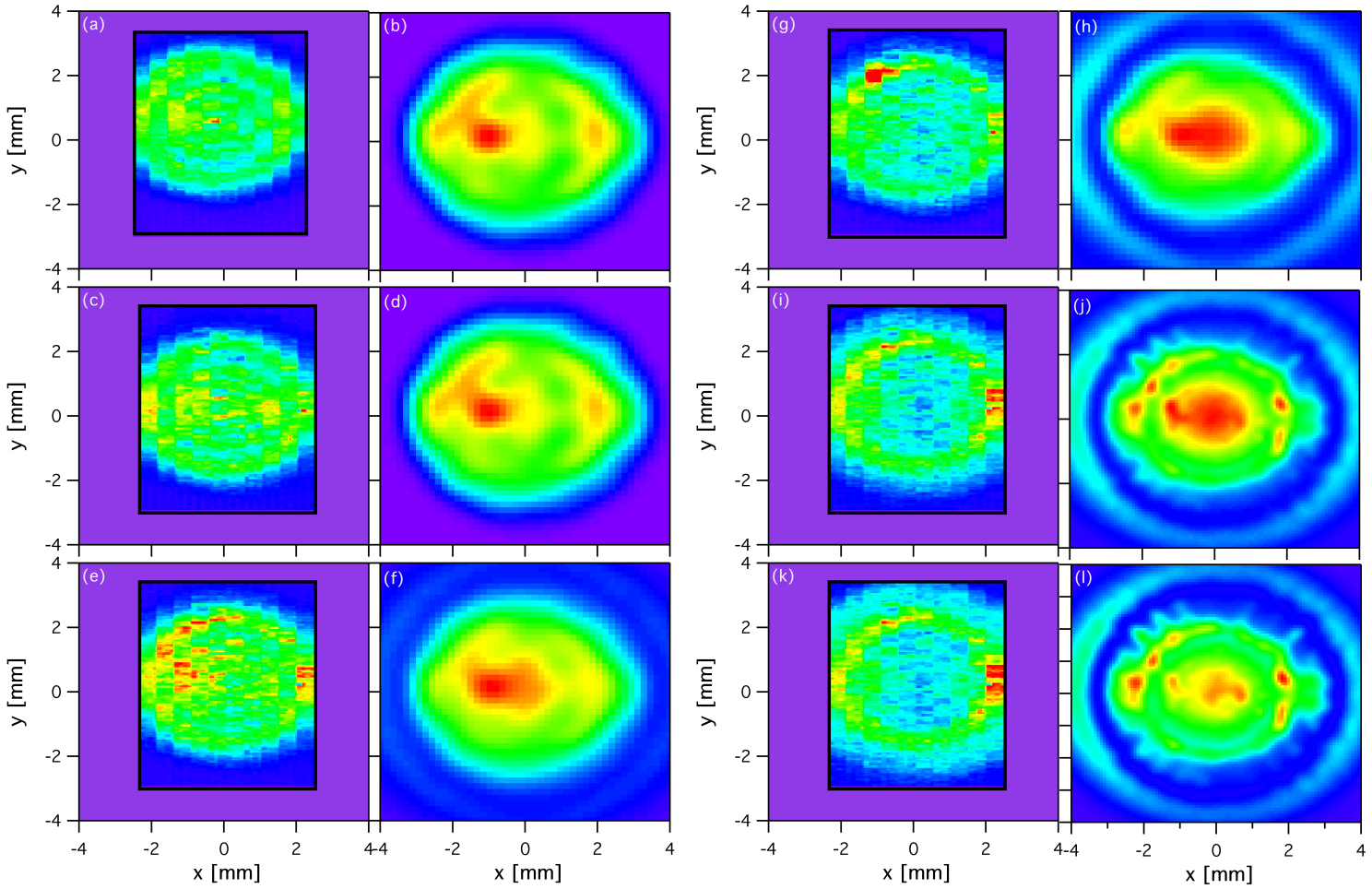

Figure 4.11: Beam profiles: (a) shows the measured beam profile before the first lens. (b) the simulated beam profile before the first lens. (c) shows the measured beam profile without sample, (d) the simulated beam profile with pulse energy of 1 μJ. Form here on out all profiles are shown behind the telescope and with sample with pulse energies: (e) the measured beam profile for 10 μJ, (f) the simulated beam profile for 10 μJ. (g) the measured beam profile for 30 μJ, (h) the simulated beam profile for 35 μJ. (i) the measured beam profile for 50 μJ, (j) the simulated beam profile for 50 μJ. (k) the measured beam profile for 80 μJ, (l) the simulated beam profile for 80 μJ.

30 μJ and higher. The similarities are nonetheless striking and the presented beam profiles are to the knowledge of the author the first computer simulations of beam profiles after an ultrashort pulse-material interaction near the damage threshold.

The amplitude and phase after the sample in the $y = 0$ plane of the pulse are shown in the first column of the Fig. 4.13 and Fig. 4.12 for different input pulse energies. With increasing input pulse energy the beam develops spatio-temporal inhomogeneities, which can be seen clearly in both amplitude and phase diagrams: The amplitude does not vary as a function of x for energies under 22 μJ, but it will be shown later that spatio-temporal dependences are often harder to identify in the amplitude than in the phase. The phase does not vary as a function of x for 1 μJ, while for higher energies a region at the center of the pulse develops in which the phase depends strongly on the position in the beam.

The amplitude and phase for the 10 μJ case show the onset of self-focusing and the development of a spatio-temporal dependence. This explains the increase of the peak amplitude in the retrieved fields from the measured FROG traces. The amplitude and phase show clear signs of filamentation at 35 μJ, and this becomes even more well defined at higher energies. Filamentation induces strong spatio-temporal dependences, which lead to a reduction of the center amplitude in the retrieved fields from the measured FROG traces.

The next step in the simulation process is to simulate the aperture shown in Fig. 4.9, by setting all values in the inverse Fourier transformed field after the sample outside of a defined radius to zero. The apertured field is then Fourier transformed again to represent the beam that is analyzed by the FROG experiment. Fig. 4.13 and Fig. 4.12 show the complex amplitude and phase respectively for different pinhole radii used. A 1" pinhole size was selected to investigate the influence of the 1" lens used in the experiment on the beam. The smaller pinholes were used to investigate the effects on the spatial temporal pulse shape of the field. The left column shows the phase and amplitude at $y = 0$ immediately after the sample.

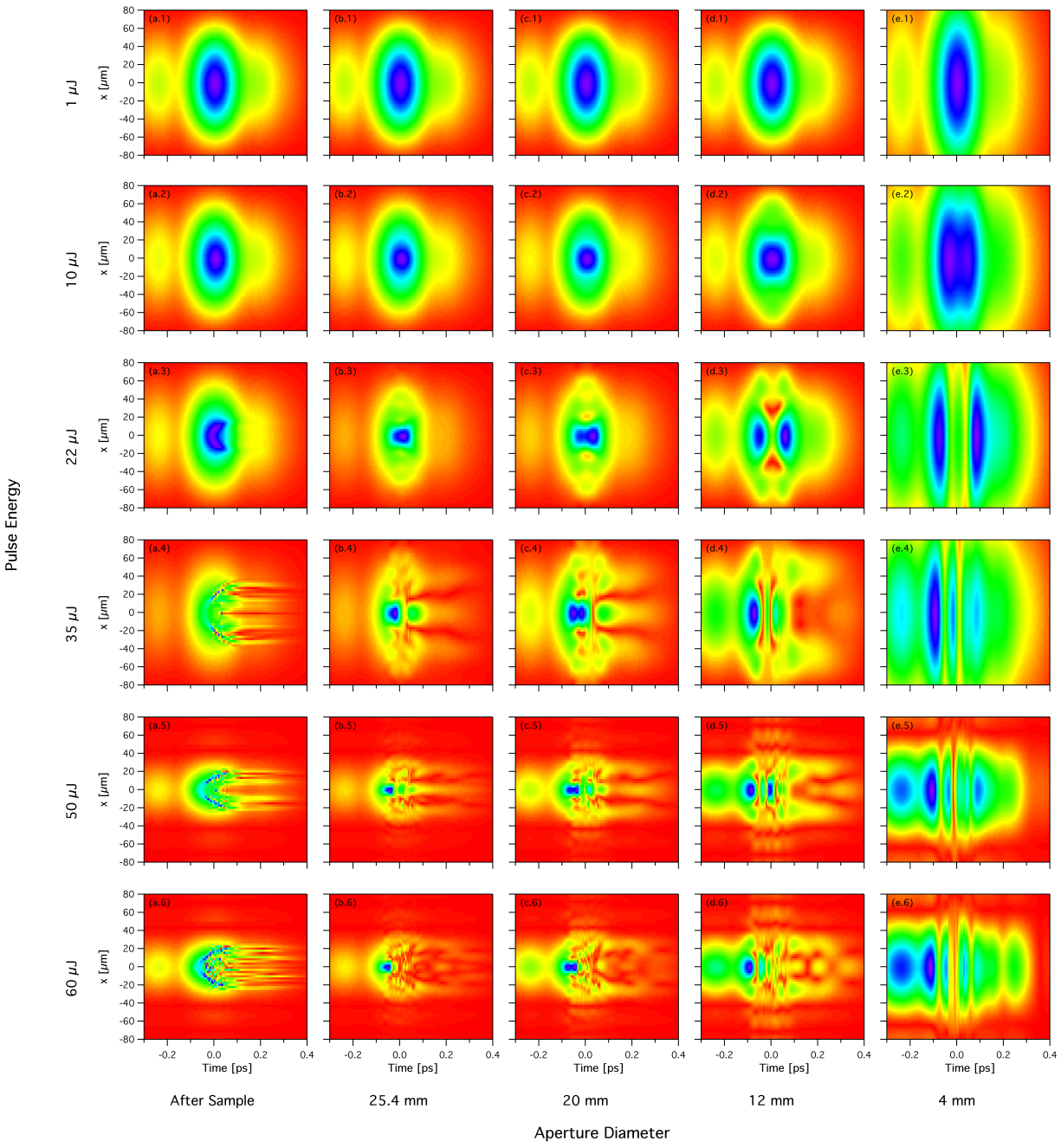

Figure 4.12: The amplitude of the complex field at $y = 0$ for different pulse energies (increasing from top to bottom), and different aperture sizes (decreasing from left to right).

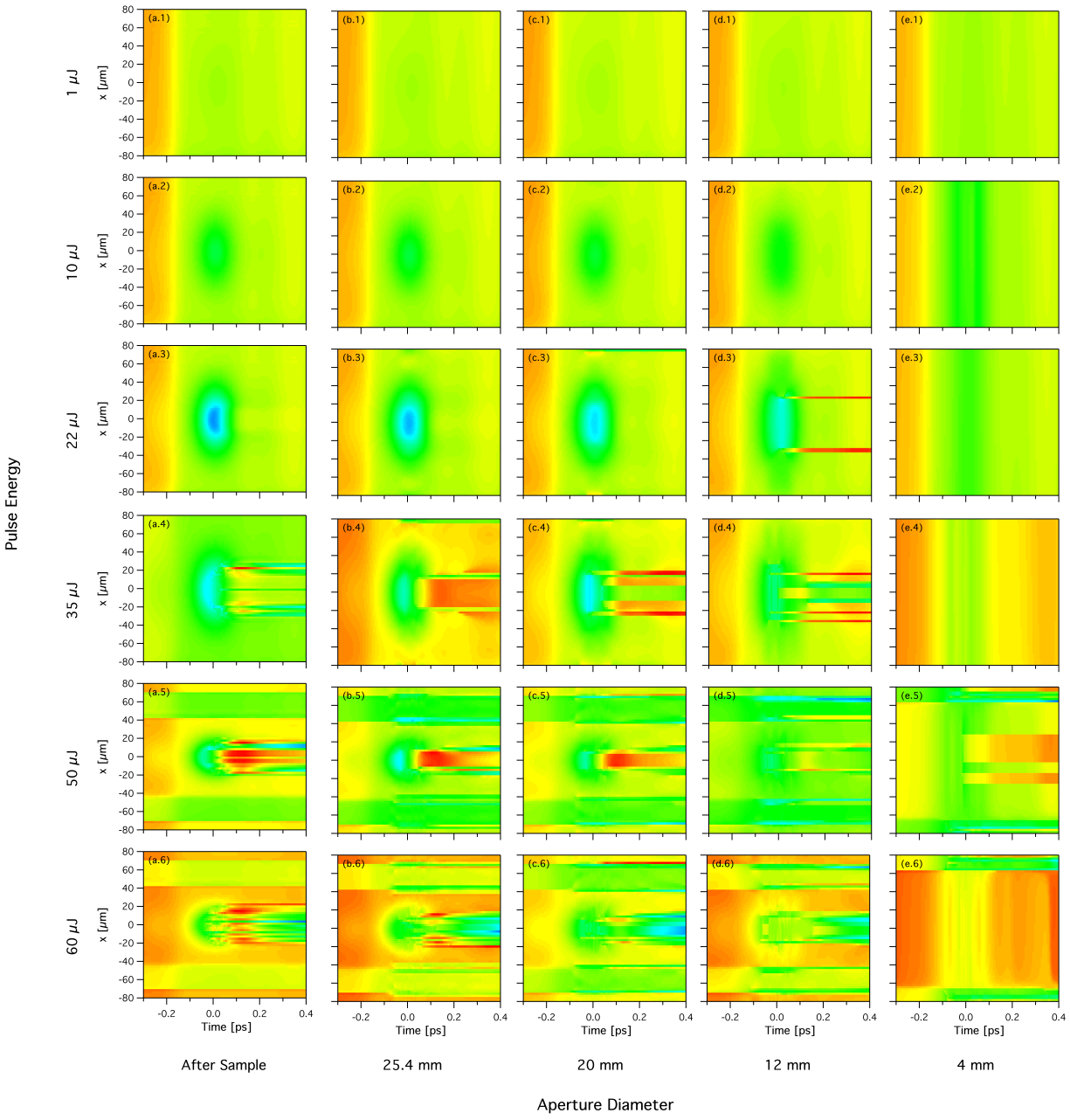

Figure 4.13: The phase of the complex field at $y = 0$ for different pulse energies (increasing from top to bottom), and different aperture sizes (decreasing from left to right).

Fig. 4.12 shows the amplitude and Fig. 4.13 the phase for the $y = 0$ plane after the field has been apertured and Fourier transformed for a range of aperture diameters. The pinhole size is reduced from left to right: The second column shows the field when apertured by a 1" optic, the third, forth, and fifth column show the results for pinholes of 2 cm, 1.2 cm and 0.4 mm diameter, respectively. It is important to notice that there is a change in pulse shape and the strong spatio-temporal dependences even for the case of the 1" optic. The pulse shape is changed dramatically and the spatio-temporal dependences prevent a retrieval of the FROG trace or even a meaningful autocorrelation measurement. Using a smaller pinhole size changes the pulse shape while reducing the spatio-temporal dependence. This can be clearly seen in the line-out at $x = 0$ shown in Fig. 4.14. Here Fig. 4.14 (a) shows the amplitude and phase for the field immediately after the sample. Fig. 4.14 (b) shows the amplitude and phase for the 1.2 cm diameter aperture and Fig. 4.14 (c) shows the amplitude and phase for 0.4 mm diameter.

The apertured amplitudes show multiple peaks, which increase in distance from each other with decreasing aperture size. The reason for this pulse splitting is the introduced strong spatio-temporal dependence at $t = 0$, at the peak of the initial pulse. When the field is Fourier transformed the beam width is increased at the point with respect to the rest of the pulse. When the pulse is now apertured the high spatial frequencies are filtered out and energy is lost. More energy has been lost at $t = 0$ than at other times in the pulse, giving the impression that the pulse splits into two pulses. The reality is that the front and the tail of the pulse stay intact, while the center of the pulse has lost most its energy, leading to a change in pulse shape. This process has been called pulse splitting in the literature [133], but must be distinguished from the pulse splitting that results from group velocity dispersion and self-focusing as observed in [87]. The pulse splitting described here is due to apertured propagation after the sample. The pulse splitting due to the group velocity dispersion and self focusing will stop when the field leaves the sample.

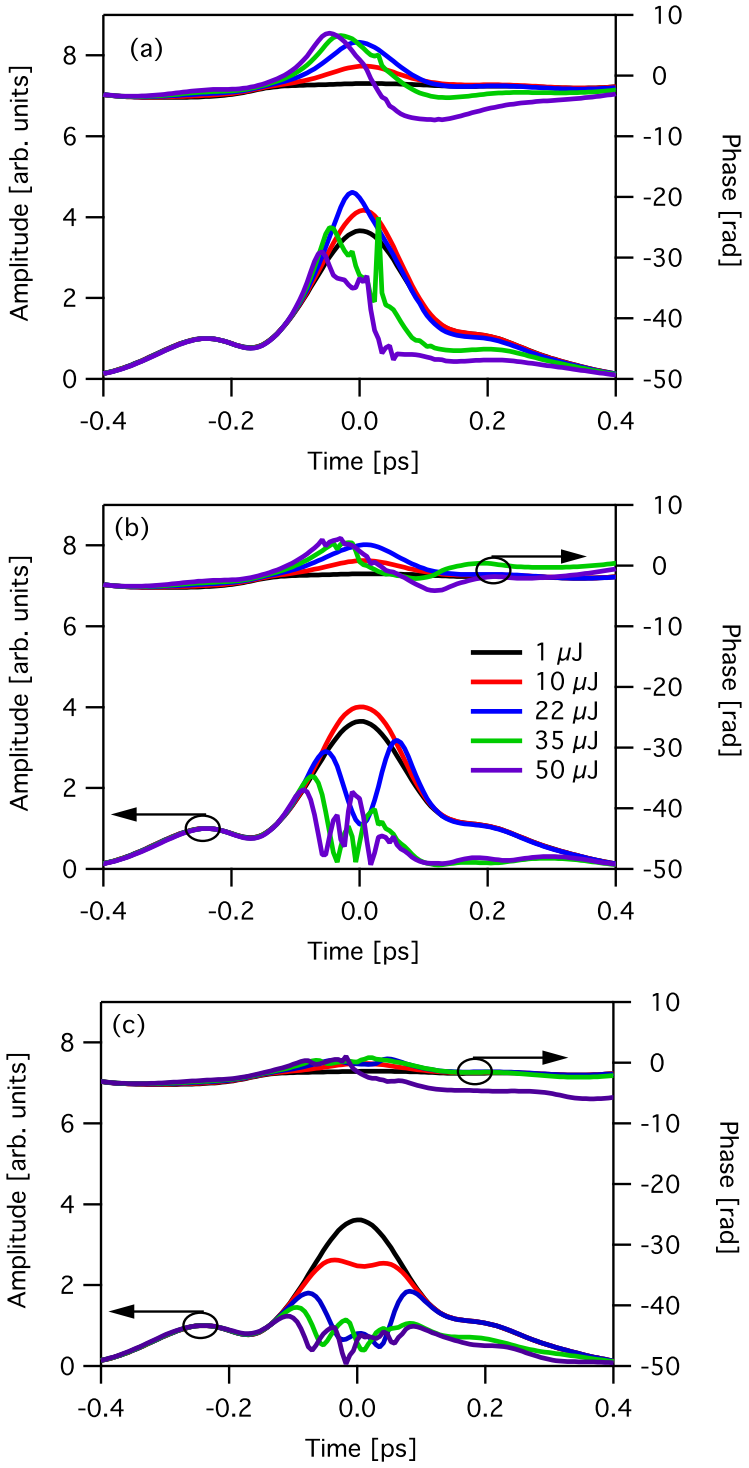

Figure 4.14: Line-outs at $x = 0$. Amplitude and phase are shown in (a) for the field immediately after the sample, in (b) with an aperture of 1.2 cm diameter, and in (c) with an aperture of 0.4 cm diameter.

It can be seen in Fig. 4.14 that the phase for the field after the sample is a strong function of time and pulse energy. For smaller aperture diameters the change is decreased until it is practically removed at an aperture size of 0.4 cm. The amplitude in 4.14.(a) shows similar behavior in amplitude than the retrieved fields from the measured FROG traces, as it increases first in peak amplitude in comparison to the pre-pulse with energy, and than decreases for energies higher than 35 μJ. However, this data also develops some sharp features in the center of the pulse which the retrieved experimental fields do not reproduce. This could be due to the lower resolution of the retrieved solution or because the field contains spatio-temporal dependences and has been apertured.

In a final step, FROG traces are constructed from the Fourier transformed apertured fields. The FROG traces constructed of the fields in Fig. 4.13 and Fig. 4.12 are shown in Fig. 4.15. Here the first row is for an unapertured field at different energies for comparison to the apertured field FROG traces. The second, third, fourth, and fifth row show the FROG traces for fields which were apertured with a 1", 1.2 cm, 4 mm and 2 mm diameter pinhole. The pulse energy increases from left to right from 1 μJ, to 10 μJ, 22 μJ, 35 μJ, 50 μJ, and 60 μJ. For energies lower than 35 μJ and a pinhole size of 1.2 cm the traces show some features seen in the unapertured experiments. The pulse maximum splits into multiple maxima and develops a long central region in delay. This similarity between the experiments with the unapertured beam and a 1.2 cm apertured beam in the computer simulation can be understood in light of the experimental setup. The mirrors are mounted in a 45° angle to the beam, reducing the beam diameter along the x axis to around 1.8 cm. The geometry of the experimental setup reduces the beam diameter by additional 25 %, to around 1.4 cm $\pm$0.2 cm. This can cause additional pulse shaping and stronger spatio-temporal dependences due to unsymmetrical clipping of the field and partially explains the discrepancy between the measured and simulated FROG traces.

An additional concern are the differences between the measured and simulated beam profiles, which indicate discrepancies between the computer simulation and the experiment.

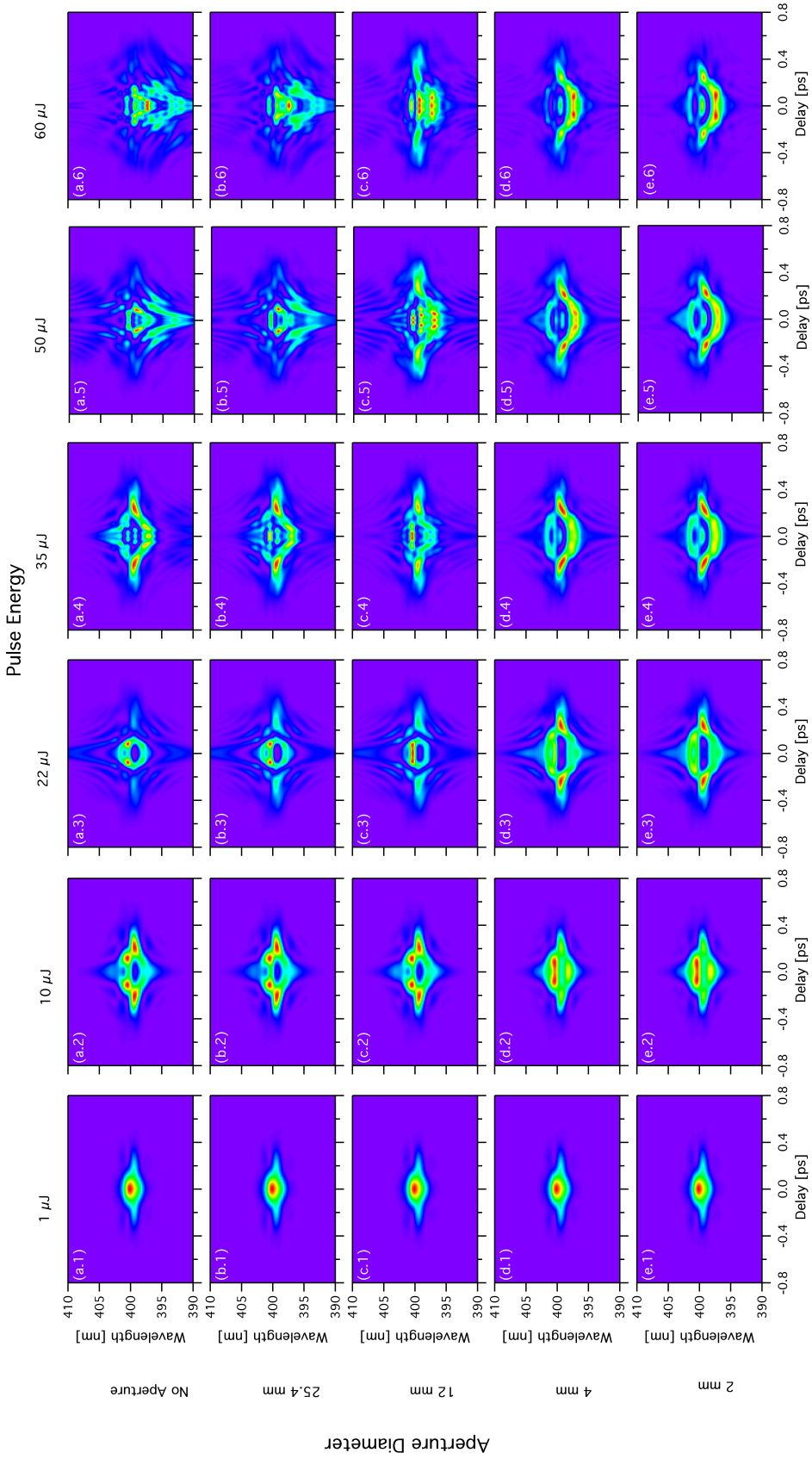

Figure 4.15: The constructed FROG traces from the simulated fields for different energies (increasing from left to right) and pinhole sizes (decreasing from top to bottom).

Small changes in the apertured region of the beam could have great impact in the FROG traces.

Other concerns might be that the simulation of the pulse propagation has a low resolution, which can lead to misrepresentation of the field after the sample. The Fourier transformations used to simulate the decollimation and the focusing have a good resolution but are limited in the dimensions of the computer grid, which is a possible but unlikely source of error, given the fact that the beam is apertured by the optics used in the experiment. As discussed in Chapter 3 the FROG generation simulation includes some approximations as well. The tilting process works with an approximation of the field at every given grid point. As well as the step size of the FROG generation had to be increased by an order of 10 in both the x and y directions, while only the center half was taken into account in order to limit the calculation time to under 5 hours per FROG trace. This process may overestimate the contribution of the center of the field compared to the outer regions of the field in cases with high spatio-temporal dependences.

For comparison with experimental data, a subset of the simulated FROG traces were analyzed using the FROG phase retrieval code. These are shown with the retrieved solutions in Fig. 4.16. The FROG traces were generated from fields with a 1.2 cm aperture, for which the amplitude and phase for different pulse energies are shown in Fig. 4.12.(d.1) - (d.6) and in Fig. 4.13.(d.1) - (d.6), respectively. The line-outs at $x = 0$, $y = 0$ for these fields are shown in 4.14.b. The retrieved fields are shown in Fig. 4.17 with the retrieval errors listed in Table 4.4. Note that the retrieved phase in Fig. 4.17 stays flat for all pulse energies which is consistent with the solutions from experimental FROG traces. When comparing the amplitude of Fig. 4.17 with the amplitude for different aperture sizes in Fig. 4.14 it becomes apparent that the retrieved solutions show more similarity with the fields in Fig. 4.14.c than with Fig. 4.14.b, which would be expected. The line-out for the 4 mm aperture field and the retrieved solutions from the 1.2 cm aperture field FROG traces both show very little variation in phase for all pulse energies. More striking is the similarity between the line-outs

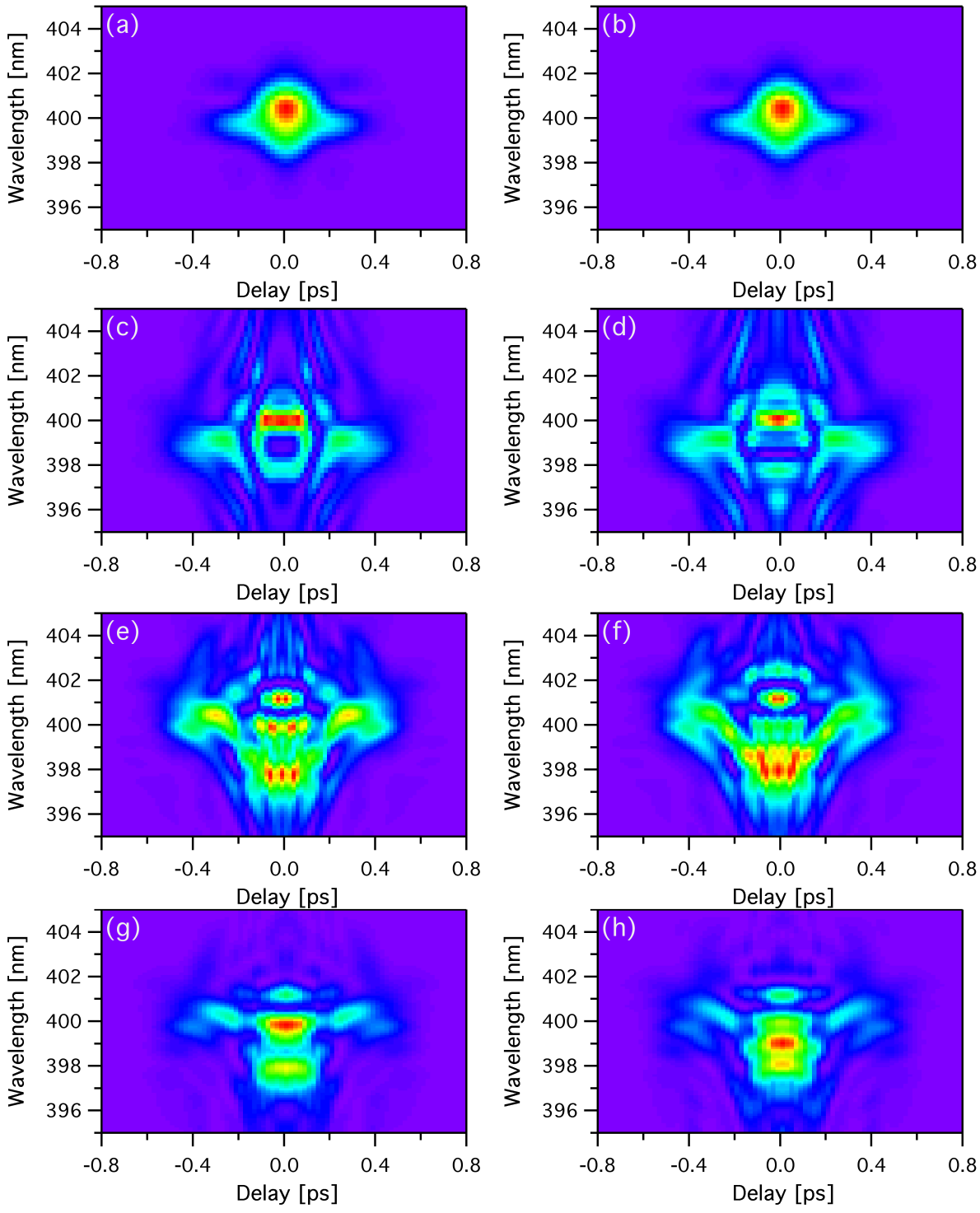

Figure 4.16: The generated FROG traces and the retrieved traces in comparison for simulated fields with an aperture of 1.2 cm diameter. (a) is the simulated FROG trace for 1 μJ with (b) the retrieved trace. (c) is the simulated FROG trace for 22 μJ with (d) the retrieved trace. (e) is the simulated FROG trace for 50 μJ with (f) the retrieved trace. (g) is the simulated FROG trace for 80 μJ with (h) the retrieved trace.

shown in Fig. 4.14.c (0.4 cm aperture) and the retrieved fields in Fig. 4.17 (1.2 cm aperture). It is interesting that the field retrieved from the FROG trace of an apertured pulse with spatio-temporal dependences is similar to the field measured through a smaller aperture. It is noteworthy that the combination of FROG with computer simulation can provide valuable insight even when spatio-temporal dependences prevents the field from being retrieved.

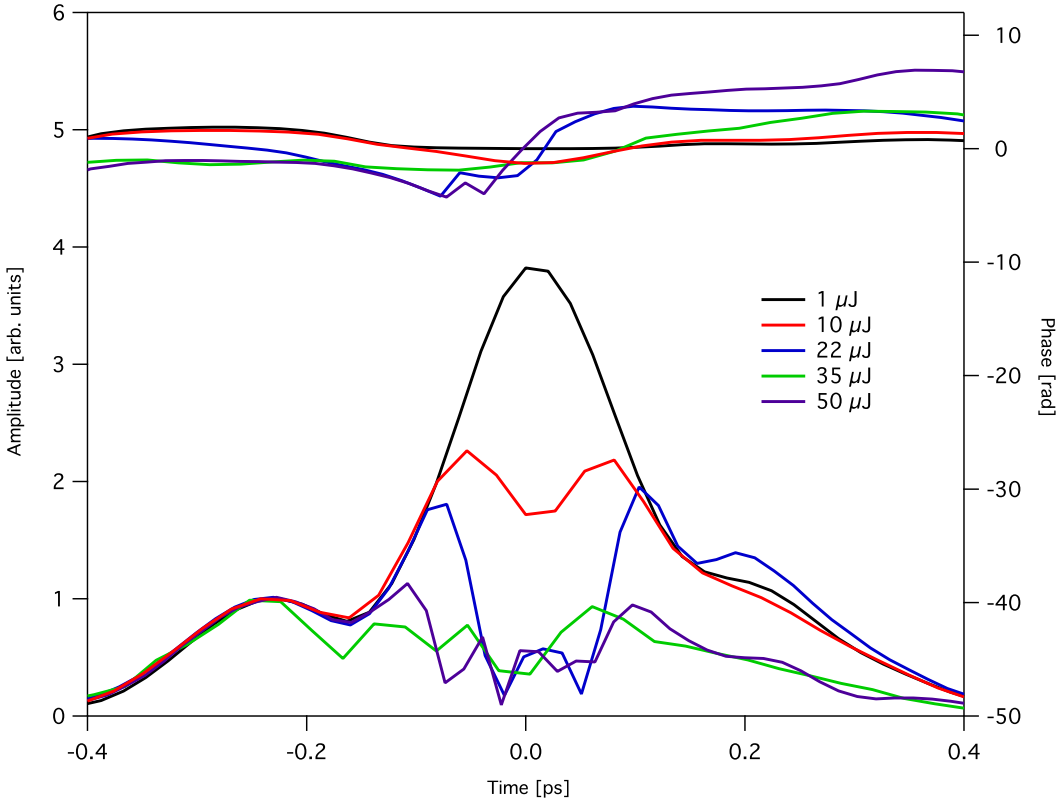

Figure 4.17: The retrieved fields in amplitude and phase as retrieved from generated FROG traces (shown in Fig. 4.16) for simulated fields with an aperture of 1.2 cm diameter.

4.3 Conclusions

Results presented in this chapter were from experiments that probe the light - matter interaction in fused silica. The first experiments use FROG to investigate the behavior of the temporal pulse shape as a function of input pulse energy. These experiments were performed using two different laser systems and explored the effect of aperturing the beam on the

Table 4.4: G_{error} and offset compensation (OC) for the retrieved complex fields in Fig. 4.17. Note that the G_{error} scales with $\sqrt{n_f n_\tau}$.

Pulse Energy	Trace Dimensions	G_{error}	OC
1 μJ	256×128	0.0062	0
10 μJ	256×128	0.0094	0
22 μJ	256×128	0.0259	0
35 μJ	256×128	0.0196	0
50 μJ	512×256	0.015	0

retrieved fields. Results were presented of an experiment that investigates the spatial profile as a function of pulse energy. In parallel, computer simulations were performed, that explain the effects of input pulse energy, aperturing and in some case electron collision time as on the temporal pulse shape and spatial beam profile. The importance of the electron dispersion for pulse lengths of 100 fs was investigated and confirmed.

Based on the detailed comparison between the experimental and the computer simulation results the following observations can be made:

1. The complex electric field in principle provides a sensitive indication of the dynamics within the material.

2. For reasonable electron collision times, the computer simulations give a reasonable prediction of the experimental damage threshold.

3. The Drude dispersion term in the NLSE is necessary even though the laser pulse width is larger than 100 fs. Computer simulations without this term significantly underestimated the damage threshold.

4. Simulated beam profiles exhibit several of the features observed in experiment: The diffraction ring stays intact for all pulse energies and shows hot spots for high pulse energies. The center region fades in comparison with the ring for high energies.

5. The discrepancy between computer simulation and experiment (in particular FROG traces) indicate that more sophisticated material models should be explored.

6. More sophisticated experiments are required, *e.g* cross-correlation FROG, aperturing in the sample plane, or single shot FROG should be performed.

7. Tight coupling between experiment and computer simulation appears to be essential if predictive models of ultrashort pulse propagation in dielectrics are to be developed.

Chapter 5

Summary, Conclusion and Future Work

A new technique has been developed to construct a high dynamic range SHG-FROG trace from FROG traces acquired with different exposure times. The resulting multi-FROG traces were analyzed using an improved retrieval code, that included threshold compensation, which retrieves the low amplitude parts of the complex field more reliably.

To investigate the light-material interaction the high dynamic range multi-FROG technique was used to analyze ultrashort high energy laser pulses that had been propagated through 200 μm thick fused silica sample. The change in the pulse shape as a function of pulse energy gives great insight into the electron generation processes. The experiments were performed with pulse energies under the destruction threshold of the sample, an important regime in which *post mortem* investigations cannot be used.

It is found that for pulse energies close to the destruction threshold the FROG traces show varying degrees of spatio-temporal dependence and are unretrievable. On the other hand, FROG traces from apertured fields are retrievable due to the reduced spatio-temporal dependence. All retrieved fields exhibited a small pre-pulse. The retrieved fields also show a strong dependence on the initial pulse energy. Furthermore the peak amplitude to pre-pulse ratio was found to vary as a function of pulse energy. It is interesting that the phase did not vary as a function of pulse energy due to the retrieval process, which is unable to resolve the phase for fields with spatio-temporal dependence. Consistent with the computer simulation, an increase of the peak-intensity with respect to the reference pre-pulse is observed for energies up to 20 μJ, due to self-focusing. The peak-power decreases with respect to the pre-pulse for higher pulse energies. This can be explained by the energy loss at the center of

the pulse due to plasma absorption inside the sample combined with the energy loss when the beam is recollimated. Since the pulse is broader in the Fourier plane at the temporal center when the spatio-temporal dependences are higher, leading to greater energy losses in the region of the pulse center.

The measured beam profiles after the sample show a clear diffraction ring for all pulse energies. Also as the pulse energy was increased, a decrease of the energy at the beam center was observed; this indicates strong diffraction due to nonlinear effects inside the sample. This is supported by the computer simulations, which predict similar beam profiles at energies close to the destruction threshold.

The computer simulations also show self-focusing and induced spatio-temporal dependences for the field inside the sample, which can explain the change in peak amplitude in the retrieved fields. While the simulated FROG traces differ from the measured ones, similar behavior is observed, indicating spatio-temporal dependences of the field at high pulse energy.

Future improvements to the computer simulation will include developing better material models, including higher order nonlinearities and a more sophisticated models for the plasma generation. Future experimental work will include improvements to the experiment, which are necessary to confirm and test the presented results. The computer simulations indicate that even a 1" optic (*e.g.* a lens or mirror) can lead to significant changes in the pulse shape. The recollimating lens behind the sample should be replaced by a lens with a larger diameter and smaller focal length. This decreases the beam diameter and lessens the effects of the spatial filtering from the optical elements. Additionally, the beam can be refocused with a long focal length lens, which will magnify the image of the beam profile at the sample. If a pinhole is placed at this point rather than in the Fourier plane, it can be used to spatially resolve the beam. An additional two lenses can then be used to image the apertured beam onto the nonlinear crystal in the FROG experiment. Preliminary calculations show that the pulse will stay intact and can be analyzed using FROG.

Using a microscope objective and a long focal length lens would allow a more direct comparison of the beam profile at the rear surface of the sample with the computer simulation. This should help determining the destruction threshold with greater precession.

It is possible to investigate the relationship between destruction threshold and beam diameter before the lens further, using the experiment in combination with the "pulsesuite" computer simulation code that is used in this work. By varying the beam diameter with a pinhole before the attenuator and investigating the destruction threshold using *post mortem* investigation techniques, the computer simulation can be used to find more precise values for the electron collision time and the electron mass.

To measure a possible change in the refractive index due to either plasma effects or damage the existing SHG-FROG should be replaced by a cross-correlation FROG (x-FROG). This would measure both a change in optical path length as well as a change in pulse shape.

Appendix A

Computing the gradient of Z with respect to E

In order to calculate the new field value $E^{(k+1)}(t)$ from $E^{(k)}(t)$ in section 3.1.4 the gradient of the error Z with respect to $E(t)$ is required. In the following the gradient $\vec{\nabla}_{\mathrm{E(t)}}$ will be derived. The starting point is the SHG FROG trace $g(t,\tau)$ in time-delay domain which is generated using:

$$g(t,\tau) = E(t)E(t-\tau), \tag{A.1}$$

where $E(t)$ is the complex field and $E(t-\tau)$ is that field delayed by τ. The Z-error is given by

$$Z = \sum_{\mathrm{i,j=1}}^{N} |g'(t_i,\tau_j) - g(t_i,\tau_j)|^2. \tag{A.2}$$

To find the direction in which E must be changed in order to minimize the Z-error, the negative of the gradient of Z with respect to E is required. In order to simplify the derivation, the calculation is performed separately for $\mathrm{Re}(E)$ and $\mathrm{Im}(E)$. By using

$$\frac{\partial E(t_i)}{\partial \mathrm{Re}(E(t_k))} = \delta(t_k - t_i) \quad \text{and} \quad \frac{\partial E(t_i)}{\partial \mathrm{Im}(E(t_k))} = i\delta(t_k - t_i)$$

it can be shown for Re(E):

$$\frac{\partial Z}{\partial \mathrm{Re}(E(t_k))} = \frac{\partial}{\partial \mathrm{Re}(E(t_k))} \sum_{\mathrm{i,j}=1}^{N} [g'(t_i,\tau_j) - g(t_i,\tau_j)][g'(t_i,\tau_j) - g(t_i,\tau_j)]^* \tag{A.3}$$

$$= \frac{\partial}{\partial \mathrm{Re}(E(t_k))} \sum_{\mathrm{i,j}=1}^{N} [g'(t_i,\tau_j) - E(t_i)E(t_i-\tau_j)][g'(t_i,\tau_j) - E(t_i)E(t_i-\tau_j)]^* \tag{A.4}$$

$$= \sum_{\mathrm{i,j}=1}^{N} -[g'(t_i,\tau_j) - E(t_i)E(t_i-\tau_j)][\delta((t_i-\tau_j)-t_k)E(t_i) + \tag{A.5}$$
$$+\delta((t_i-t_k)E(t_i-\tau_j)]^*$$
$$-[g'(t_i,\tau_j) - E(t_i)E(t_i-\tau_j)]^*[\delta((t_i-\tau_j)-t_k)E(t_i) + \tag{A.6}$$
$$+\delta((t_i-t_k)E(t_i-\tau_j)],$$
(A.7)

$$\frac{\partial Z}{\partial \mathrm{Re}(E(t_k))} = \sum_{\mathrm{j}=1}^{N} -[g'(t_k,\tau_j) - E(t_k)E(t_k-\tau_j)]^* E(t_k-\tau_j) +$$
$$-[g'(t_k+\tau_j,\tau_j) - E(t_k)E(t_k+\tau_j)]^* E(t_k+\tau_j) +$$
$$-[g'(t_k,\tau_j) - E(t_k)E(t_k-\tau_j)]E(t_k-\tau_j)^* +$$
$$-[g'(t_k+\tau_j,\tau_j) - E(t_k)E(t_k+\tau_j)]E(t_k+\tau_j)^*, \tag{A.8}$$

$$\frac{\partial Z}{\partial \mathrm{Re}(E(t_k))} = \sum_{\mathrm{j}=1}^{N} -\frac{1}{2}\mathrm{Re}\{[g'(t_k,\tau_j) - E(t_k)E(t_k-\tau_j)]E(t_k-\tau_j)^*\} +$$
$$-\frac{1}{2}\mathrm{Re}\{[g'(t_k+\tau_j,\tau_j) - E(t_k)E(t_k+\tau_j)]E(t_k+\tau_j)^*\}, \tag{A.9}$$

and similarly for $\mathrm{Im}(E)$:

$$\frac{\partial Z}{\partial \mathrm{Im}(E(t_k))} = \frac{\partial}{\partial \mathrm{Im}(E(t_k))} \sum_{\mathrm{i,j=1}}^{N} [g'(t_i,\tau_j) - g(t_i,\tau_j)][g'(t_i,\tau_j) - g(t_i,\tau_j)]^* \tag{A.10}$$

$$= \frac{\partial}{\partial \mathrm{Im}(E(t_k))} \sum_{\mathrm{i,j=1}}^{N} [g'(t_i,\tau_j) - E(t_i)E(t_i-\tau_j)][g'(t_i,\tau_j) - E(t_i)E(t_i-\tau_j)]^*, \tag{A.11}$$

$$= \sum_{\mathrm{i,j=1}}^{N} -[g'(t_i,\tau_j) - E(t_i)E(t_i-\tau_j)][i\delta((t_i-\tau_j)-t_k)E(t_i) + \tag{A.12}$$
$$+i\delta((t_i-t_k)E(t_i-\tau_j)]^*$$
$$-[g'(t_i,\tau_j) - E(t_i)E(t_i-\tau_j)]^*[i\delta((t_i-\tau_j)-t_k)E(t_i) + \tag{A.13}$$
$$+i\delta((t_i-t_k)E(t_i-\tau_j)], \tag{A.14}$$

$$\frac{\partial Z}{\partial \mathrm{Im}(E(t_k))} = \sum_{\mathrm{j=1}}^{N} -[g'(t_k,\tau_j) - E(t_k)E(t_k-\tau_j]^* iE(t_k-\tau_j) +$$
$$-[g'(t_k+\tau_j,\tau_j) - E(t_k)E(t_k+\tau_j)]^* iE(t_k+\tau_j) +$$
$$+[g'(t_k,\tau_j) - E(t_k)E(t_k-\tau_j)]iE(t_k-\tau_j)^* +$$
$$+[g'(t_k+\tau_j,\tau_j) - E(t_k)E(t_k+\tau_j)]iE(t_k+\tau_j)^*, \tag{A.15}$$

$$\frac{\partial Z}{\partial \mathrm{Im}(E(t_k))} = \sum_{\mathrm{j=1}}^{N} -\frac{1}{2}\mathrm{Im}\{[g'(t_k,\tau_j) - E(t_k)E(t_k-\tau_j)]E(t_k-\tau_j)^*\} +$$
$$-\frac{1}{2}\mathrm{Im}\{[g'(t_k+\tau_j,\tau_j) - E(t_k)E(t_k+\tau_j)]E(t_k+\tau_j)^*\}. \tag{A.16}$$

Bibliography

[1] K. M. Davis, K. Miura, N. Sugimoto, and K. Hirao, "Writing waveguides in glass with a femtosecond laser," Opt. Lett. **21**, 1729-1731 (1996).

[2] J. Kruger, and W. Kautek, "Femtosecond-pulse visible laser processing of transparent materials," Appl. Surf. Sci. **96-8**, 430-438 (1996).

[3] K. Miura, J. Qiu, H. Inouye, T. Mitsuyu, and K. Hirao, "Photowritten optical waveguides in various glasses with ultrashort pulse laser," Appl. Phys. Lett. **71**, 3329 (1997).

[4] D. Ashkenasi, H. Varel, A. Rosenfeld, S. Henz, J. Herrmann, and E. E. B. Cambell, "Application of self-focusing of picosecond laser pulses for three-dimensional microstructuring of transparent materials," Appl. Phys. Lett. **72**, 1442 (1998).

[5] M. D. Shirk, P. A. Molian, and A. P. Malshe, "Ultrashort pulsed laser ablation of diamond," J. Laser Appl. **10**, 64 (1998).

[6] E. E. B. Campbell, D. Ashkenasi, and A. Rosenfeld, "Ultra-short-pulse laser irradiation and ablation of dielectrics," Lasers in Materials Science, (1999), pp. 123-144.

[7] M. D. Perry, B. C. Stuart, P. S. Banks, M. D. Feit, V. Yanovsky, and A. M. Rubenchik, "Ultrashort-pulse laser machining of dielectric materials," J. Appl. Phys. **85**, 6803-6810 (1999).

[8] K. Minoshima, A. M. Kowalevicz, I. Hartl, E. P. Ippen, and J. G. Fujimoto, "Photonic device fabrication in glass by use of nonlinear materials processing with a femtosecond laser oscillator," Opt. Lett. **26**, 1516-1518 (2001).

[9] O. M. Efimov, L. B. Glebov, K. A. Richardson, E. Van Stryland, T. Cardinal, S. H. Park, M. Couzi, and J. L. Brunel, "Waveguide writing in chalcogenide glasses by a train of femtosecond laser pulses,"Opt. Mater. **17**, 379-386 (2001).

[10] A. Marcinkevicius, S. Juodkazis, M. Watanabe, M. Miwa, S. Matsuo, H. Misawa, and J. Nishii, "Femtosecond laser-assisted three-dimensional microfabrication in silica," Opt. Lett. **26**, 277-279 (2001).

[11] C. B. Schaffer, A. Brodeur, J. F. Garca, and E. Mazur, "Micromachining bulk glass by use of femtosecond laser pulses with nanojoule energy," Opt. Lett. **26**, 93-95 (2001).

[12] A. M. Streltsov, and N. F. Borrelli, "Fabrication and analysis of a directional coupler written in glass by nanojoule femtosecond laser pulses," Opt. Lett. **26**, 42-43 (2001).

[13] G. Cerullo, R. Osellame, S. Taccheo, M. Marangoni, D. Polli, R. Ramponi, P. Laporta, and S. De Silvestri, "Femtosecond micromachining of symmetric waveguides at 1.5 m by astigmatic beam focusing," Opt. Lett. **27**, 1938-1940 (2002).

[14] J. D. Mills, P. G. Kazansky, E. Bricchi, and J. J. Baumberg, "Embedded anisotropic microreflectors by femtosecond-laser nanomachining," Appl. Phys. Lett. **81**, 196-198 (2002).

[15] A. M. Streltsov, and N. F. Borrelli, "Study of femtosecond-laser-written waveguides in glasses," J. Opt. Soc. Am. **B 19**, 2496-2504 (2002).

[16] M. Will, S. Nolte, B. N. Chichkov, and A. T́unnermann, "Optical Properties of Waveguides Fabricated in Fused Silica by Femtosecond Laser Pulses," Appl. Opt. **41**, 4360-4364 (2002).

[17] A. P. Joglekar, H. Liu, G. J. Spooner, E. Meyhofer, G. Mourou, and A. J. Hunt, "A study of the deterministic character of optical damage by femtosecond laser pulses and applications to nanomachining," Appl. Phys. **B 77**, 25-30 (2003).

[18] R. Osellame, S. Taccheo, M. Marangoni, R. Ramponi, P. Laporta, D. Polli, S. De Silvestri, and G. Cerullo, "Femtosecond writing of active optical waveguides with astigmatically shaped beams," J. Opt. Soc. Am. **B 20**, 1559-1567 (2003).

[19] A. Saliminia, N. T. Nguyen, M. C. Nadeau, S. Petit, S. L. Chin, and R. Vallee, "Writing optical waveguides in fused silica using 1 kHz femtosecond infrared pulses," J. Appl. Phys. **93**, 3724-3728 (2003).

[20] W. Watanabe, T. Asano, K. Yamada, K. Itoh, and J. Nishii, "Wavelength division with three-dimensional couplers fabricated by filamentation of femtosecond laser pulses," Opt. Lett. **28**, 2491-2493 (2003).

[21] R. Osellame, N. Chiodo, G. Valle, S. Taccheo, R. Ramponi, G. Cerullo, A. Killi, U. Morgner, M. Lederer, and D. Kopf, "Optical waveguide writing with a diode-pumped femtosecondoscillator," Opt. Lett. **29**, 1900-1902 (2004).

[22] S. Nolte, M. Will, J. Burghoff, and A. T$'$unnermann, "Ultrafast laser processing: new options for three-dimensional photonic structures," Journal of Modern Optics **51**, 2533-2542 (2004).

[23] A. Saliminia, N. T. Nguyen, S. L. Chin, and R. Vallee, "The influence of self-focusing and filamentation on refractive index modifications in fused silica using intense femtosecond pulses," Opt. Commun. **241**, 529-538 (2004).

[24] C. Hnatovsky, R. S. Taylor, P. P. Rajeev, E. Simova, V. R. Bhardwaj, D. M. Rayner, and P. B. Corkum, "Pulse duration dependence of femtosecond-laser-fabricated nanogratings in fused silica," Appl. Phys. Lett. **87**, 014104 (2005).

[25] L. Jiang, and H. L. Tsai, "Repeatable nanostructures in dielectrics by femtosecond laser pulse trains," Appl. Phys. Lett. **87**, 151104 (2005).

[26] L. Jiang, and H. L. Tsai, "Energy transport and material removal in wide bandgap materials by a femtosecond laser pulse," Int. J. of Heat Mass Transfer **48**, 487-499 (2005).

[27] A. Vogel, J. Noack, G. Huttman, and G. Paltauf, "Mechanisms of femtosecond laser nanosurgery of cells and tissues," Appl. Phys. **B 81**, 1015-1047 (2005),

[28] L. Jiang, and H. L. Tsai, "Energy Transport and Nanostructuring of Dielectrics by Femtosecond Laser Pulse Trains," J. Heat Transfer **128**, 926 (2006).

[29] N. T. Nguyen, A. Saliminia, S. L. Chin, and R. Vallee, "Control of femtosecond laser written waveguides in silica glass," Appl. Phys. **B 85**, 145-148 (2006).

[30] T. Tamaki, W. Watanabe, H. Nagai, M. Yoshida, J. Nishii, and K. Itoh, "Structural modification in fused silica by a femtosecond fiber laser at 1558 nm," Opt. Express **14**, 6971-6980 (2006).

[31] S. K. Turitsyn, V. K. Mezentsev, M. Dubov, A. M. Rubenchik, M. P. Fedoruk, and E. V. Podivilov, "Sub-critical regime of femtosecond inscription," Opt. Express **15**, 14750-14764 (2007).

[32] L. Ehrentraut, I. Hertel, and A. Rosenfeld, "Method for finely polishing/structuring thermosensitive dielectric materials by a laser beam," (EP Patent 1,871,566, 2008).

[33] A. Mermillod-Blondin, I. M. Burakov, Y. P. Meshcheryakov, N. M. Bulgakova, E. Audouard, A. Rosenfeld, A. Husakou, I. V. Hertel, and R. Stoian, "Flipping the sign of refractive index changes in ultrafast and temporally shaped laser-irradiated borosilicate crown optical glass at high repetition rates," Phys. Rev. **B 77**, (2008)

[34] D. M. Krol, "Femtosecond laser modification of glass," Journal of Non-Crystalline Solids **354**, 416-424 (2008).

[35] H. R. Qiu, K. Miura, and K. Hirao, "Femtosecond laser-induced microfeatures in glasses and their applications," Journal of Non-Crystalline Solids **354**, 1100-1111 (2008).

[36] M. D. Shirk, P. A. Molian, and A. P. Malshe, "Ultrashort pulsed laser ablation of diamond," J. Laser Appl. **10**, 64 (1998).

[37] T. V. Kononenko, V. I. Konov, S. V. Garnov, R. Danielius, A. Piskarskas, G. Tamosauskas, and F. Dausinger, "Comparative study of the ablation of materials by femtosecond and pico-or nanosecond laser pulses," Quantum Electron. **29**, 724-728 (1999).

[38] R. R. Gattass, and E. Mazur, "Femtosecond laser micromachining in transparent materials," Nature Photonics **2**, 219 (2008).

[39] B. C. Stuart, M. D. Feit, S. Herman, A. M. Rubenchik, B. W. Shore, and M. D. Perry, "Nanosecond-to-femtosecond laser-induced breakdown in dielectrics," Phys. Rev. **B 53**, 1749-1761 (1996).

[40] A. Kaiser, "Energieeinkopplung und-relaxation in Isolatoren bei Bestrahlung mit SubpikosekundenLaserpulsen," (Diplomarbeit, TU Braunschweig, 1998).

[41] B. Rethfeld, "Unified Model for the Free-Electron Avalanche in Laser-Irradiated Dielectrics," Phys. Rev. Lett. **92**, 187401 (2004).

[42] B. Rethfeld, V. V. Temnov, K. Sokolowski-Tinten, P. Tsu, D. von der Linde, S. I. Anisimov, S. I. Ashitkov, and M. B. Agranat, "Superfast thermal melting of solids under the action of femtosecond laser pulses," J. Opt. Technol. **71**, 348-352 (2004).

[43] A. Von Hippel, "Electric Breakdown of Solid and Liquid Insulators," J. Appl. Phys. **8**, 815 (1937).

[44] H. Fröhlich, and B. V. Paranjape, "Dielectric Breakdown in Solids," Reports on Progress of Physics **6**, (1939).

[45] F. Seitz, "On the Theory of Electron Multiplication in Crystals," Phys. Rev. **76**, 1376-1393 (1949).

[46] E. Yablonovitch, "Optical Dielectric Strength of Alkali-Halide Crystals Obtained by Laser-Induced Breakdown" Appl. Phys. Lett. **19**, 495 (1971).

[47] F. W. Kaseta and H. T. Li, "Temperature Dependence of Dielectric Breakdown of Potassium Chloride Crystals under dc and Pulse Voltages" J. Appl. Phys. **37**, 2744 (1966).

[48] E. Yablonovitch, and N. Bloembergen, "Avalanche Ionization and the Limiting Diameter of Filaments Induced by Light Pulses in Transparent Media," Phys. Rev. Lett. **29**, 907-910 (1972).

[49] N. Bloembergen, "Laser-induced electric breakdown in solids," IEEE Journal of Quantum Electron., **10**, 375-386 (1974).

[50] A. S. Epifanov, "Avalanche ionization induced in solid transparent dielectrics by strong laser pulses," Soviet Physics JETP **40**, 897 (1974).

[51] J. Marburger, "Relation between optical breakdown field and stokes spectral broadening," Opt. Commun. **14**, 92-94 (1975).

[52] W. L. Smith, J. H. Bechtel, and N. Bloembergen, "Dielectric-breakdown threshold and nonlinear-refractive-index measurements with picosecond laser pulses," Phys. Rev. **B 12**, 706-714 (1975).

[53] J. P. Anthes, and M. Bass, "Direct observation of the dynamics of picosecond-pulse optical breakdown," Appl. Phys. Lett. **31**, 412 (1977).

[54] W. L. Smith, J. H. Bechtel, and N. Bloembergen, "Picosecond laser-induced breakdown at 5321 and 3547 Å: Observation of frequency-dependent behavior," Phys. Rev. **B 15**, 4039 (1977).

[55] S. Brawer, "Phenomenological theory of laser damage in insulators," Phys. Rev. **B 20**, 3422-3441 (1979).

[56] M. Sparks, D. L. Mills, R. Warren, T. Holstein, A. A. Maradudin, L. J. Sham, E. Loh Jr, and D. F. King, "Theory of electron-avalanche breakdown in solids," Phys. Rev. **B 24**, 3519-3536 (1981).

[57] D. Du, X. Liu, G. Korn, J. Squier, and G. Mourou, "Laser-induced breakdown by impact ionization in SiO2 with pulse widths frm 7 ns to 150 ns", Appl. Phys. Lett. **64**, 3071-3073 (1994).

[58] L. V. Keldysh, Sov. Phys. JETP **20**, 1307 (1965).

[59] D. Kitriotis, and L. D. Merkle, "Multiple pulse laser-induced damage phenomena in silicates," Appl. Opt. **28**, 949-958 (1989).

[60] J. Ihlemann, B. Wolff, and P. Simon, "Nanosecond and femtosecond excimer laser ablation of fused silica," Appl. Phys. **A 54**, 363-368 (1992).

[61] H. Varel, D. Ashkenasi, A. Rosenfeld, R. Herrmann, F. Noack, and E. E. B. Campbell, "Laser-induced damage in SiO2 and CaF2 with picosecond and femtosecond laser pulses," Appl. Phys. **A 62**, 293-294 (1996).

[62] D. Ashkenasi, M. Lorenz, R. Stoian, and A. Rosenfeld, "Surface damage threshold and structuring of dielectrics using femtosecond laser pulses: the role of incubation,"Appl. Surf. Sci. **150**, 101-106 (1999).

[63] A. C. Tien, S. Backus, H. Kapteyn, M. Murnane, and G. Mourou, "Short-Pulse Laser Damage in Transparent Materials as a Function of Pulse Duration," Phys. Rev. Lett. **82**, 3883-3886 (1999).

[64] M. Lenzner, J. Kröger, S. Sartania, Z. Cheng, C. Spielmann, G. Mourou, W. Kautek, and F. Krausz, "Femtosecond Optical Breakdown in Dielectrics," Phys. Rev. Lett. **80**, 4076 (1998).

[65] T. Q. Jia, R. X. Li, Z. Liu, H. Chen, and Z. Z. Xu, "Threshold of ultra-short pulse laser-induced damage in dielectric materials,"Appl. Surf. Sci. 189, 78-83 (2002).

[66] L. Sudrie, M. Franco, B. Prade, and A. Mysyrowicz, "Study of damage in fused silica induced by ultra-short IR laser pulses," Opt. Commun. **191**, 333-339 (2001).

[67] T. Gorelik, M. Will, S. Nolte, A. Tuennermann, and U. Glatzel, "Transmission electron microscopy studies of femtosecond laser induced modifications in quartz," Appl. Phys. **A 76**, 309-311 (2003).

[68] H. Kumagai, S.-H. Cho, K. Ishikawa, K. Midorikawa, M. Fujimoto, S.-i. Aoshima, and Y. Tsuchiya, "Observation of the complex propagation of a femtosecond laser pulse in a dispersive transparent bulk material," J. Opt. Soc. Am. **B 20**, 597-602 (2003).

[69] C. B. Schaffer, A. O. Jamison, and E. Mazur, "Morphology of femtosecond laser-induced structural changes in bulk transparent materials," Appl. Phys. Lett. **84**, 1441-1443 (2004).

[70] T. Q. Jia, H. X. Chen, M. Huang, F. L. Zhao, X. X. Li, S. Z. Xu, H. Y. Sun, D. H. Feng, C. B. Li, and X. F. Wang, "Ultraviolet-infrared femtosecond laser-induced damage in fused silica and CaF_2 crystals," Phys. Rev. **B 73**, 54105 (2006).

[71] T. Q. Jia, H. Y. Sun, X. X. Li, D. H. Feng, C. B. Li, S. Z. Xu, R. X. Li, Z. Z. Xu, and H. Kuroda, "The ultrafast excitation processes in femtosecond laser-induced damage in dielectric omnidirectional reflectors," J. Appl. Phys. **100**, (2006).

[72] A. Rodenas, J. A. S. Garcia, D. Jaque, G. A. Torchia, C. Mendez, I. Arias, L. Roso, and F. Agullo-Rueda, "Optical investigation of femtosecond laser induced microstress in neodymium doped lithium niobate crystals," J. Appl. Phys. **100**, 033521-033528 (2006).

[73] D. Giguére, G. Olivié, F. Vidal, S. Toetsch, G. Girard, T. Ozaki, J. C. Kieffer, O. Nada, and I. Brunette, "Laser ablation threshold dependence on pulse duration for fused silica and corneal tissues: experiments and modeling," J. Opt. Soc. Am. **A 100**24, 1562-1568 (2007).

[74] W. J. Reichman, J. W. Chan, C. W. Smelser, S. J. Mihailov, and D. M. Krol, "Spectroscopic characterization of different femtosecond laser modification regimes in fused silica," J. Opt. Soc. Am. **B 24**, 1627-1632 (2007).

[75] L. Englert, M. Wollenhaupt, L. Haag, C. Sarpe-Tudoran, B. Rethfeld, and T. Baumert, "Material processing of dielectrics with temporally asymmetric shaped femtosecond laser pulses on the nanometer scale," Appl. Phys. **A 92**, 749-753 (2008).

[76] J. B. Ashcom, R. R. Gattass, C. B. Schaffer, and E. Mazur, "Numerical aperture dependence of damage and supercontinuum generation from femtosecond laser pulses in bulk fused silica," J. Opt. Soc. Am. **B 23**, 2317-2322 (2006).

[77] F. Qur, S. Guizard, P. Martin, G. Petite, O. Gobert, P. Meynadier, and M. Perdrix, "Ultrafast carrier dynamics in laser-excited materials: subpicosecond optical studies," Appl. Phys. **B 68**, 459-463 (1999).

[78] A. Q. Wu, I. H. Chowdhury, and X. Xu, "Femtosecond laser absorption in fused silica: Numerical and experimental investigation," Phys. Rev. **B 72**, 85128 (2005).

[79] V. P. Kandidov, O. G. Kosareva, I. S. Golubtsov, W. Liu, A. Becker, N. Akozbek, C. M. Bowden, and S. L. Chin, "Self-transformation of a powerful femtosecond laser pulse into a white-light laser pulse in bulk optical media (or supercontinuum generation)," Appl. Phys. **B 77**, 149-165 (2003).

[80] N. Sanner, O. Utza, B. Bussiere, G. Coustillier, A. Leray, T. Itina, and M. Sentis, "Measurement of femtosecond laser-induced damage and ablation thresholds in dielectrics," Appl. Phys. **A 94**, 889-897 (2009).

[81] M. Li, S. Menon, J. P. Nibarger, and G. N. Gibson, "Ultrafast Electron Dynamics in Femtosecond Optical Breakdown of Dielectrics," Phys. Rev. Lett. **82**, 2394-2397 (1999).

[82] M. Henyk, D. Wolfframm, and J. Reif, "Ultra short laser pulse induced charged particle emission from wide bandgap crystals,"Appl. Surf. Sci. **168**, 263-266 (2000).

[83] C. Quoix, G. Hamoniaux, A. Antonetti, J. C. Gauthier, J. P. Geindre, and P. Audebert, "Ultrafast plasma studies by phase and amplitude measurements with femtosecond spectral interferometry," J. Quant. Spectrosc. Radiat. Transfer **65**, 455-462 (2000).

[84] R. Stoian, A. Rosenfeld, D. Ashkenasi, I. V. Hertel, N. M. Bulgakova, and E. E. B. Campbell, "Surface Charging and Impulsive Ion Ejection during Ultrashort Pulsed Laser Ablation," Phys. Rev. Lett. **88**, 97603 (2002).

[85] Y. Liu, H. Jiang, Q. Sun, Z. Wu, H. Yang, and Q. Gong, "Different tendencies of breakdown threshold on pulse duration in the subpicosecond regime in fused silica," J. Opt. **A 7**, 198-203 (2005).

[86] A. Q. Wu, I. H. Chowdhury, and X. Xu, "Plasma formation in fused silica induced by loosely focused femtosecond laser pulse," Appl. Phys. Lett. **88**, 111502 (2006).

[87] Z. Wu, H. Jiang, Q. Sun, H. Yang, and Q. Gong, "Filamentation and temporal reshaping of a femtosecond pulse in fused silica," Phys. Rev. **A 68**, 63820 (2003).

[88] S. Tzortzakis, L. Sudrie, M. Franco, B. Prade, A. Mysyrowicz, A. Couairon, and L. Berge, "Self-guided propagation of ultrashort IR laser pulses in fused silica," Phys. Rev. Lett. **8721**, (2001).

[89] L. Sudrie, A. Couairon, M. Franco, B. Lamouroux, B. Prade, S. Tzortzakis, and A. Mysyrowicz, "Femtosecond Laser-Induced Damage and Filamentary Propagation in Fused Silica," Phys. Rev. Lett. **89**, 186601 (2002).

[90] N. T. Nguyen, A. Saliminia, W. Liu, S. L. Chin, and R. Vallee, "Optical breakdown versus filamentation in fused silica by use of femtosecond infrared laser pulses," Opt. Lett. **28**, 1591-1593 (2003).

[91] A. Couairon, L. Sudrie, M. Franco, B. Prade, and A. Mysyrowicz, "Filamentation and damage in fused silica induced by tightly focused femtosecond laser pulses," Phys. Rev. **B 71**, 125435 (2005).

[92] P. Audebert, P. Daguzan, A. Dos Santos, J. C. Gauthier, J. P. Geindre, S. Guizard, G. Hamoniaux, K. Krastev, P. Martin, and G. Petite, "Space-Time Observation of an Electron Gas in SiO_2," Phys. Rev. Lett. **73**, 1990-1993 (1994).

[93] G. Petite, P. Daguzan, S. Guizard, and P. Martin, "Ultrafast processes in laser irradiated wide bandgap insulators,"Appl. Surf. Sci. **109**, 36-42 (1997).

[94] J. W. Chan, T. Huser, S. Risbud, and D. M. Krol, "Structural changes in fused silica after exposure to focused femtosecond laser pulses," Opt. Lett. **26**, 1726-1728 (2001).

[95] D. Von der Linde, and H. Schueler, "Breakdown threshold and plasma formation in femtosecond laser-solid interaction," TECHNICAL DIGEST SERIES-OSA **16**, 224-224 (1994).

[96] D. M. Simanovskii, H. A. Schwettman, H. Lee, and A. J. Welch, "Midinfrared Optical Breakdown in Transparent Dielectrics," Phys. Rev. Lett. **91**, 107601 (2003).

[97] R. Stoian, S. Winkler, M. Hildebrand, M. Boyle, A. Thoss, M. Spyridaki, E. Koudoumas, N. M. Bulgakova, A. Rosenfeld, and P. Tzanetakis, "Temporal Pulse Shaping and Optimization in Ultrafast Laser Ablation of Materials," Materials Research Society Symposium Proceedings **780**, 183-194 (2003).

[98] M. Mero, A. J. Sabbah, J. Zeller, and W. Rudolph, "Femtosecond dynamics of dielectric films in the pre-ablation regime," Appl. Phys. **A 81**, 317-324 (2005).

[99] S. S. Mao, F. Quere, S. Guizard, X. Mao, R. E. Russo, G. Petite, and P. Martin, "Dynamics of femtosecond laser interactions with dielectrics," Appl. Phys. **A 79**, 1695-1709 (2004).

[100] A. Horn, E. W. Kreutz, and R. Poprawe, "Ultrafast time-resolved photography of femtosecond laser-induced modifications in BK7 glass and fused silica," Appl. Phys. **A 79**, 923-925 (2004).

[101] Q. Sun, H. Jiang, Y. Liu, Z. Wu, H. Yang, and Q. Gong, "Measurement of the collision time of dense electronic plasma induced by a femtosecond laser in fused silica," Opt. Lett. **30**, 320-322 (2005).

[102] K. Yamada, W. Watanabe, T. Toma, K. Itoh, and J. Nishii, "*In-situ* observation of photoinduced refractive-index changes in filaments formed in glasses by femtosecond laser pulses," Opt. Lett. **26**, 19-21 (2001).

[103] A. P. Joglekar, H. Liu, G. J. Spooner, E. Meyhofer, G. Mourou, and A. J. Hunt, "A study of the deterministic character of optical damage by femtosecond laser pulses and applications to nanomachining," Appl. Phys. **B 77**, 25-30 (2003).

[104] X. Mao, S. S. Mao, and R. E. Russo, "Imaging femtosecond laser-induced electronic excitation in glass," Appl. Phys. Lett. **82**, 697 (2003).

[105] J. Siegel, D. Puerto, W. Gawelda, G. Bachelier, J. Solis, L. Ehrentraut, and J. Bonse, "Plasma formation and structural modification below the visible ablation threshold in fused silica upon femtosecond laser irradiation," Appl. Phys. Lett. **91**, (2007).

[106] S. Henz, and J. Herrmann, "Self-channeling and pulse shortening of femtosecond pulses in multiphoton-ionized dispersive dielectric solids," Phys. Rev. **A 59**, 2528-2531 (1999).

[107] T. Apostolova, and Y. Hahn, "Modeling of laser-induced breakdown in dielectrics with subpicosecond pulses," J. Appl. Phys. **88**, 1024-1034 (2000).

[108] A. Couairon, and L. Berg, "Modeling the filamentation of ultra-short pulses in ionizing media," Phys. Plasmas **7**, 193 (2000).

[109] A. L. Gaeta, "Catastrophic Collapse of Ultrashort Pulses," Phys. Rev. Lett. 84, 3582 (2000).

[110] C. H. Fan, and J. P. Longtin, "Modeling optical breakdown in dielectrics during ultrafast laser processing," Appl. Opt. **40**, 3124-3131 (2001).

[111] M. R. Junnarkar, "Short pulse propagation in tight focusing conditions," Opt. Commun. **195**, 273-292 (2001).

[112] K. Ishikawa, H. Kumagai, and K. Midorikawa, "High-power regime of femtosecond-laser pulse propagation in silica: Multiple-cone formation," Phys. Rev. **E 66**, (2002)

[113] E. Perlin, A. Ivanov, and R. Levitskii, "Prebreakdown generation of nonequilibrium electron-hole pairs: The multiphoton avalanche effect," J. Exp. Theor. Phys. **101**, 357-366 (2005).

[114] J. Liu, X. Chen, J. Liu, Y. Zhu, Y. Leng, J. Dai, R. Li, and Z. Xu, "Spectrum reshaping and pulse self-compression in normally dispersive media with negatively chirped femtosecond pulses," Opt. Express **14**, 979-987 (2006).

[115] C. L. Arnold, A. Heisterkamp, W. Ertmer, and H. Lubatschowski, "Computational model for nonlinear plasma formation in high NA micromachining of transparent materials and biological cells," Opt. Express **15**, 10303-10317 (2007).

[116] J. R. Gulley, S. W. Winkler, and W. M. Dennis, "Simulation and analysis of ultrafast laser pulse induced plasma generation in dielectric materials," Proceedings of SPIE **6572**, 65720R (2007).

[117] V. Gruzdev, T. V. Smirnova, O. M. Fedotova, O. K. Khasanov, A. P. Sukhorukov, B. Rethfeld, V. V. Temnov, K. Sokolowski-Tinten, and D. van der Linde, "Terawatt

femtosecond pulse propagation in dielectric solids," Quantum Electron. Conference, 2003. EQEC'03. European, (2003).

[118] L. Hallo, A. Bourgeade, V. T. Tikhonchuk, C. Mezel, and J. Breil, "Model and numerical simulations of the propagation and absorption of a short laser pulse in a transparent dielectric material: Blast-wave launch and cavity formation," Phys. Rev. **B 76**, (2007).

[119] V. E. Gruzdev, and J. K. Chen, "Laser-induced ionization and intrinsic breakdown of wide band-gap solids," Appl. Phys. **A 90**, 255-261 (2008)

[120] L. Jiang, and H.-L. Tsai, "A plasma model combined with an improved two-temperature equation for ultrafast laser ablation of dielectrics," J. Appl. Phys. **104**, 093101-093108 (2008).

[121] T. Otobe, M. Yamagiwa, J. I. Iwata, K. Yabana, T. Nakatsukasa, and G. F. Bertsch, "First-principles electron dynamics simulation for optical breakdown of dielectrics under an intense laser field," Phys. Rev. **B 77**, 165104-165105 (2008).

[122] K. Sala, G. Kenney-Wallace, and G. Hall, "CW autocorrelation measurements of picosecond laser pulses," IEEE Journal of Quantum Electron., **16**, 990-996 (1980).

[123] D. M. Rayner, P. A. Hackett, and C. Willis, "Ultraviolet laser, short pulse-width measurement by multi-photon ionization autocorrelation," Rev. Sci. Instrum. **53**, 537-538 (1982).

[124] O. L. Bourne, and A. J. Alcock, "Ultraviolet and visible single-shot autocorrelator based on multi-photon ionization," Rev. Sci. Instrum. **57**, 2979-2982 (1986).

[125] A. Gierulski, G. Marowsky, B. Nikolaus, and N. Vorobev, "Surface 2nd-Harmonic generation - a novel technique for picosecond-pulse duration measurements," Appl. Phys. **B 36**, 133-135 (1985).

[126] E. S. Kintzer, and C. Rempel, "Near-surface second-harmonic generation for autocorrelation measurements in the uv," Appl. Phys. **B 42**, 91-95 (1987).

[127] J. I. Dadap, G. B. Focht, D. H. Reitze, and M. C. Downer, "Two-photon absorption in diamond and its application to ultraviolet femtosecond pulse-width measurement," Opt. Lett. **16**, 499501 (1991).

[128] S. W. Winkler"Anregungskanle von Elektronen in transparenten Dielektrika durch ultrakurzes Laserlicht", Diplomarbeit Technische Universit´at Berlin, Berlin, Sep.2003.

[129] R. W. Gerchberg, and W. O. Saxton, Optik **35**, 237 (1972).

[130] R. Trebino, and D. J. Kane, "Using phase retrieval to measure the intensity and phase of ultrashort pulses: frequency-resolved optical gating," J. Opt. Soc. Am. **A 10**, 1101-1111 (1993).

[131] C. Iaconis, and I. A. Walmsley, "Spectral phase interferometry for direct electric-field reconstruction of ultrashort optical pulses," Opt. Lett. **23**, 792-794 (1998)

[132] J. K. Ranka, R. W. Schirmer, and A. L. Gaeta, "Observation of Pulse Splitting in Nonlinear Dispersive Media," Phys. Rev. Lett. **77**, 3783 (1996).

[133] A. A. Zozulya, S. A. Diddams, and T. S. Clement, "Investigations of nonlinear femtosecond pulse propagation with the inclusion of Raman, shock, and third-order phase effects," Phys. Rev. **A 58**, 3303-3310 (1998).

[134] S. A. Diddams, H. K. Eaton, A. A. Zozulya, and T. S. Clement, "Characterizing the nonlinear propagation of femtosecond pulses in bulk media," IEEE Journal of J. Sel. Top. Quantum Electron. **4**, 306-316 (1998).

[135] X. W. Chen, Y. X. Leng, J. Liu, Y. Zhu, R. X. Li, and Z. Z. Xu, "Pulse self-compression in normally dispersive bulk media," Opt. Commun. **259**, 331-335 (2006).

[136] J. Liu, X. Chen, J. Liu, Y. Zhu, Y. Leng, J. Dai, R. Li, and Z. Xu, "Spectrum reshaping and pulse self-compression in normally dispersive media with negatively chirped femtosecond pulses," Opt. Express **14**, 979-987 (2006).

[137] S. Skupin, G. Stibenz, L. Berg, F. Lederer, T. Sokollik, and M. Schnrer, "Self-compression by femtosecond pulse filamentation: Experiments versus numerical simulations," Phys. Rev. **E 74**, 056604 (2006).

[138] S. W. Winkler, I. M. Burakov, R. Stoian, N. M. Bulgakova, A. Husakou, A. Mermillod-Blondin, A. Rosenfeld, D. Ashkenasi, and I. V. Hertel, "Transient response of dielectric materials exposed to ultrafast laser radiation," Appl. Phys. **A 84**, 413-422 (2006).

[139] E. Hecht, A. Zajac, V. A. Martynov, and J. I. Selichov, Optics (Addison-Wesley Reading, Mass, 1998).

[140] M. Born, E. Wolf, and A. B. Bhatia, Principles of optics (Pergamon Press New York, 1975).

[141] R. L. Sutherland, and F. K. Hopkins, "Handbook of Nonlinear Optics," Optical Engineering **36**, 964 (1997).

[142] G. S. He, S. H. Liu, S. Mixing, T. Mixing, I. Changes, P. Effects, S. P. M. Self-Focusing, S. Self-Broadening, O. Phase-Conjugation, and O. C. T. Effects, "Physics of nonlinear optics", Opt. Photonics News **12**, (2001).

[143] L. Bergmann, and C. Schaefer, "Lehrbuch der Experimentalphysik", Walter de Gruyter, (2005).

[144] P. Drude, Ann. Phys. **306** 1, **566** and **306** 3, **369** (1900).

[145] J. D. Jackson, and R. F. Fox, "Classical Electrodynamics," Am. J. Phys. **67**, 841 (1999).

[146] Kittel, Charles, "Introduction to solid state physics.", John Wiley & Sons, Inc., (Skupin).

[147] A. Couairon, and A. Mysyrowicz, "Femtosecond filamentation in transparent media," Phys. Rep. **441**, 47-189 (2007).

[148] M. Mero, J. Liu, W. Rudolph, D. Ristau, and K. Starke, Scaling laws of femtosecond laser pulse induced breakdown in oxide lms, Phys. Rev. **B 71**(11), 115109 (2005).

[149] A. Couairon, G. Mchain, S. Tzortzakis, M. Franco, B. Lamouroux, B. Prade, and A. Mysyrowicz, "Propagation of twin laser pulses in air and concatenation of plasma strings produced by femtosecond infrared filaments," Opt. Commun. **225**, 177-192 (2003).

[150] S. Skupin, and L. Bergé, "Self-guiding of femtosecond light pulses in condensed media: Plasma generation versus chromatic dispersion," Physica **220**, 14-30 (2006).

[151] J. R. Gulley, "Simulation of Ultrashort Laser Pulse Propagation and Plasma Generation in Nonlinear Media," in Physics and Astronomy, (University of Georgia, Athens, 2009).

[152] W. H. Press, S. A. Teukolsky, W. T. Vetterling, and B. P. Flannery,"Numerical recipes in Fortran 77 and Fortran 90: Source code for recipes and example programs," (1996).

[153] M. Frigo and S. G. Johnson, "The design and implementation of FFTW3," Proceedings of the IEEE **93**(2), pp. 216231, 2005. special issue on"Program Generation, Optimization, and Platform Adaptation"

[154] K. Sokolowski-Tinten, and D. von der Linde, "Generation of dense electron-hole plasmas in silicon," Phys. Rev. **B 61**, 2643-2650 (2000).

[155] E. Mach, and E. Salcher, "Photographische Fixierung der durch Projektile in der Luft eingeleiteten Vorgaenge," Repertorium der Physik **23**, 587-600 (1887).

[156] E. Shechtman, Y. Caspi, and M. Irani, "Increasing Space-Time Resolution in Video," Lecture notes in computer science, 753-768 (2002).

[157] G. J. J. Dixon, "Advanced techniques measure ultrashort pulses," Laser focus world **33**, 99-105 (1997).

[158] R. W. Gerchberg, "Holography without fringes in the electron microscope," Nature **240**, 404-406 (1972).

[159] J. R. Fienup, "Phase retrieval algorithms: a comparison," Appl. Opt. **21**, 2758-2769 (1982).

[160] T. J. Pearson, and A. C. S. Readhead, "Image Formation by Self-Calibration in Radio Astronomy," Annu. Rev. Astron. Astrophys. **22**, 97-130 (1984).

[161] A. Levi, and H. Stark, "Image restoration by the method of generalized projections with application to restoration from magnitude," J. Opt. Soc. Am. **A 1**, 932-943 (1984).

[162] F. Wyrowski, and O. Bryngdahl, "Iterative Fourier-transform algorithm applied to computer holography," J. Opt. Soc. Am. **A 5**, 1058-1065 (1988).

[163] F. Wyrowski, "Diffractive optical elements: iterative calculation of quantized, blazed phase structures," J. Opt. Soc. Am. **A 7**, 961-969 (1990).

[164] R. P. Millane, "Phase retrieval in crystallography and optics," J. Opt. Soc. Am. **A 7**, 394-411 (1990).

[165] F. Wyrowski, and O. Bryngdahl, "Digital holography as part of diffractive optics," Rep. Prog. Phys. **54**, 1481-1571 (1991).

[166] J. Miao, D. Sayre, and H. N. Chapman, "Phase retrieval from the magnitude of the Fourier transforms of nonperiodic objects," J. Opt. Soc. Am. **A 15**, 1662-1669 (1998).

[167] D. Sayre, "X-Ray Crystallography: The Past and Present of the Phase Problem," Struct. Chem. **V 13**, 81-96 (2002).

[168] S. Marchesini, H. He, H. N. Chapman, S. P. Hau-Riege, A. Noy, M. R. Howells, U. Weierstall, and J. C. H. Spence, "X-ray image reconstruction from a diffraction pattern alone," Phys. Rev. **B 68**, 140101 (2003).

[169] F. Pfeiffer, T. Weitkamp, O. Bunk, and C. David, "Phase retrieval and differential phase-contrast imaging with low-brilliance X-ray sources," Nature Physics, **2**, 258-261 (2006).

[170] Rick Trebino, Frequency-Resolved Optical Gating: "The Measurement of Ultrashort Lasser Pulses," Kluwer Academic Publisher, New York, (2002).

[171] C. Billet, J. Dudley, N. Joly, and J. Knight, "Intermediate asymptotic evolution and photonic bandgap fiber compression of optical similaritons around 1550 nm," Opt. Expr. **13**, 3236-3241 (2005).

[172] J. M. Dudley, C. Finot, D. J. Richardson, and G. Millot, "Self-similarity in ultrafast nonlinear optics," Nature Physics **3**, 597-603 (2007).

[173] K. W. DeLong, D. N. Fittinghoff, R. Trebino, B. Kohler, and K. Wilson, "Pulse retrieval in frequency-resolved optical gating based on the method of generalized projections," Opt. Lett. **19**, 2152-2152 (1994).

[174] C. Liebig, Privat Communication (2008).

[175] H. Wang, S. Backus, Z. Chang, R. Wagner, K. Kim, X. Wang, D. Umstadter, T. Lei, M. Murnane, H. Kapteyn, J. Opt. Soc. Am. **B**, **16**, (10), 1790-1794.(Skupin).

[176] S. Mann, R. W. Picard, IS & T's 48th annual conference, 422-428 (1995).

[177] M. D. Grossberg, S. K. Nayar, Lecture Notes in Computer Science, Proc. ECCV, **2353**, 189-205,(2002).

[178] M. D. Grossberg, S. K. Nayar, Proc. ICCV Workshop on Color and Photometric Methods in Computer Vision (CPMCV) (2003).